NATIONAL CENTRE FOR NUCLEAR RESEARCH

DOCTORAL THESIS

Modelling and Uncertainty Quantification of Nuclear Fuel Performance in HTGR

NAIRI BAGHDASARYAN

A thesis submitted in fulfilment of the requirements
for the degree of Doctor of Physical Sciences
in the National Centre for Nuclear Research

Supervisor:

Prof. Tomasz Kozłowski

Auxiliary supervisor:

Dr. Agnieszka Boettcher

Acknowledgments

I would like to express my deepest gratitude to my supervisor, Prof. Tomasz Kozlowski, for his invaluable guidance and support throughout my doctoral research. His patience, expertise, and encouragement have been instrumental in helping me navigate the challenges of academic research, and I am truly grateful for his mentorship.

I am also indebted to the members of my thesis committee for their insightful comments, constructive criticism, and unwavering support. Their expertise and feedback have been instrumental in shaping my research and helping me to improve my writing and analysis.

I would like to thank the staff of the UZ3 department at NCBJ and my auxiliary supervisor Agnieszka Boettcher for their support and encouragement, as well as my fellow graduate students, who always helped me when any needed any support.

My research would not have been possible without the generous funding and support of PhD4Gen project members (especially Prof. M. Dąbrowski and Dr. K. Kowal), and I am deeply grateful for the provided support.

Finally, I want to express my heartfelt appreciation to my family and friends, who have supported me in countless ways throughout this journey. Their love, encouragement, and understanding have been the bedrock of my success, and I am grateful for their unwavering support.

Thank you all for your contributions to my research and my personal and professional growth.

Contents

List of Figures

List of Tables

Nomenclature

Abbreviations

BAF – Bacon Anisotropy Factor

BISO – Bi-structural ISOtropic

FGR – Fission Gas Release

FP – Fission Products

GT-MTR – Gas Turbine Materials Testing Reactor

HTGR – High Temperature Gas Cooled Reactor

HTTR – High-Temperature Test Reactor

HTR – High Temperature Reactor

IPyC – Inner Pyrolytic Carbon

JAERI – Japan Atomic Energy Research Institute

NGNP – Next Generation Nuclear Plant

OpF – Free Oxygen per Fission

OPyC – Outer Pyrolytic Carbon

PyC – Pyrolytic Carbon

PCRV – Pre-Stressed Concrete Reactor Vessel

RPV – Reactor Pressure Vessel

SiC – Silicon Carbide

TRISO – TRi-structural ISOtropic

THTR – Thorium High Temperature Reactor

Greek symbols and letters

CO – Carbon monoxide

CO_2 – Carbon dioxide

E_f – Energy released per fission

FR – Failure fraction of SiC layer

K – Temperature in Kelvin

N_{tr} – Total number of TRISO particles inside fuel block

L – Operational time (in seconds)

M_{co} – Molar mass of CO

Na – Avogadro constant,

P – Pressure

P_{fb} – Power of fuel block

R – Gas constant

t – Time

T – Temperature

UO_2 – Uranium dioxide

UCO – Uranium oxycarbide

V_m – Molar volume

σ_t – Maximum tensile stress

σ_u – Mean fracture strength

m – Weibull modulus

Abstract

The primary objectives of fourth-generation nuclear reactor concepts revolve around achieving significant fuel burnup, elevated coolant temperatures, and enhanced safety levels, particularly through the utilization of passive safety systems. Among the design concepts that meet these requirements is the high-temperature gas-cooled reactor (HTGR), which incorporates tristructural isotropic (TRISO) fuel particles for power generation.

While the development and qualification programs for TRISO fuel have yielded promising outcomes regarding its potential usage, there is still a need for research and optimization regarding the modelling of fuel performance. The most significant limitations of the current modelling are (1) incomplete representative coating property data as a function of irradiation conditions, (2) insufficient understanding of the interactions between occurring phenomena as irradiation proceeds, (3) uncertainty quantification of different models/methods used in TRISO fuel performance analysis.

In this thesis, a comprehensive literature review is performed regarding the fuel performance limitations and challenges. Then a detailed comparison of different methods used in fuel performance tools is performed both for UCO and UO_2 type fuel kernels and the limitations and advantages of each model is presented. For the first time, the impact of low concentration fission gases on fuel performance analysis is estimated both for UCO and UO_2 type fuel kernels (for operational and extended burnup values). Finally, uncertainty quantification of geometrical and material data property is conducted using new approach, and the optimization potential of TRISO fuel particles is presented from the mechanical integrity perspectives. In the scope of current thesis, the Serpent and BISON fuel performance codes were used.

Streszczenie

Główne cele reaktorów jądrowych czwartej generacji skoncentrowane są na osiągnięciu znacznego wypalenia paliwa, podwyższonych temperatur chłodziwa i zwiększonych poziomów bezpieczeństwa, w szczególności poprzez wykorzystanie pasywnych systemów bezpieczeństwa. Wśród koncepcji projektowych spełniających te wymagania znajduje się wysokotemperaturowy reaktor chłodzony gazem (HTGR), który wykorzystuje trójstrukturalne izotropowe cząstki paliwa (TRISO).

Podczas, gdy programy rozwoju i kwalifikacji paliwa TRISO przyniosły obiecujące wyniki w zakresie jego potencjalnego wykorzystania, nadal istnieje potrzeba badań i optymalizacji w zakresie modelowania wydajności paliwa. Najważniejszymi ograniczeniami obecnego modelowania są: (1) niekompletne dane dotyczące właściwości powłoki w funkcji warunków napromieniowania, (2) niewystarczające zrozumienie interakcji między zachodzącymi zjawiskami w miarę postępu napromieniowania, (3) kwantyfikacja niepewności różnych modeli/metod stosowanych w analizie wydajności paliwa TRISO.

W niniejszej pracy dokonano kompleksowego przeglądu literatury dotyczącej ograniczeń i wyzwań związanych z wydajnością paliwową. Następnie dokonano szczegółowego porównania różnych metod stosowanych w narzędziach do pomiaru parametrów paliwowych zarówno dla rdzeni paliwowych typu UCO, jak i UO_2 oraz przedstawiono ograniczenia i zalety każdego z modeli. Po raz pierwszy oszacowano wpływ gazów rozszczepienia o niskim stężeniu na analizę wydajności paliw zarówno dla rdzeni paliwowych typu UCO, jak i UO_2 (dla wartości eksploatacyjnych i wydłużonego wypalenia). Na koniec, przy użyciu nowego podejścia, przeprowadzono ocenę niepewności właściwości danych geometrycznych i materiałowych, a także przedstawiono potencjał optymalizacyjny cząstek paliwa TRISO z perspektywy integralności mechanicznej. W ramach niniejszej pracy wykorzystano kody Serpent i BISON.

1. Introduction

1.1 Motivation

The development of high-temperature reactors, particularly those that use TRISO fuel, is a significant area of research in the nuclear energy field. TRISO fuel has several advantages over traditional nuclear fuels, including enhanced reactor safety and the ability to achieve high coolant outlet temperatures. However, the performance of TRISO fuel is highly dependent on the properties of the surrounding layers of the coated particles.

Given the importance of TRISO fuel technology in high-temperature gas cooled reactors, there is a need for further research to understand the properties and behaviour of these coated particles. This research can help to improve the safety and efficiency of high-temperature reactors, which are expected to be among the most likely types of 4^{th} generation reactors to be constructed in the near future.

Moreover, while the manufacturing process for TRISO fuel has been developed over the past several decades, there is still room for improvement and optimization. Through research on TRISO fuel, we can identify opportunities to improve the manufacturing process and reduce costs, making high-temperature reactors more economically viable.

Therefore, this research aims to contribute to the understanding of TRISO fuel technology and its performance, with the goal of improving the safety and efficiency of high-temperature reactors.

1.2 Objective of the thesis

The goal of this thesis is to provide insights that can help optimize the manufacturing process for TRISO fuel particles and enhance the safety and efficiency of high-temperature gas-cooled reactors. By quantifying uncertainties in the TRISO fuel performance analysis and evaluating the effects on maximum tensile stress for the SiC layer of the TRISO particles, the study can contribute to the development of more accurate performance models and improved understanding of the mechanical integrity of TRISO particles.

The thesis focuses on TRISO fuel particles with UCO and UO_2 type kernels, and examines different models used in fuel performance analysis. The assessment of the concentrations of fission gases and helium inside the fuel kernel is also performed. The study also evaluates the

free oxygen released in the system and calculates the maximal tensile stress for the SiC layer of the TRISO particle.

The thesis also seeks to quantify the differences between different methods which are currently used in fuel performance tools and evaluates the impact on the mechanical integrity of the SiC layer of the TRISO particle.

Finally, the findings of this thesis may have practical applications for the development of novel HTGR designs that incorporate TRISO fuel particles as a source of nuclear fuel.

1.3 Outline of the thesis

The dissertation consists of five Chapters, with a detailed scope of work as follows:

Chapter 1: Introduces the thesis, objectives, and the overall scope of the dissertation.

Chapter 2: Provides a comprehensive literature review of the experimental, prototype, and commercial HTGR as well as represents a basic understanding of important phenomena in TRISO fuel performance analysis, reviews modelling capabilities over the past years and points out open questions in TRISO fuel performance analysis for future studies.

Chapter 3: Focuses on analysing pressure buildup within TRISO fuel particles with UCO and UO_2 type kernels at different burnup levels. The concentrations of fission gases and helium inside the fuel kernel is quantified by using different methods and the comparison and the impact on SiC failure rate is provided.

Chapter 4: Discusses and quantifies the uncertainties and variations in geometrical configurations and material properties of TRISO fuel particles and emphasizes the importance of quantifying uncertainties in TRISO fuel particles and evaluating the optimization potential of TRISO particles.

Chapter 5: In the last Chapter, a comprehensive overview of the thesis is provided, which involves a thorough examination and analysis of the findings and outcomes presented in the previous sections.

2. Literature Review

This Chapter presents an extensive review of the literature on experimental, prototype, and commercial HTGR, and provides an overview of significant phenomena relevant to TRISO fuel performance analysis. The Chapter also discusses the advancements in modelling capabilities over the years and identifies areas that require further investigation in the analysis of TRISO fuel performance.

2.1 Brief description of HTGR Experimental Reactors, Prototype Plants and Commercial Concepts

2.1.1. Experimental HTGRs

2.1.1.1 Dragon Reactor Description (UK)

Dragon reactor [1-6] was the first HTGR built in the United Kingdom, mainly for the purpose of testing nuclear fuel and materials. The reactor was not planned for electricity production, and the heat was rejected to the environment by air-cooled heat exchangers. The fuel was a mixture of thorium and uranium carbides cladded by graphite. The core consists of 37 hexagonal fuel moderator assemblies. The control system consisted of 24 control rods made of concentric tubes of stainless steel with rings of boron carbide. The primary helium was circulated through six loops, which contained a heat exchanger and a blower. The loops were used for the decay heat removal. The containment was a double-walled system because in the beginning of the project it was thought that the primary circuit would contain large contamination.

Dragon's original fuel load was a highly enriched uranium/thorium fuel, but due to questions about long-term availability of highly enriched uranium in the United Kingdom, this was replaced by low-enriched (3.5%) uranium fuel [7].

The operation of the DRAGON reactor allowed a good availability of the entire system, the components showed a very good reliability and especially the contribution to the development and the knowledge of the behaviour of coated particle fuel was especially important for the development of HTR technology. Many experiments have been conducted, which have demonstrated the excellent safety features of HTR: for example, the measurements of strong negative temperature coefficients, the demonstration of the capability of the core to store heat in transients, and principally the concept of self-acting decay heat removal. Here are the key specifications of the Dragon reactor [7]:

- Thermal Power: 21.5 MW,
- Power Density: 14 MW/M^3,
- Secondary Coolant: Steam (low quality steam and hot water),
- Primary System Pressure: 2 MPa,
- Primary Inlet Temperature: 350C,
- Primary Outlet Temperature: 750C,
- Vessel Material: Carbon Steel,
- Core Type: Prismatic Blocks,
- Years of Operation: 1964-1975.

2.1.1.2 Peach Bottom Plant Description (USA)

Peach Bottom (PB) Unit 1 was the first HTGR to operate in the United States (located in Delta, Pennsylvania), and it was the first HTGR to produce electrical power [8-11]. It operated successfully for 8 years as a prototype reactor, demonstrating high thermal efficiency power generation and the highly enriched uranium/thorium converter fuel cycle [8]. The fuel element consisted of graphite tubes, which contain the fuel compacts. These fuel compacts consisted of U-235 and Th-232 carbide which was dispersed in a graphite matrix. Fuel and fertile material were mixed intimately.

Because PB featured up-flow of helium coolant through the core; decay heat could be removed by natural circulation using the service steam generators. The plant did not have a dedicated decay heat removal system; instead, the main circulator was run using a pony motor. The plant had a steel containment, which was inserted during operation. Reactivity control was by solid absorber rods.

One operational problem documented at PB was fission product release from the earliest loads of fuel. These were made with a simple fuel particle: the uranium or thorium kernel was coated with a single layer of pyrolytic carbon (PyC). This led to replacement fuel being made with a bi-structural isotropic (BISO) fuel particle with an inner buffer layer to accommodate fission product recoil and an outer layer to retain noble gas fission products [10].

Another operational issue was oil ingress from the oil-lubricated bearings of the helium compressors. Investigation revealed that the demister/filter on the outlet of the compressor had become saturated with oil and that approximately 100 kg of oil entered the reactor.

The steam generators in PB were the first nuclear steam generators to use Alloy-800; no leaks or failures of the steam generators were experienced during seven years of plant operation [8]. PB was the first HTGR constructed with a cross-vessel connecting the reactor vessel to a steam generator [11].

PB had completed its demonstration mission by the end of October 1974. In totally, the Peach Bottom reactor formed the basis for the development of the HTR in the USA. Experiences on coated particle fuel, helium technology, and some important components resulted from the successful operation of this plant. Here are the key specifications of the PB reactor [11]:

- Thermal Power: 115 MW,
- Power Density: 8.3 MW/M^3,
- Secondary Coolant: Steam (modern fossil steam conditions, no reheat),
- Primary System Pressure: 2.3 MPa,
- Primary Inlet Temperature: 327C,
- Primary Outlet Temperature: 700-726C,
- Vessel Material: Carbon Steel,
- Core Type: Prismatic Blocks,
- Years of Operation: 1966-1974.

2.1.1.3 AVR Plant Description (Germany)

AVR (German: Arbeitsgemeinschaft Versuchsreaktor) was one of the first reactors built in the Federal Republic of Germany located at the Julich Research Center [12]. It used a pebble bed type core, with the fuel contained in 6 cm diameter graphite spheres. These spheres contain the TRISO and BISO fuel particles in the centre 4 cm region of the fuelled spheres. During the operation, the spheres were circulated out of the reactor, where the fuelled spheres were evaluated for burn-up by means of a high-resolution gamma spectrometer. The spheres with high enough burn-up were removed from the reactor; spheres with sufficient remaining fuel were returned [9]. Reactor's shutdown is done by four absorber rods which are introduced into graphite noses, which reach into the core region, to allow a higher worth of the control rods.

One of the most significant operational occurrences at AVR was a steam generator leak that developed at the beginning of or during a 1978 plant shutdown to repair a safety valve. AVR normally experienced some increase in helium moisture during shutdown; in this case when the reactor was restarted, the moisture levels increased enough to require plant shutdown.

Investigation revealed that a 1-3 mm^2 leak had formed in one steam generator [13]. Since the steam generators were located above the core, this leak resulted in a significant amount of water in the system. Because AVR did not have a low-point drain to remove bulk water from the vessel, removal of the water and repair of the steam generator required a 15-month shutdown. AVR did not use a cross-vessel type of construction, instead having the steam generators above the core in a single vessel [8].

In the AVR, many types of fuel elements have been tested. The LEU fuel elements with TRISO particles showed an excellent fission product retention capability. Different safety experiments regarding the nuclear and thermal stability in extreme situations have been conducted as well. It was shown that the reactor core would not melt or superheated to unallowable high temperatures after a total loss of active cooling.

The AVR confirmed the feasibility of a pebble-bed reactor as well as the expected excellent operating performance of a helium-cooled, graphite-moderated nuclear reactor. The AVR and its components techniques are a basis especially for the further development of the small-sized modular HTR reactors. Here are the key specifications of the AVR reactor [11]:

- Thermal Power: 46 MW,
- Power Density: 2.6 MW/M^3,
- Secondary Coolant: Steam (modern fossil steam conditions, no reheat),
- Primary System Pressure: 1.1 MPa,
- Primary Inlet Temperature: 275C,
- Primary Outlet Temperature: 950C,
- Vessel Material: Steel and Concrete Building,
- Core Type: Pebble Bed,
- Years of Operation: 1967-1988.

2.1.1.4 HTTR Plant Description (Japan)

The high-temperature test reactor (HTTR) has been built in 1999 and is located on the Japanese Atomic Energy Agency campus (Tokaimura, Japan). HTTR is a prismatic fuel type HTGR reactor featuring a steel RPV connected to heat exchangers that cool the outlet helium (there is no power conversion equipment at this research reactor) by means of a secondary helium loop [14-19]. This transfers heat to pressurized water heat exchangers, and these in turn reject heat to the atmosphere. The RPV is connected to the heat-exchanger vessel by a cross-

vessel. The main purpose of this reactor is to establish basic technology for advanced HTGR in the future and to get an irradiation test reactor to conduct research in the field of innovative high-temperature technologies.

The reactor core consists of prismatic fuel elements. The active core contains 30 fuel columns and seven control rod columns, each column composed of five blocks stacked one upon the other. The reactor shutdown under the high-temperature condition is made by inserting nine pairs of control rods into the reflector region at first, then the other seven pairs of control rods in the core region are added after the temperature of the region is reduced. Refuelling is performed after the reactor is shut down and depressurized. The reactor pressure vessel is made of 2-1/4Cr–1Mo steel. The 2-1/4Cr–1Mo steel has better creep strength at high temperature than Mn-Mo steel, which is widely used in the pressure vessels of light water reactors [19].

Recently, JAERI has stressed the importance of research and development on the hydrogen production considering significance of hydrogen as an energy carrier for energy security and prevention of global climate change. Here are the key specifications of the HTTR reactor [11]:

- Thermal Power: 30 MW,
- Power Density: 2.5 MW/M^3,
- Secondary Coolant: He/Pressurized Water,
- Primary System Pressure: 4 MPa,
- Primary Inlet Temperature: 395C,
- Primary Outlet Temperature: 850-950C,
- Vessel Material: 2-1/4Cr-1Mo Steel,
- Core Type: Prismatic Blocks,
- Years of Operation: Startup in 1998.

2.1.1.5 HTR-10 Plant Description (China)

HTR-10 (high-temperature gas-cooled, pebble-bed reactor) is a helium-cooled, pebble-bed reactor, located at Tsinghua University in Beijing, China, very similar in construction to the Siemens design for a HTR module [20-25]. The core consists of pebble fuel and contains low enriched uranium dioxide in TRISO particles. The fuel elements are cycled several times through the core before they reach final burn up.

HTR-10 has two independent reactor shutdown systems: one is the control rod system and the other is the small absorber ball system. They are both placed in the side graphite reflector

and are able to bring the reactor to cold shutdown conditions. The HTR-10 uses helium gas as coolant, which has thermal and chemical stability, good compatibility with the core graphite material and metallic material of the primary system at high temperature condition; in addition, there is no phase transition.

The reactor core is designed and laid out such that a maximum fuel element temperature of 1600 °C is not exceeded during any accident. Due to the high activity retention of the fuel elements, a pressure-tight reactor building is not necessary. The reactor building is accessible for repair work at any time after an accident because of the low activity release. The reactor is named to be inherent safe because fuel temperatures higher than 1100 °C never can occur even in very hypothetical accidents. It is planned to demonstrate this behaviour of the system in an experiment. Here are the key specifications of HTR-10 reactor [25]:

- Thermal Power: 10 MW,
- Power Density: 2 MW/M^3,
- Secondary Coolant: Steam,
- Primary System Pressure: 3 MPa,
- Primary Inlet Temperature: 250C,
- Primary Outlet Temperature: 700C,
- Vessel Material: C-Mn-Si Steel,
- Core Type: Pebble Bed,
- Years of Operation: Start-up in 2000 – still operating.

2.1.2 Prototype HTGRs

2.1.2.1 THTR Plant Description (Germany)

The Thorium High Temperature Reactor (THTR) was built near the city of Hamm Uentrop in the Germany and was turned over to the operating utility on 1987 [11, 26-27]. The fissile and fertile material of this pebble-bed type reactor was contained in BISO particles which are embedded in a special pressed graphite matrix. Each fresh fuel element contained 10.2g of ThO_2 and 0.96g UO_2, which was enriched to 93%. The fissile and fertile materials are mixed in the same coated particle. Overall, this represents an enrichment of around 8.6% for fresh fuel elements. A graphite reflector surrounds the active reactor core. Arranged around the reactor core are six steam generators consisting of helix-shaped tube bundles, inside which the heat of the helium is used for steam production. The adjustment and shutdown of the plant are

performed by 36 reflector rods and 42 core rods, which are directly introduced into the pebble bed.

In the THTR, a normal industrial building is realized instead of a dense reactor containment. This solution was similar to that of Fort St. Vrain (FSV) and of AGR plants. The reason for this design choice was the use of a PCVR, which had additionally double closures for all penetrations.

One of the key features of THTR was that all safety requirements originating from LWR licensing processes and applied to the THTR were fulfilled during the construction time. These additional requirements were the main reason for a long time of construction. The operation demonstrated that a pebble-bed HTR with a medium power level can be operated with a similar robust dynamic behaviour as already known from the AVR.

During an inspection of one of the hot gas channels in the year 1989, the operator detected that some of the metallic bolts which fixed the cover plates of the insulation of the hot gas ducts were broken (35 bolts from 2600) in the six hot gas channels, however the safety authorities decided that this would not cause any difficulty for further operation. Despite the initial problems, caused by a new technology and the prototype characteristics, the THTR delivered significant contributions to the HTR technology. Here are the key specifications of THTR reactor [26]:

- Thermal Power: 750 MW,
- Power Density: 6 MW/M^3,
- Secondary Coolant: Steam (modern fossil steam conditions, with reheat),
- Primary System Pressure: 4 MPa,
- Primary Inlet Temperature: 404C,
- Primary Outlet Temperature: 777C,
- Vessel Material: PCRV with Liner,
- Core Type: Pebble Bed,
- Years of Operation: 1985-1991.

2.1.2.2 FSV Plant Description (USA)

Fort Saint Vrain (FSV) was located in Platteville, Colorado. FSV, the only commercial HTGR to operate in the United States, was built under the Atomic Energy Commission Reactor Demonstration Program [28-29]. The core, the steam generators, and the helium circulators

were integrated into a large pre-stressed concrete reactor vessel (PCRV). There were twelve steam generators and four helium circulators arranged in the bottom part of the reactor vessel. The PCRV shields the reactor and the helium circuit. The PCRV contains an insulation layer, a steel liner and because cracks in the wall never can grow, the PCRV is said to be burst-protected.

The core consists of hexagonal-shaped graphite fuel elements, stacked in vertical columns. It is arranged in the upper section of the PCRV cavity. A graphite reflector surrounds the active core, around this there is a borated side reflector and an outer core barrel made from steel. The hexagonal fuel elements are grouped into 37 fuel regions and are refuelled as units. The control of the reactor is done by 74 control rods, which move vertically within holes in the graphite fuel elements. Absorber material is boron carbide in metallic tubes.

FSV suffered from operational problems and by the mid-1980s was confronted with rising maintenance, operations, and fuel costs. In 1988 the Board of Directors of the Public Service Company of Colorado decided to shut the plant down on 1990 [29]. In late August 1989, during a shutdown to repair a faulty control rod drive, a steam leak was discovered in the main steam ring header, and further inspections revealed more cracking. Faced with the considerable expense required to repair the ring header, the company decided to permanently shut FSV down on August 29, 1989 [28].

The reactor, the primary arrangement, and components of which were prototypical, brought in much experience for the technology of larger HTR plants and is now partly, especially with fuel and core internals, the basis for the US program for modular HTR. Here are the key specifications of FSV reactor [29]:

- Thermal Power: 842 MW,
- Power Density: 6.3 MW/M^3,
- Secondary Coolant: Steam,
- Primary System Pressure: 4.8 MPa,
- Primary Inlet Temperature: 404 C,
- Primary Outlet Temperature: 777 C,
- Vessel Material: Pre-stressed Concrete Reactor Vessel (PCRV),
- Core Type: Prismatic Block,
- Years of Operation: 1976-1989.

2.1.3. Commercial HTGRs

2.1.3.1 PR-500

From 1967 to 1974 the PR-500 [30] has been designed and analysed as a reactor with a thermal power of 500 MW for co-generation processes. The reactor was thought to be able to deliver high-temperature process heat too. It was planned mainly to produce process steam with a temperature of 265 °C for industrial application. The pebble-bed core was planned to use the OTTO cycle for the fuel elements handling. The heating up of helium was planned to be between 250 and 850 °C. The core was arranged in a pre-stressed concrete reactor pressure vessel, and three loops for steam production were connected to the reactor using coaxial gas ducting systems.

The reactor containment was planned to be arranged underground and should be covered with a hill composed of gravel, concrete and other suited materials. The reason was the protection against airplane crash, gas cloud explosions, and terrorism.

The decay heat removal was planned to be carried out by the three steam generator loops and if these installations had failed, the redundant liner cooling system of the reactor pressure vessel would cool the system.

The PR-500 has been designed as a cogeneration plant with a simplified fuel management. Analysis of the economic conditions to that time of the HTR development showed that the products process steam and electricity should be cheaper than those from oil or coal (Europe conditions). It was envisioned that the necessary technology already would be available.

2.1.3.2 HHT Reference

In Germany between 1968 and 1982, the HHT project (high-temperature helium turbine) was conducted in an international cooperation with the USA and Switzerland [31]. It was an extended project with the goal to develop a commercial power plant with the Brayton cycle and HTR as heat source. During this work, many flow sheets have been worked out, different thermal power of the plant and the use of a pebble-bed core and of a core with block-type fuel elements have been investigated. The thermal power of this plant was foreseen as 1640 MW, the net efficiency was 40.5%. The primary system was arranged in a large reactor pressure vessel. The maximal helium temperature was planned to be 850 °C and the maximal helium pressure was 6 MPa.

During the HHT project, the possibility of combined cycles has been analysed too. This process is a further interesting option for future developments in nuclear technologies. The analysis delivered as example for a helium inlet temperature into the turbine of 900 °C.

2.1.3.3 HTR 500 Reactor

The HTR 500 was designed as follow-up project after the THTR as a base load plant or for cogeneration [31-32]. Dependent on the requirements of the consumers steam till temperature of around 500 °C can be delivered. Normally, the steam shall be given off using the introduction of a steam transformer. This allows a strict separation of the nuclear and of the conventional part of the plant and serves to reduce a possible tritium contamination of the products.
The fuel cycle is LEU using TRISO particles, and it was planned to realize the OTTO cycle, which means that the elements pass once through the core and then were taken out having reached their full burnup. The helium would be heated up between 250 and 730 °C, and the quality of steam should be 530 °C/18 MPa. It was planned to operate the plant without internal reheat. The shutdown installations contain absorber rods in the side reflector and in core rods, which are directly inserted into the pebble bed as in case of THTR.

The HTR 500 was thought to be either an electricity generating plant with a net efficiency of 40% or a plant for delivery of electricity and process heat. In this case of application, the total use of primary energy would be around 85% or even more. The economic analysis of the company HRB in the late 80s resulted in the statement that the HTR 500 would be competitive to a large PWR.

2.1.3.4 HTGR 1160 Reactor

The concept of HTGR-1160 with block-type fuel elements was developed and nearly commercialized in the USA from 1970 to 1980 [33]. A detailed planning of this concept was conducted for the German market too. Eight large plants of this type were sold to utilities, but later these projects have been cancelled because of different developments in the American energy economy.

The core consists of block-type fuel elements as they have been operated in the For St. Vrain. The reactor was a pod boiler system with a thermal power of 3000 MW, and the conversion cycle was the steam cycle. The reactor was planned to use discontinuous refuelling during shutdown, and the fuel elements were similar to that of Fort St. Vrain. The fuel cycles were planned to use the system uranium carbide and thorium in different coated particles

(TRISO for feed particles and BISO for breed particles). The reactors were planned to use the thorium cycle with high burnup and high conversion factors. The average core power density was 8.4 MW/m^3, and the core should consist of 493 columns of fuel elements, each with eight elements. The heating up of helium in the core should be 319-741 °C at a pressure of 50 bar.

Safety aspects and economy of this plant in totally were estimated promising compared to the commercially introduced nuclear power plants at that time.

2.1.3.5 PNP Prototype

The VHTR (very high temperature reactor) was a first integrated concept using a prestressed concrete reactor pressure vessel with integrated heat exchangers in the pods in the wall of the vessel PNP (prototype nuclear process heat) project [11]. The central cavity in the PCRV should contain the reactor core with a thermal power of 500 MW. In the cylindrical wall of the vessel, there should eight positions for heat exchangers.

The reactor was planned to use the OTTO cycle, and therefore the maximal fuel temperature in normal operation was expected to be around 1050 °C for a design with an average helium outlet temperature of 950 °C. Shutdown and control of the reactor used two systems consisting of absorber rods. The first system should move in borings in the side reflector, the second system should use in core rods, which should penetrate into the core with NH_3 lubrication to reduce friction and forces. The maximal fuel temperature in case of the very severe accident "total loss of coolant and total loss of active decay heat removal" was estimated to be around 2200 °C.

Based on the concept of modular HTR for the steam generation process (thermal power 200 MW) a modular HTR plant with a thermal power of 170 MW has been proposed as a universal heat source together with an IHX. Therefore, it would be possible to operate the heat exchanger in normal operation nearly without pressure differences between the primary and secondary side. This allows a design with high safety reactors even at high material temperatures.

2.1.3.7 PBMR Concept

The PBMR (pebble-bed modular reactor) [11] was developed and planned to be built in the future in South Africa. The plant used the Brayton cycle for power production.

The heat source for this plant should be a pebble-bed reactor with a power of 400 MWth. The maximal helium temperature will be 900 °C. The hot helium leaving the reactor with a temperature of 900 °C should enter the turbine, which is connected to the generator through a speed reduction gearbox on the one side and by two compressors on the other side. The helium enters the core then with a temperature of 470 °C. The coolers are water cooled. The power of the plants is proportional to the mass flow and the mass flow depends on pressure.

As fuel element, the spherical fuel clement containing TRISO particles will be used. The core is an annular core, the inner zone consists of a graphite column, and the outer zone consists of fuel elements.

The boundary condition is that the maximal fuel temperature stays below 1600 °C in severe accidents. The fuel cycle is the MEDUL cycle using low enriched uranium. Control and hot shutdown of the reactor are conducted by reflector rods. The first shutdown system includes rods; the second shutdown system consists of small absorber balls made from boron carbide.

The concept of PBMR has been worked out in detail. In the meantime, the project was finished, mainly because of changing politics of the interested utility and shortage of funding.

2.1.3.8 The ANTARES Project

The ANTARES (Areva New Technology, based on Advanced Gas-cooled Reactor for Energy Supply) project is carried out in France to develop a HTR solution for the future energy market [11]. It includes two main applications: steam generation to supply a cogeneration or a condensation plant and production of high-temperature process heat to be used via an IHX for different processes.

The heat source for ANTARES is an HTR with block-type fuel elements, as was developed by General Atomic. It is an annular core with a thermal power of 600 MW and a power density of 5 MW/m^3.

The helium flows from top of the reactor to the bottom and is heated up to 750 °C for steam generation and up to 1000 °C for process heat application. At the bottom, there is a hot gas chamber, formed from ceramic components. The reactor and the heat exchanger are connected by a coaxial duct. The control of the reactor is done by absorber rods, which are inserted from the top into the core.

The primary system is positioned in an inner concrete cell which is equipped with a surface cooler around the reactor pressure vessel for the removal of the decay heat. The inner concrete

cell itself is surrounded by the outer reactor building. The maximal fuel temperature would stay below 1600 °C because of annular core usage.

2.2 Review of Progress in Coated Fuel Particle Performance Analysis

High-temperature reactors are one of the most likely types of 4th generation reactors to be constructed in the near future [34]. There are different designs of these reactors, but typically the fuel is in the form of a coated particle. Because of the high temperatures of the fuel, the properties of the layers of the coated particles are fundamental to the safety of these reactors. In case of TRISO particles, the surrounding layers function as a containment vessel for the fission products. Therefore, the technology of TRISO fuel is the key factor for high temperature gas cooled reactors. It allows coolant outlet temperatures in excess of 950 °C and contributes to enhanced reactor safety. TRISO fuel manufacturing process has been developed since 1960 and several fuel qualification programs are currently in progress in many countries [35]. TRISO particles typically consist of five distinct regions (Figure 2.1):

1. fuel kernel, which contains the nuclear fuel (uranium, plutonium, thorium, or other transuranic elements),
2. a porous carbon buffer, which surrounds the kernel to attenuate recoiling fission fragments and to accommodate internal gas buildup and particle dimensional changes,
3. an inner pyrolytic carbon (IPyC) layer, which surrounds the buffer layer to protect the SiC layer from chemical attack during TRISO particle operation and acts as an additional diffusion barrier to fission products (FPs),
4. a silicon carbide (SiC) layer, which surrounds IPyC layer and acts as the main pressure vessel for the particle, withstanding the stresses from internal gas pressure buildup and mechanical forces as well as provides a diffusion barrier to prevent the release of gaseous and metallic FP,
5. an outer pyrolytic carbon (OPyC) layer, which surrounds SiC layer and protects it from mechanical damage during the manufacturing process.

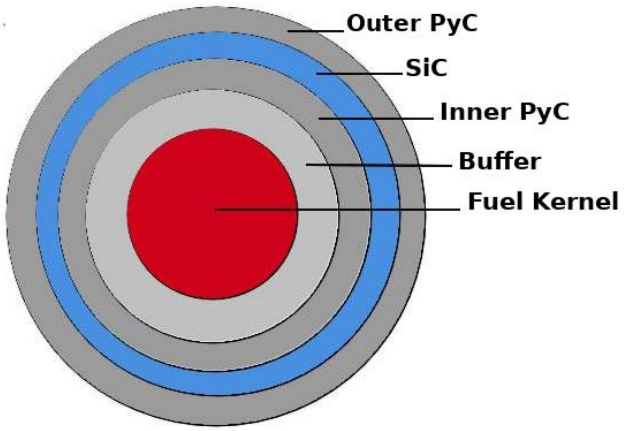

Figure 2.1: TRISO fuel particle geometry

In order to estimate the behaviour of the coated fuel particle, it is necessary to address all the phenomena occurring in the system during the operational and accidental conditions. Many studies have been performed to find the fuel failure mechanisms and important phenomena influencing coated fuel particle integrity in the past. The main objective of this Chapter is to provide a basic understanding of important phenomena in TRISO fuel performance analysis, review current modelling capabilities and to point out open questions for future studies. In this thesis, the phenomena are divided into three categories as follows: general phenomena (which includes: pressure buildup in buffer layer, anisotropy effects, heat generation and transfer from the kernel, kernel migration, fission products buildup and release), chemical phenomena and mechanical phenomena.

2.2.1. General Phenomena

2.2.1.1. Pressure Buildup in Buffer Layer

The pressure buildup in the buffer layer of TRISO fuel has a huge importance for fuel performance analysis. High pressures can result on TRISO vessel mechanical failure. Pressure buildup in coated fuel is a result of three main contributors: gases produced during the fission (mainly noble gases), gases formatted during oxygen interaction with carbon layer (CO, CO_2) and ternary fission (mainly helium). The pressure in the buffer layer is an input parameter for other important phenomena (such as kernel migration, fission product release), therefore a high accuracy is needed during the modelling process. To predict the pressure in the buffer layer two main methods are used: the ideal gas law [36, 37] and the method of Redlich and Kwong

[38]. Both methods require information regarding fission gases and oxygen (released in the buffer layer) and for both cases the empirical expression (proposed by Proksch [39]) is used to calculate the amount of oxygen. Although the method of Redlich and Kwong is currently the best-adapted method, there is still a need for more studies to increase the accuracy of the model. This model assumes that the pressure in the buffer layer is created only by CO, CO_2, Xe and Kr gases, therefore the contribution of other fission gases and volatile FPs are not considered (even if their contributions are relatively small [40]).

2.2.1.2. Anisotropy Effects

Dimensional changes of graphite blocks under irradiating conditions have a critical importance on the design and operation of HTGR reactors' fuel. When graphite blocks are produced by extrusion or pressing, the layer planes of the graphite crystallites are distributed preferentially (parallel to the extrusion direction or perpendicular to pressing direction). To visualize the orientation of graphite planes, the transmission electron microscope images are illustrated in Figure 2.2. Four different deposition conditions are examined to show the changing growth features in a single layer of PyC coatings. More details can be found in [41].

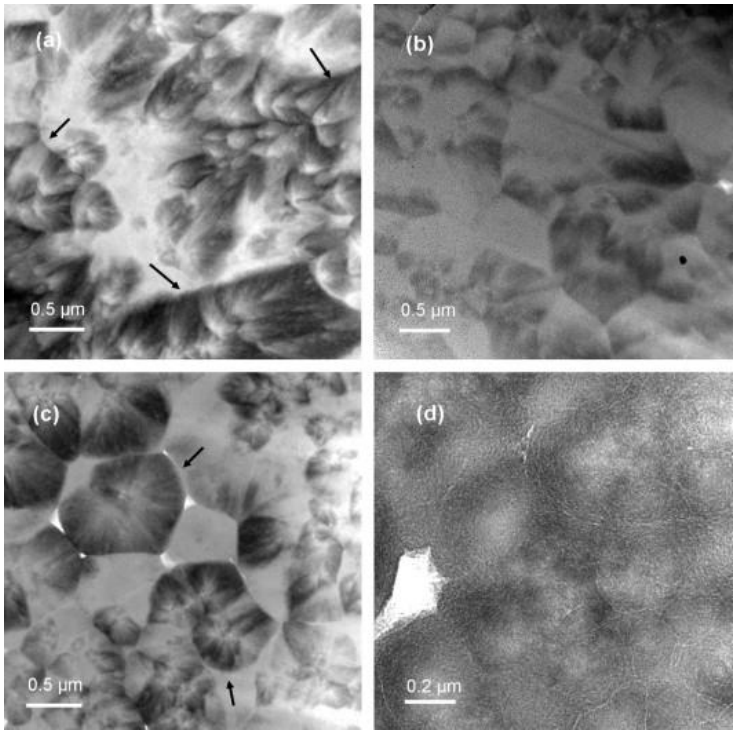

Figure 2.2 Transmission electron microscope images for deposition conditions (a-d) [42].

Recent studies have shown that dimensional changes of graphite crystallites under irradiation are anisotropic [42]. To characterize the level of orientation of materials the Bacon anisotropy factor (BAF) [43] is used. The value of BAF can vary from 1 to infinity. If BAF=1, it means that the layers in material are distributed randomly (isotropic). Several studies and experiments have been performed to estimate the anisotropy factor of the PyC used in TRISO fuel [44]. For the graphite used in the 1970s, the BAF was reached to 1.26. However, during the development of PyC formation technique, JAEA developed a new artificial graphite (IG-110), which is currently used by most HTGR reactors. It has been shown that anisotropy factor for this type of graphite is very small (maximum value of BAF is about 1.05) [45].

2.2.1.3. Heat Generation and Transfer from the Kernel

The heat generation and temperature distribution in any substance can be calculated by the energy balance equation. Based on the structure of the coated fuel compacts, there are two regions that have to be considered: temperature distribution in fuel particles and in fuel pellets (or pebbles). For fuel particles, the problem is relatively easy, while calculating temperature distribution in fuel pellet (or pebble) is more challenging, as the distribution of fuel particles in graphite mixture is not uniform. The homogenization methods [46] or Monte-Carlo based methods [47, 48] are commonly used for the assessment of the temperature. In case of fuel particles, homogenization methods work well until the debonding of the particle layers occurs. Despite the low conductivity of a potential interface gap, enough of the heat will flow through additional particles before reaching the coolant to noticeably affect the centreline temperatures of the pebbles especially at high power density and particle packing fractions. As a result, it often becomes necessary to estimate the gap widths, which are dependent on irradiation induced dimensional changes (IIDC), creep and gas pressure. This effect is mainly considered using proper values for thermal conductivity coefficient. The uncertainty analysis is recommended to get the clear picture of this phenomenon. The following numerical methods are mainly used for temperature distribution assessment:

1. Finite element method [49],
2. Boundary element method [50],
3. Finite differences method [36].

For the simple conditions/geometry, the finite difference method has a good precision level and can be used. While in more complicated cases, the finite element and boundary element methods are recommended.

2.2.1.4. Kernel Migration

Kernel migration is a movement of the fuel kernel towards TRISO coated layers. The driving force for the kernel migration is extreme operating conditions and asymmetrical kernel production during manufacturing [51]. This phenomenon is also known as an "Amoeba effect" and mainly depends on power density, temperature, and temperature gradient across the fuel particle (Figure 2.3).

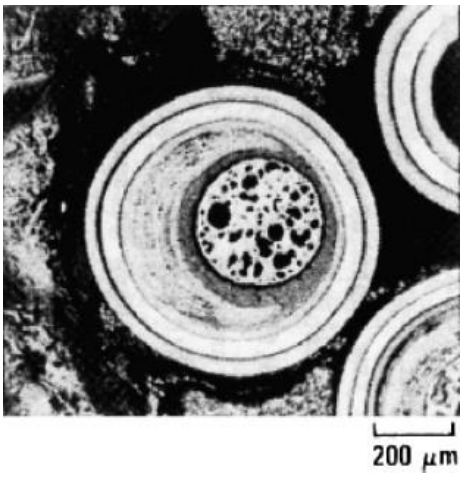

Figure 2.3 Micrograph showing kernel migration in a TRISO particle [52].

Prismatic fuel elements have higher susceptibility for kernel migration compared to pebble bed fuel elements because of the presence of a more severe temperature gradients. Temperature gradients lead to carbon transport from the hotter side to the colder side of the IPyC layer, which causes movement of the kernel in the opposite direction. Experiments on this effect were conducted in the past and the results have shown no coated particle failure. However, experimental data on kernel migration distances from irradiation tests were gathered and a correlation between the kernel migration rate and temperature was found [53].

Although kernel migration has a small influence on fuel failure fraction within operating conditions [54], it could influence other phenomena occurring in the TRISO fuel (such as SiC degradation, fission gas release, etc.). It increases the probability of interaction with IPyC and SiC, and therefore the chemical degradation of coating layers is more likely. Therefore, models which are predicting the fuel performance dependent on kernel migration [55], include many parameters (for above-mentioned dependencies) and the results have significant amount of

uncertainties. The sensitivity and uncertainty analysis are recommended to analyse the real impact of kernel migration on TRISO fuel failure fraction.

2.2.1.5. Fission Products Buildup and Release

Buildup of FPs in the fuel kernel of TRISO particle plays an especially important role in fuel performance analysis. FPs can influence pressure buildup in buffer layer, chemically interact with coating layers of the fuel particle and decrease the strength of the particle. FPs can also release from the coated particles, and as a result, increase the activity level (therefore exposure to workers) in the primary circuit. The amount of FPs depends on several factors, but primarily on burnup. Therefore, the phenomenon of fission product release is one of the most significant issues for coated fuel particle safety analysis and it is the main indicator of the fuel performance. The FPs, which can be released from the fuel kernel, are usually classified into two groups: fission gases and metals. There are several methods developed for each group to estimate their release fractions from the fuel particle [51].

2.2.1.6. Fission Gas Release Models

The Booth model [56] developed in the 1950s is commonly used to estimate fission gas release (FGR) from the TRISO. Because of its simplicity, there are several limitations of the Booth model, such as:

1. the gas phase transport in the interconnected porosities in fuel kernel is not considered, and the model describes only the gas release from a fuel grain,
2. the effect of burnup on the micro-structural changes in the kernel is not captured with this model,
3. the release of some metallic fission products (such as Ru, Mo, Tc, Pd) which tend to form nodules along grain boundaries in the fuel, is not considered by this model.

Therefore, many studies were conducted to remove these assumptions from the Booth model. These include the trapping of gas atoms by matrix defects and the resolution of gas atoms from bubbles by fission spikes. Currently, the following models are commonly used in FGR performance analysis [18]:

1. The KFA model (German) for fission gas release from defective fuel particles [57]. This model distinguishes between different components, grains, and pores, of both the particle kernel and the buffer layer. It also describes the steady state fission gas and

iodine release from defective particles, recoil effect and graphite contamination, by using an uncoupled two-phase (grain, pore, or grain boundary) diffusion model, but considers no sorption effect on graphite surfaces [58].

2. The ORNL model (American) for steady state FGR from fuel particles with exposed kernels [59, 60] which considers (empirically) the effects of burnup, temperature, the mechanisms of a thermal diffusion and vacancy (common defects in bulk materials) migration [61, 62]. The irradiation induced, intrinsic diffusion and a buffer-recoil contributions are included in the model [63].
3. The GAC model (American) for transient FGR from fuel particles with exposed kernels, which accounts for transport, trapping, and emission of diffusants [64, 65].
4. The JAERI model (Japanese) for short-lived noble gas release from failed coated particles and matrix contamination [66], which is based on an empirical equation generated from previous irradiation experiments.
5. Another JAERI model (Japanese) for oxide fuel, which is based on a modelling approach developed in Canada [67]. It takes into account diffusive transport in the oxide fuel, partial retention of gas in trapping sites, and a possible resolution of trapped gas with subsequent diffusive transport.
6. The method developed by G. Momot (Russian) of determining the fission gas and iodine release under operating conditions is characterized by a temperature dependent release velocity (equivalent to a change of the activity per unit time) of the nuclides out of a core volume element [68].

2.2.1.7. Fission Metal Release Models

The transient release behaviour of (long-lived) metallic FPs are usually predicted by using diffusion models. TRISO particles' SiC coating layer represents an efficient barrier against FPs release at operation temperatures [69]. Therefore, the most important data for coated particle performance are the fractions of defective/failed coated particles and the fractions of heavy metal contamination in the fuel element graphite. It is essential to know the transport data of heavy metals in kernel material and fuel element graphite. The following models have been used to model the metal release from TRISO particle:

1. The diffusion model FRESCO [70] which was widely used under irradiation and elevated temperature conditions. This model includes specific irradiation effects such

as recoil and the buildup of fission product inventories dependent on the decay constant. It is based on effective diffusion coefficients for the fission product species in the different fuel materials. Later, the KFA diffusion code SPTRAN [71] has been modified for use under operating conditions [72]. No significant difference in the method of modelling fission product release from the fuel can be detected between this code and FRESCO.

2. The JAERI computer code FORNAX [73] is similar to the diffusion code FRESCO in describing the metallic fission product release from the particle kernel. Three types of fuel particles are considered in this model: standard (intact) particles, failed particles (exposed kernels) and particles with a degraded SiC layer simulated by a larger diffusion coefficient.
3. The GA codes COPAR2 [74] and TRAFIC-FD [75] determine the release of metallic fission products from the HTGR core into the primary coolant circuit. The codes model a one-dimensional Fick's migration through the fuel particle, fuel compact, and structural graphite to the coolant-graphite surface.

Recent studies and experiments for operating and accidental conditions show that there is a limited number of fission gases and metals which are relevant for fission product behaviour analysis [76]. In particular, the number of relevant fission gases and metals mainly depend on the modelling conditions (operating history, short-lived or stable nuclide, heat up rate, etc.). All the above-mentioned diffusion models are using diffusion coefficient [77] for predicting FG and metal release from the TRISO particle. However, there is a lack of experimental data for several fission gases and metals, therefore additional research is needed to get a clear picture of this phenomenon.

2.2.2. Chemical Phenomena

The release behaviour of FPs from TRISO fuel is dependent on its chemical state and temperature. In the case of UO_2 kernels, the chemical state of each FP is strongly dependent on oxygen potential, temperature, and its composition [78]. In coated UO_2 fuel particles, oxygen reacts with PyC to form carbon monoxide, which influences the oxygen potential of the fuel. SiC layer of TRISO fuel acts as the main barrier against the release of metallic FPs during operation and adds to the structural integrity of the TRISO particles. The SiC layer, however, has been found to be susceptible (see Figure 2.4) to chemical attack (mainly from Pd and Ag).

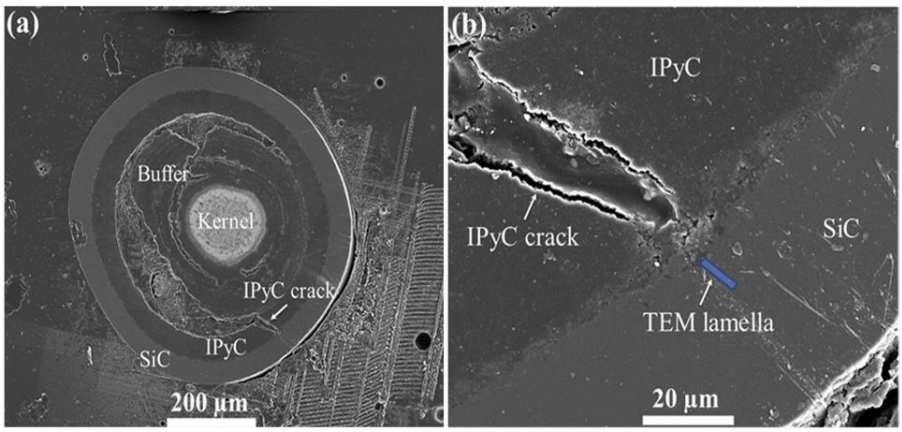

Figure 2.4: Scanning electron microscopy images of the cross section of the studied TRISO particle [79].

Several studies and experiments have been performed to estimate the behaviour of fission products in the TRISO particles [80-91]. The following was observed:

1. Palladium and silver accumulated at the inner surface of the SiC layers and sometimes reacted with the SiC layers, which is the key factor influencing the fuel performance,
2. Rhodium and ruthenium were also detected at the corroded areas in some particles,
3. Tellurium was often observed in the buffer PyC layers, but it did not penetrate through the IPyC layers,
4. Cerium and barium were observed at the interface of the IPyC/SiC layers of the particles. Both interacted with the IPyC and the SiC layers,
5. Caesium was observed in the buffer PyC and the IPyC layers. In contrast with the cases of palladium, tellurium, cerium and barium, no high concentration of Cs was observed.
6. The noble gas xenon was also retained in the buffer PyC layer with low concentrations (similar to Cs).

In recent publications [92-96], the transport of silver in association with palladium silicide in SiC was studied. The presence of silver in palladium silicide and the migration of palladium, silver, and silicon solutions in the form of nodules along grain boundaries of the SIC layer were observed. Experimental temperatures were comparable to the reactor operating temperatures. Similar findings were reported in [92], where nodules consisting of Rh, Pd, U and Si were observed along SiC grain boundaries. The relation between the observed Pd-SiC reaction depth and the calculated amount of palladium near SiC layer was found in [79].

Although many studies addressed the high temperature performance of SiC in TRISO during the last years [97, 99], the available data is still limited. Developed models are mainly considering short term irradiation and simplified environment (mainly the chemical elements with high concentrations are considered), especially for oxidation and corrosion processes. A better understanding of the chemical phenomena occurring in TRISO fuel at normal and extreme conditions is still necessary (including also chemical elements with low concentrations) for the development of the fuel design and improvements of current modelling codes.

2.2.3. Mechanical Phenomena

Mechanical behaviour of TRISO coating layers is playing a key role for predicting stresses limits and therefore determining failure probabilities of the fuel particles. To assess the mechanical behaviour of the TRISO fuel, the tangential and radial stresses should be calculated. Many parameters relevant to TRISO fuel have to be considered during the stress assessment process, such as neutron flux, anisotropy behaviour of different layers, material properties (such as grains, pores), gas pressure, etc. Figure 2.5 shows the TRISO fuel particle failure from several experiments.

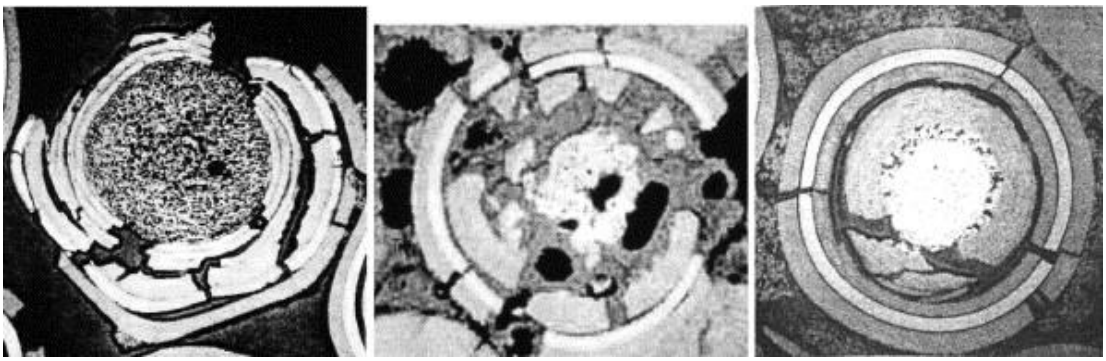

Figure 2.5: Pressure vessel failure in a fertile fuel particle from HRB-14, a UO_2 particle from HRB-8 and UC_2 particle from P13T [31].

The mechanical properties of the SiC layer of TRISO particles have been explored with different techniques including the ring test method [100, 101], the crush test [102-104], the micro-cantilever test [105] and indentation methods [106, 107]. The following features of TRISO fuel have been investigated in the latest studies:

1. Post-irradiation examination showed the presence of radial shrinkage cracks in the IPyC and OPyC layers, partial deboning between buffer and IPyC layers, as well as between IPyC and SiC layers.
2. It was shown that shrinkage cracks in the IPyC layer can contribute significantly to the failure of fuel particles [108]. Therefore, multidimensional effects (such as shrinkage cracks in IPyC layer, partial debonding between layers and asphericity) may have led to unexpectedly large number of failures of particles.
3. The grain size in SiC layer is not constant and grows considerably with thickness [100-110]. Since grain size has an important effect on the diffusion of fission products and on the mechanical properties of ceramic materials, this change in grain size could be destructive to the properties of SiC [99, 111]. The following factors should be considered while controlling the thickness of SiC layer. Increasing the thickness, the grain sizes will increase, which has a negative effect on mechanical performance (at some point it increases fission products release rate). On the other hand, with increasing SiC thickness the thermal conductivity is decreasing, which then also reduces the strength of the material. While decreasing the thickness of SiC layer will directly decrease the mechanical strength of the layer.
4. During the production of coated particles the deposition of SiC at 1500 °C is occurring. It has been reported that the deposition at this temperature results in an increase in coating density and anisotropy [112]. This increase in anisotropy could also seriously reduce the performance of these coatings, since higher anisotropies result in a higher probability of coating failure [113, 114]. In general, the following issues are considered while choosing the deposition temperature for SiC. First, increase in deposition temperature will increase the anisotropy in the material and grain sizes, which has negative effect on mechanical characteristics. While increasing the deposition temperature will increase the hardness and strength of the material.
5. PyC initially shrinks, and later swells, when irradiated with fast neutrons. The seminal Combustion Engineering-General Atomics (CEGA) report [115] defined this as Irradiation-Induced Dimensional Change (IIDC) and provided a reasonable description of the process. More detailed descriptions can be found elsewhere [116, 63]. SiC undergoes a similar irradiation-induced volumetric change, however, it has a negligible impact on the release rate for the most FPs [117].

Early models of coated fuel particles used iterative numerical procedures to include the effects of pyrocarbon creep and swelling in determining stresses in the coating layers. Later, closed form solution for a single layer significantly increased the speed for calculating stresses, making it possible to perform Monte Carlo investigations of particle behaviour. The effects of assuming a Gaussian distribution for kernel diameter and buffer thickness on particle failures was studied and Bongartz [118] added the effect of a Weibull distribution for SiC strengths. A comprehensive model then developed during the Dragon project [1]. Bongartz [119] simplified the stress analysis with a closed form solution based on the assumption of a rigid SiC layer, which enhanced the speed of Monte Carlo calculations. Miller and Bennett [120] derived a closed form solution for a three-layer particle, allowing for a flexible SiC layer. All of these are one-dimensional models used to evaluate a failure of the coating layers. In order to represent the multidimensional behaviour associated with anomalies such as shrinkage cracking, partial deboning, and asphericity, PARFUME [116] code was developed at INL. It utilizes detailed finite element analysis on a cracked particle (using the ABAQUS program [121]) to make a statistical approximation of the stress levels in a particle. Weibull's statistics, combined with fracture mechanics, are typically used to describe failure in these materials. The load-dependent stress field in coating shells is believed to be the main cause of the varied Weibull modulus. Further study for modifying the size effect (both for fuel kernel and coating layers) analysis is recommended.

Although many other modelling tools have been developed over the last years [122] for TRISO particle fuel performance analysis, the available data is still limited. Different methods and models are used in those tools, and it is recommended to develop a new combined software using all the best adopted available methods and models.

2.2.4. Summary

Although the results of past studies have shown reliable and robust performance of TRISO fuel (low fission product release from the fuel particles during operating conditions), the fuel performance database continues to expand through several ongoing R&D and qualification programs. The main efforts are focused on investigation of the performance margin of the fuel, and the lack of data (therefore models/predicting tools) beyond operational conditions should be compensated. The summary of the paper can be listed as follows:

1. The consideration of fission gases and volatile FPs (besides Xe, Kr, Co, and CO_2) in pressure calculations of buffer layer is recommended to enhance the accuracy of the modelling tools.
2. Although the anisotropy effects in graphite material play a significant role in fuel performance analysis, the usage of new developed artificial graphite seems to solve this problem.
3. Although developed models and methods are able to predict accurate results in temperature distribution analysis, the uncertainty analysis (for thermal conductivity coefficient) are recommended.
4. Kernel migration itself has no direct impact on the fuel performance, but it influences on many other important phenomena. The sensitivity and uncertainty analysis are recommended to analyse the real impact of kernel migration on fuel performance analysis.
5. Many available models/tools exist to calculate FP release from the fuel, however, additional research is needed to get the clear picture of this phenomenon (the main problem is related with the lack of experimental data for several gases and metals).
6. Chemical phenomena occurring in TRISO fuel has a significant role for fuel performance analysis. For better understanding its impact and for improvements modelling tools, it is recommended to consider also existing chemical elements with low concentrations.
7. For mechanical performance analysis many codes/tools are currently available using different methods/models. Development of a new combined code is recommended which will include all the best-adapted available methods.

3. Pressure Buildup analysis of TRISO fuel particles

As mentioned earlier, TRISO particles represent the most common form of nuclear fuel for high-temperature gas-cooled reactors. As was mentioned in the previous Chapter, typically it consists of five regions: a fuel kernel (which contains the nuclear fuel), a porous carbon buffer, an inner pyrolytic carbon (IPyC) layer, a SiC layer (which acts as the main pressure vessel for the particle) and an outer pyrolytic carbon (OPyC) layer.

Because of its design, TRISO particles are able to contain fission products even at high operating temperatures and high burnup. However, there are some limitations to the temperature/burnup levels, which are related to the mechanical integrity of the particle. There are several phenomena influencing the mechanical failure of TRISO particles, such as pressure buildup, kernel migration, chemical attack, IPyC layer debonding [123]. Accurate evaluation of pressure buildup inside TRISO particles is particularly important because it is acting as a driving force for all the above-mentioned phenomena. Therefore, even small changes in pressure values can have a significant influence on mechanical integrity of TRISO particle.

The pressure buildup inside TRISO particles is a result of three main contributors: gases produced during the fission (mainly noble gases), gases formed during oxygen interaction with a carbon layer (CO, CO_2), and ternary fission (mainly helium). In current performance models, it is assumed that the contribution of helium gas is negligible and is not considered in fuel performance analysis [40]. However, in case of high burnup operation, the accumulation of helium gas could be essential. On the other hand, the fission gases are diffusing from the fuel kernel and accumulating in the buffer layer, and from this perspective light gases (such as helium) are more diffusive than heavier gases. Therefore, we decided to also include helium gas in our analysis. The issue is more practical for UCO type fuel kernels, where the amount of released free oxygen is very low.

In this paper we analysed pressure buildup inside TRISO fuel particles for both UCO and UO_2 type kernels for different burnup levels. To assess the concentrations of fission gases and helium inside the fuel kernel, the NGNP design-based fuel block element was selected [124]. For burnup calculations the Serpent code was used [125]. The molecular gases for UCO type kernel were not considered, as it has been proven that unlike UO_2, carbon containing fuels do not produce excess free oxygen [116]. For UO_2 type kernels, it was assumed that all free oxygen in the system is transferred into CO molecules. In reality, some oxygen molecules will also make CO_2 gas, but its concentration is very small [51]. For calculating the free oxygen released in the system both Proksch [39] and Homan [126] approximations were used.

To quantify the pressure in the buffer layer of TRISO particles, the ideal gas law and the Redlich-Kwong equations of state were implemented. In current TRISO performance models both equations are widely used [122], and the secondary aim of this work was to quantify the difference between those two models. Then, the maximal tensile stress for the SiC layer of the TRISO particle was calculated and finally, the failure fraction of the SiC layer was estimated using Weibull distribution.

3.1 Model Description

The concentrations of fission products in nuclear fuel are dependent on many factors such as operating condition, burnup level, neutron spectrum, initial enrichment of the fuel, etc. However, the main two factors are the burnup level and neutron spectrum in the fuel block. The aim of this paper is to assess pressure buildup for the representative TRISO particles. Therefore, the analysis was done using an infinite fuel block model based on NGNP design parameters for GT-MTR reactor [124].

The originally designed fuel compact consists of 14% enriched UCO type fissile particles with 30% packing fraction. The coolant and fuel temperatures in the core are 950 ^{0}C and 1200 ^{0}C, respectively. Key geometric design parameters are presented in Tables 3.1-3.2. Table 1 represents the TRISO fuel particle data, while Table 2 describes the geometry of fuel block elements.

Table 3.1: TRISO fuel particle design data [124]

Layer Material	Radius [cm]	Density [g/cm3]
UCO/UO_2	0.2125	10.5
Buffer	0.100	1
IPyC	0.30	1.9
SiC	0.35	3.2
OPyC	0.40	1.9

Table 3.2 Fuel block element design data [124]

Element	Dimension/number
Hexagonal Prism (mm)	793 in length
	361 across flats of hexagon-including gap (1 mm)
Coolant holes per element, small/large	6 / 102

Coolant hole diameter (mm)	15.88 for larger holes / 12.7 for the 6 smaller holes
Number of fuel rods in block	210
Pitch of coolant/fuel-hole array (mm)	18.8
Fuel hole diameter (mm)	12.7
Fuel hole length (mm)	752.6
Fuel compacts per fuel hole	15

Burnup calculations are performed with three-dimensional (3D) continuous energy Monte Carlo burnup code Serpent, for 150 MWd/kgU maximum burnup level. The calculations were performed with 5000 neutrons per cycle and with 200 active neutron cycles. All the fission gases, actinides, and helium isotopes were tracked during the burnup calculations. In addition, TRISO particle was handled as a separate depletion zone in burnup calculations, which enabled to get more accurate neutron flux. Based on this model, the UO_2 fuel kernel was also modelled in order to have a comparison between different types of fuel kernels.

The buildup of fission products was calculated for the full power steady-state core case. The axial and radial geometry of the fuel compact and fuel block are presented in Figure 3.1 and Figure 3.2 correspondingly.

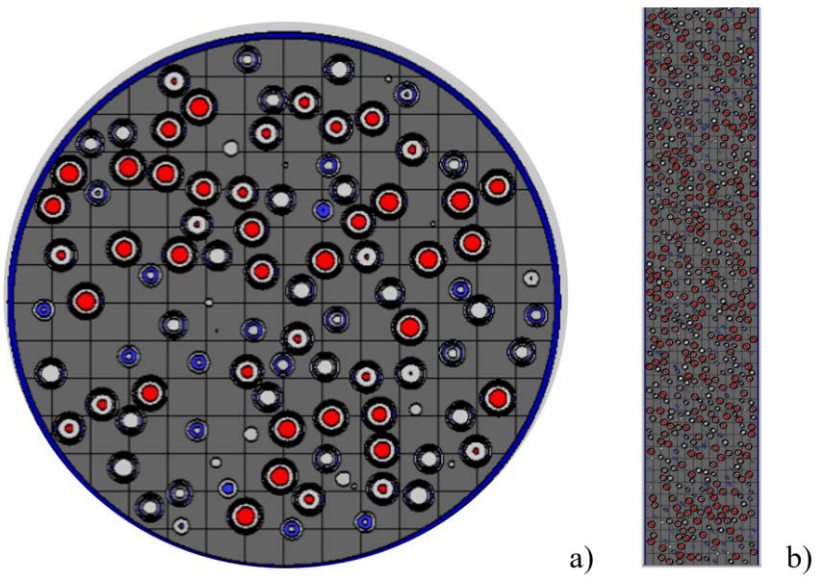

Figure 3.1 Radial (a) and axial (b) cross sections of the fuel compact model

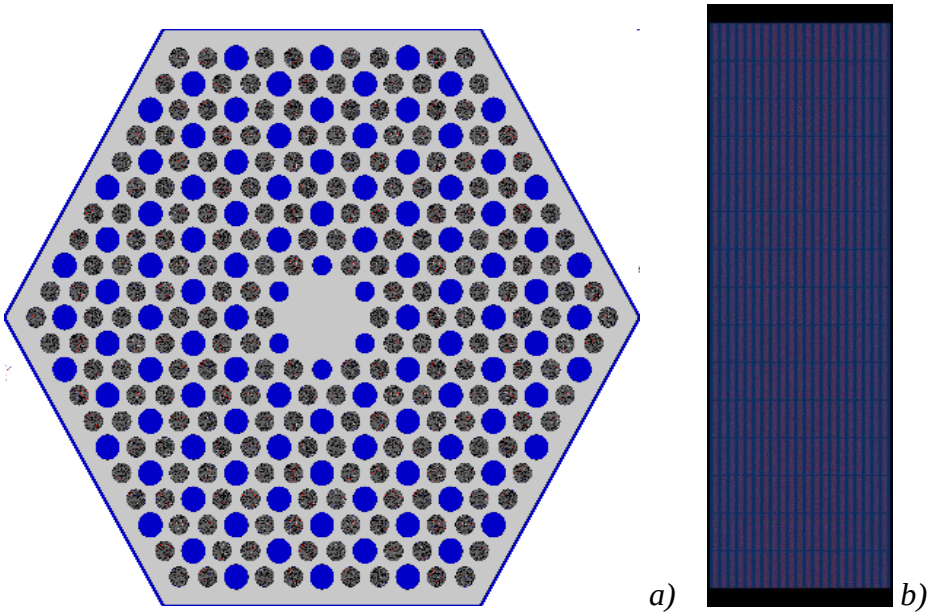

Figure 3.2 Radial (a) and axial (b) cross sections of the fuel block model

3.2 Fission and Molecular Gas Calculations

The calculation of fission gas concentrations is performed for 2 types of kernels keeping all other modelling parameters unchanged. This enabled us to assess what is the impact of the kernel type in the pressure buildup analysis. Figure 3.3 shows the neutron multiplication factor of the model dependent on burnup level, for both UCO and UO_2 type kernels. As we can see, there is almost no difference. The reason is that in terms of neutron spectrum, both carbon and oxygen atoms are behaving similar. Which means that replacing some amount of carbon atoms with oxygen atoms in the fuel kernel, the corresponding change in neutron spectrum is very small. The uncertainty value in the neutron multiplication factor calculations was less than 10^{-4}.

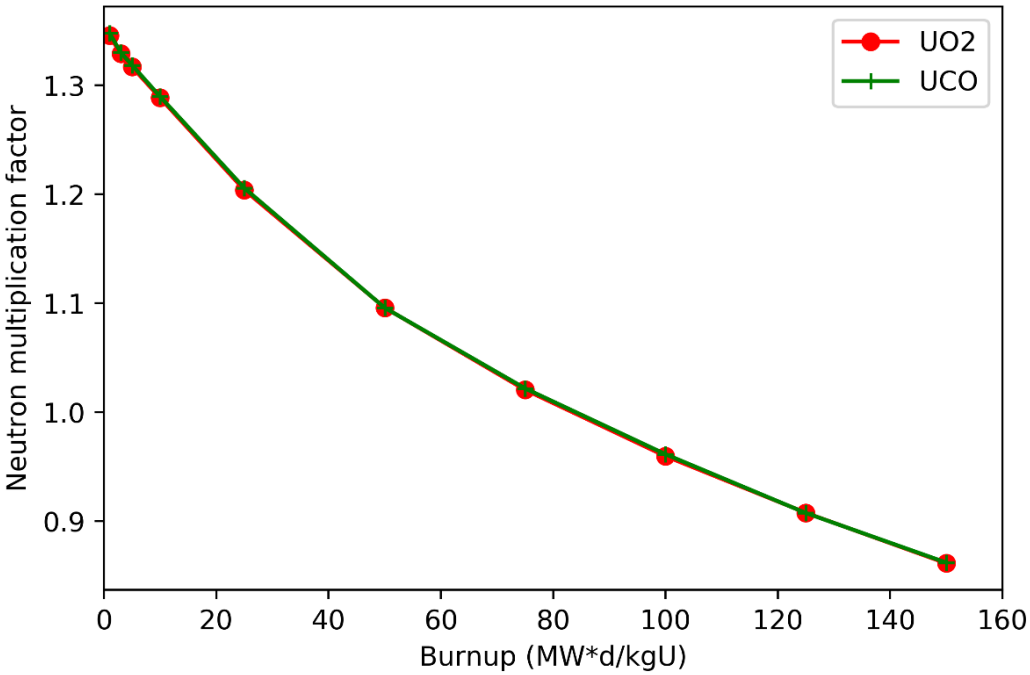

Figure 3.3 Neutron multiplication factor dependence on burnup for UCO and UO_2 fuel kernels.

3.2.1 Concentration of fission gases and helium

For estimating pressure buildup inside TRISO particles Xe, Kr and He gases were considered in this paper. The aim of helium consideration was to assess how its concentration is changing in high burnup values and what is the potential contribution of helium in total pressure value. Also, it was interesting to see if there is any essential dependence on fuel kernel type. In Figure 3.4 the concentrations of targeted gases are illustrated (dependent on burnup) for UCO type fuel, and in Figure 3.5 the results for UO_2 type kernel are shown. From Figure 3.4 and Figure 3.5 we can see that the concentration of Xe is the highest in both cases, and the difference between Xe, Kr and He is in few orders. We can see also that the concentration of helium is increasing faster during the burnup, in comparison with Xe and Kr.

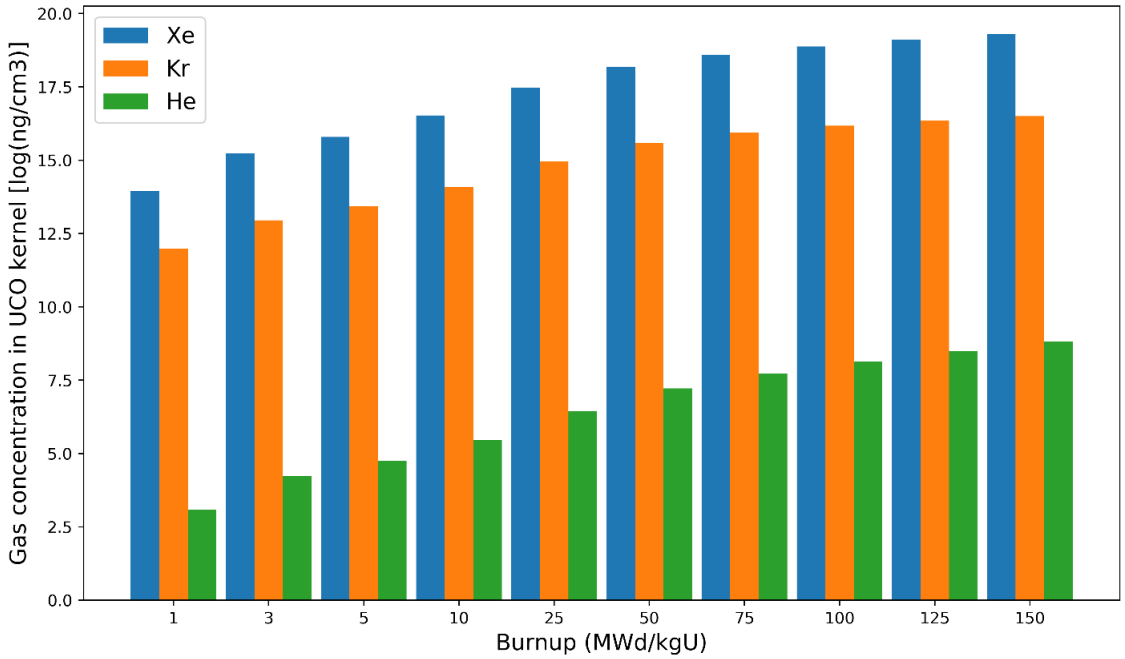

Figure 3.4 Concentrations of targeted gases in UCO type fuel kernel for different burnup values.

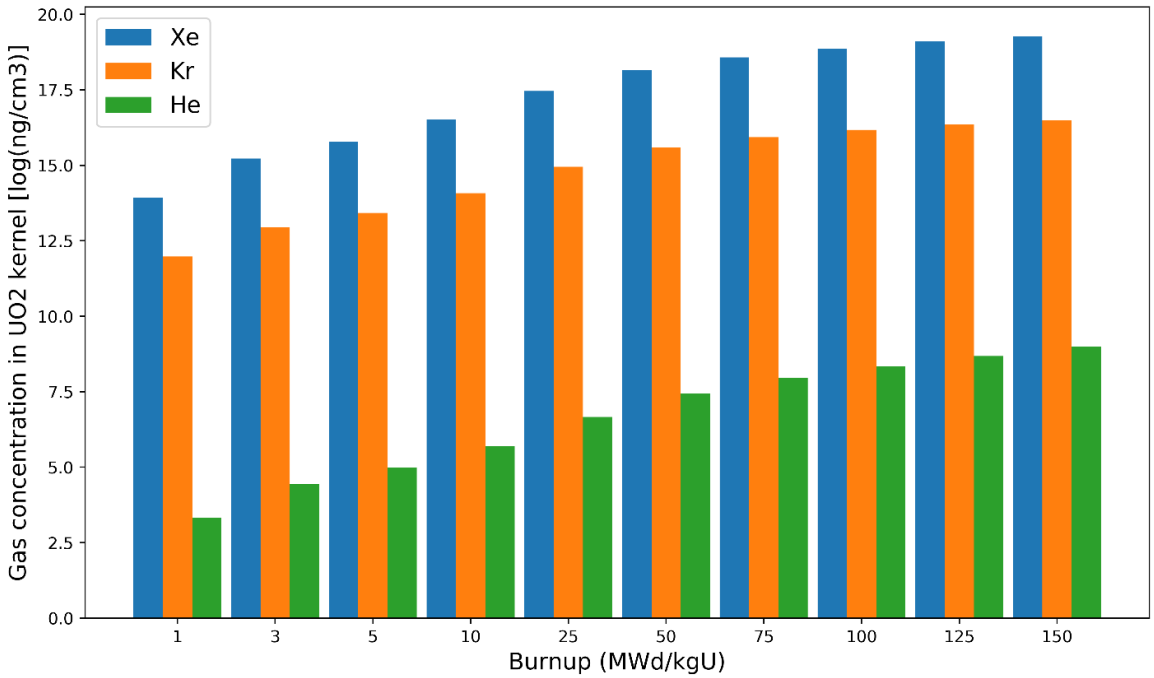

Figure 3.5: Concentrations of targeted gases in UO_2 type fuel kernel for different burnup values.

Figure 3.6 shows the relative difference of targeted gas concentrations for UO_2 and UCO type kernels. As we can see, there is no practical difference in case of Xe and Kr gases, while the concentration of helium is much higher in UO_2 type kernelled particles.

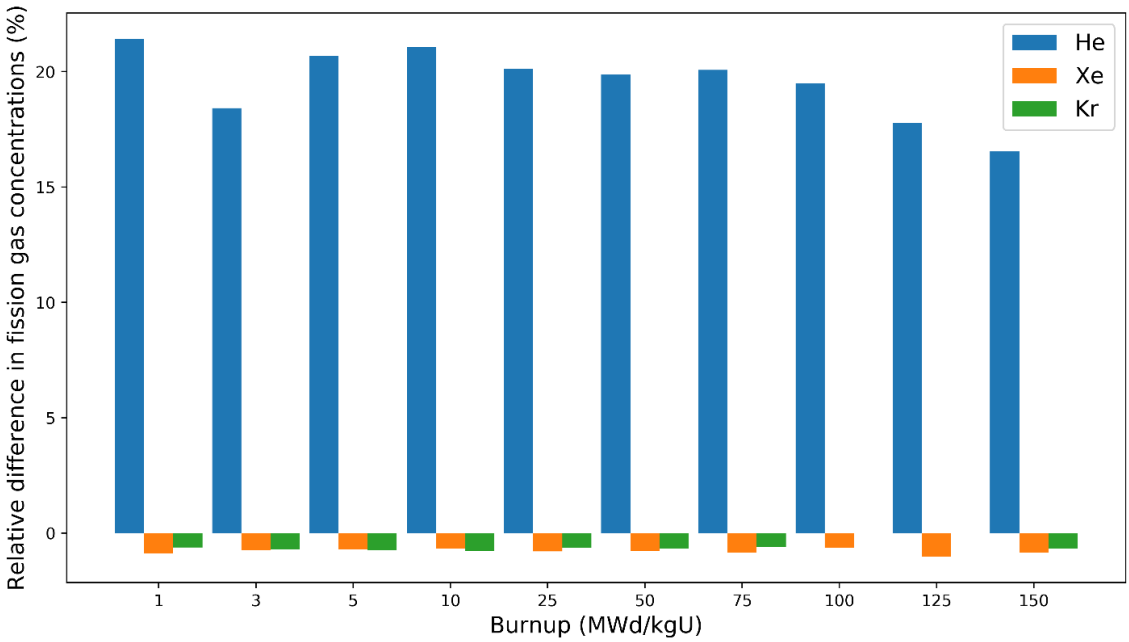

Figure 3.6: Relative difference of targeted gases for UO_2 and UCO type fuel kernels.

3.2.2 Concentration of molecular gases

As it was mentioned before, in this study we considered only CO molecular gas, as the formation of CO_2 gas is very limited. In other words, we assumed that all free oxygen released in the system is converted into CO molecules. In order to calculate the free oxygen release, both Proksch and Homan approximations were used. In case of Proksch model, the released free oxygen per fission in calculated by the following formula:

$$OpF = \mathrm{t}^2 \cdot 10^{(-0.21\ -8500/\mathrm{T})} \tag{3.1},$$

and in the case of Homan model, the equation looks like this:

$$OpF = 1.641 \cdot e^{(-3311/\mathrm{T})} \tag{3.2},$$

where OpF is the ratio of released oxygen atoms per fission, t is corresponding to the time (days the fuel was burned) and T is the fuel temperature (K).

In order to calculate the total number of fissions in TRISO fuel particle, the following equation was used:

$$N_{tf} = \frac{P_{fb} \cdot L}{N_{tr} \cdot E_f} \tag{3.3},$$

where P_{fb} is the power of fuel block, N_{tr} is the total number of TRISO particles inside fuel block, L is the operational time (in seconds), and E_f is the energy released per fission (200 MeV).

The number of formatted CO atoms inside TRISO fuel then will be equal to: $N_{co} = N_{tf} \cdot OpF$, and the corresponding mass inside the fuel kernel will be:

$$m(CO) = N_{co} \cdot M_{co}/Na \quad (3.4),$$

where Na is the Avogadro constant, M_{co} is the molar mass of CO.

Figure 3.6 shows the concentration change of CO gas (ng/cm^3) dependent on burnup (in logarithmic scale) calculated by Homan and Proksch models. As we can see, there is a difference in these models (especially in low operational time and burnup values), and from the safety perspectives the Homan model is more recommendable. Comparing with other gases in UO_2 kernel (see Figure 3.7) we can see that in the case of Proksch model, the concentration of CO gas is becoming equal to Kr at 50 MWd/kgU point, while in case of Homan model it has almost the same value at every burnup level.

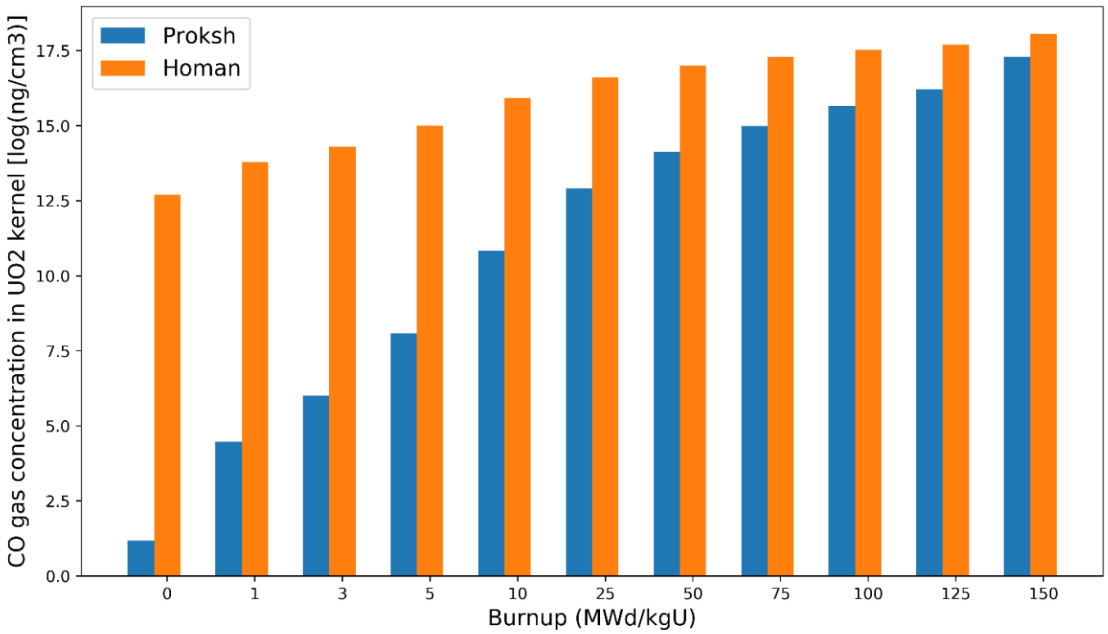

Figure 3.7: The concentration of CO gas calculated by Proksch and Homan models.

It is also important to mention, that those values are overestimated, as we converted all the available free oxygen into CO atoms, while in reality some amount of free oxygen will be taken

to form other molecules (especially in high burnup values, where the concentration of fission products are relatively high).

3.3 Pressure Buildup Modelling and Results

Pressure calculations were performed using both ideal gas law and the Redlich-Kwong equation of state. Both models are widely used in fuel performance tools, although Redlich-Kwong equation is assumed to be more adapted. The Redlich-Kwong equation has the following form:

$$P = \frac{R \cdot T}{V_m - b} - \frac{a}{\sqrt{T} \cdot V_m \cdot (V_m + b)} \quad (3.5),$$

where P is the gas pressure, R is the gas constant, T is the gas temperature, V_m is the gas molar volume, a is a constant that corrects for the attractive potential of molecules, b is a constant that corrects for volume.

Figure 3.8 and Figure 3.9 represent the results of pressure values in buffer layer of TRISO fuel with UCO and UO_2 (using Homan model for CO gas production) type kernels correspondingly, calculated by Redlich-Kwong equation.

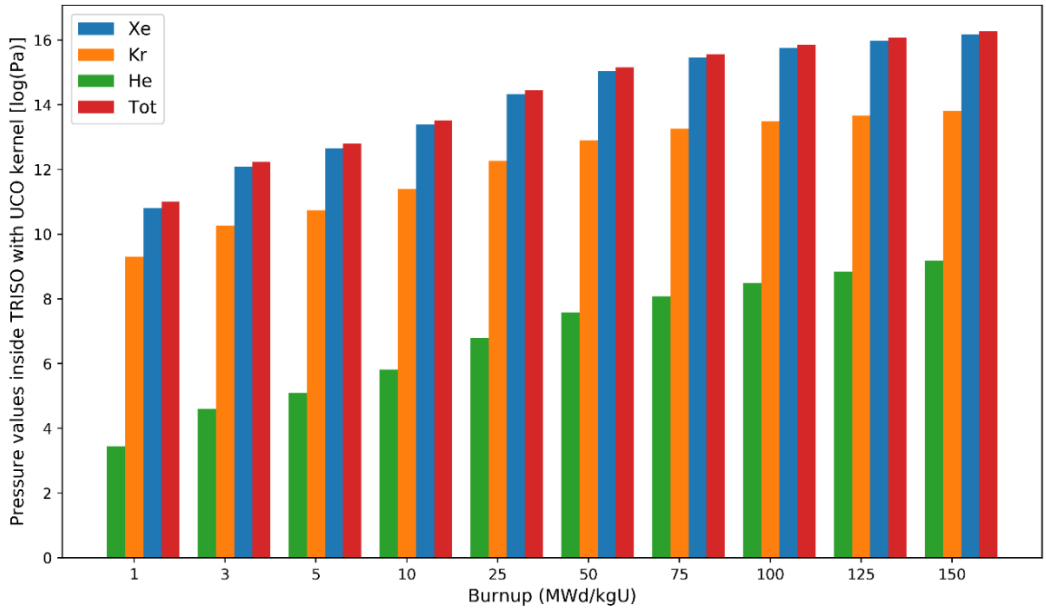

Figure 3.8: Pressure values inside the buffer layer of TRISO particle with UCO type kernel calculated by Redlich-Kwong equation.

From Figure 3.8 and Figure 3.9 we can see that the total pressure inside TRISO fuel is mainly created due to Xe gas both with UCO and UO_2 type kernels and is not much dependent

from the kernel type. In Figure 3.10 and Figure 3.11 the contribution of targeted gases in total pressure is shown in percentages. Figure 3.10 presents that the contribution of Kr gas is decreasing during the burnup increase, both in case of UCO and UO_2 kernels. Xe gas is making more than 80% of the total pressure. Kr gas contribution is around 18% in case of using Homan model and is around 10% for the Proksch model.

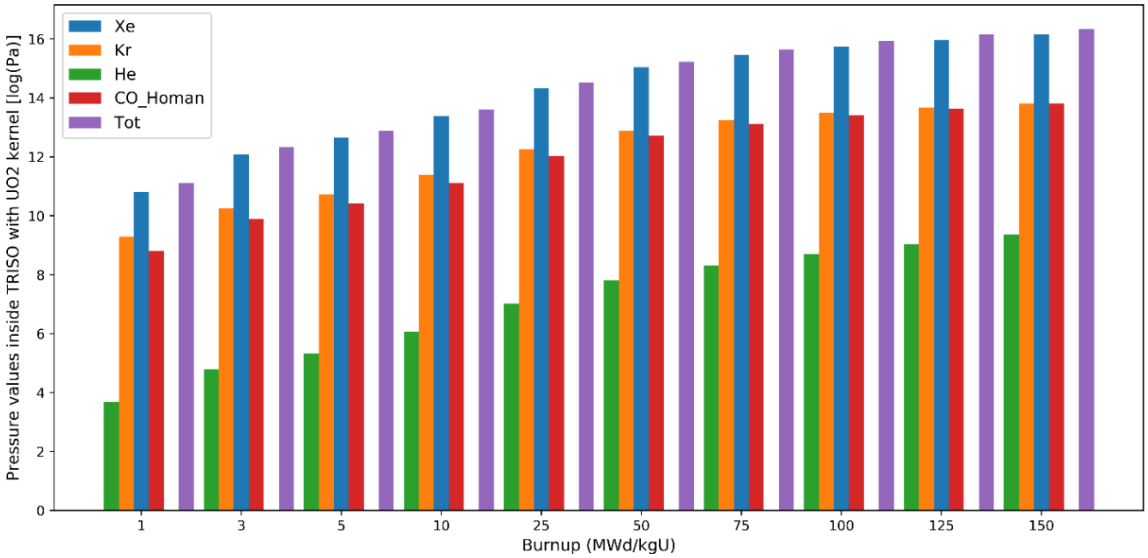

Figure 3.9: Pressure values inside the buffer layer of TRISO particle with UCO type kernel calculated by Redlich - Kwong equation.

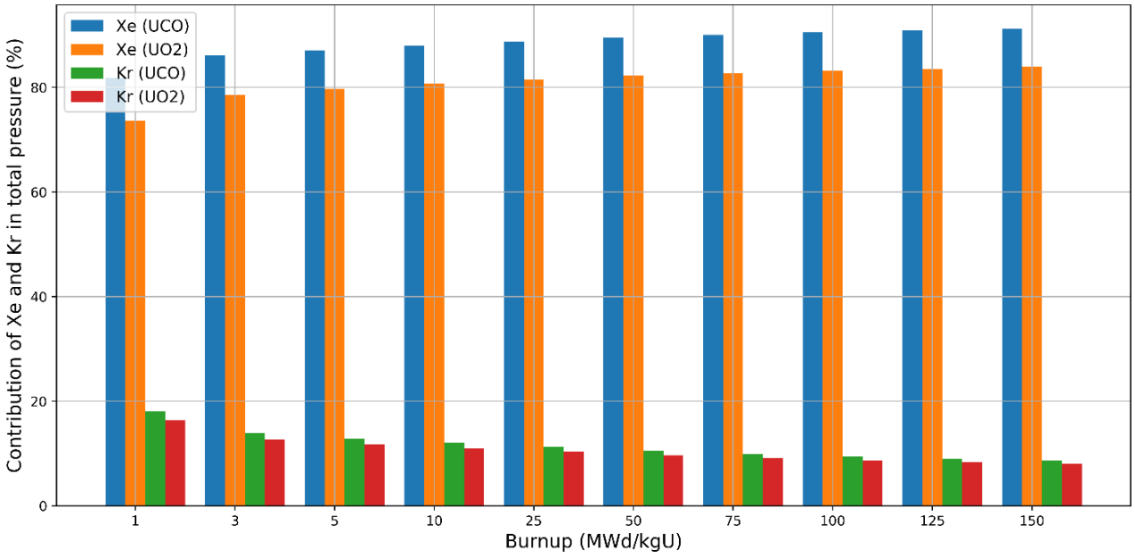

Figure 3.10: Contribution of Xe and Kr gases in total pressure.

From Figure 3.11 we can see that the contribution of CO gas is increasing with burnup (in case of Proksch model), however its contribution even at high burnup values is still less than

2%. In case of Homan model, CO contribution is quite high (around 10%). Also, we can see that the helium contribution in case of UO_2 fuel is a little higher, even when there is an additional pressure made by CO gas. However, it is making very negligible impact on the total pressure even in high burnup values and in case of max burnup it is less than 0.2%.

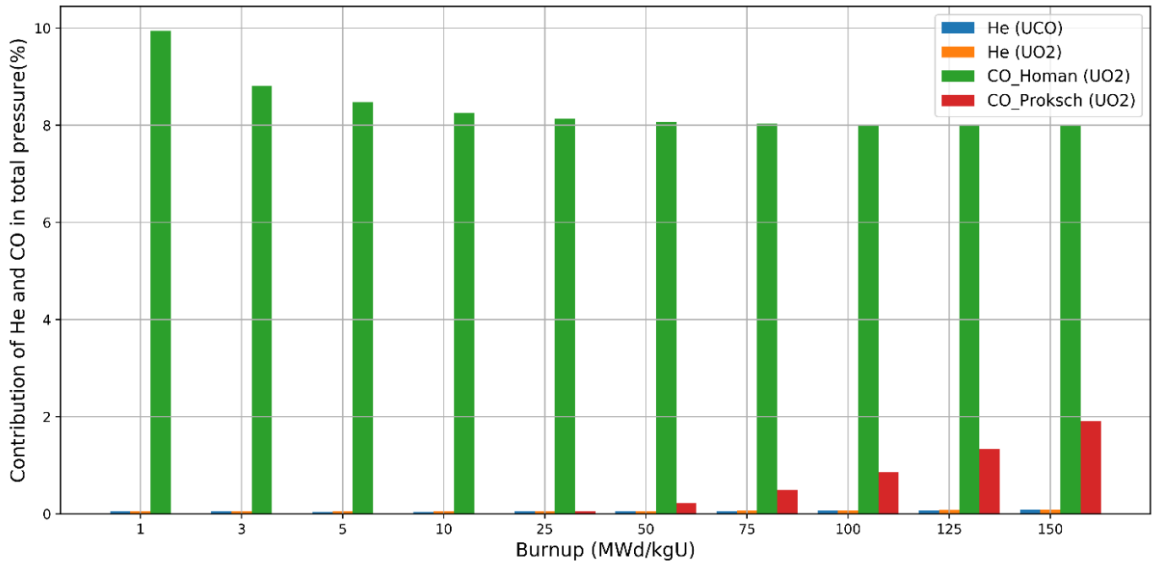

Figure 3.11: Contribution of He and CO gases in total pressure.

Above analysis for pressure values were performed also with using ideal gas low, and for all the cases the Redlich-Kwong equation was more conservative. The difference between pressure values is mainly dependent on gas concentration, and the highest difference was for Xe gas. In Figure 3.12 the relative difference of pressure values is shown calculated by ideal gas law and Redlich-Kwong equations for Xe gas. As we can see, the difference is increasing by increasing burnup, and the max difference was around 1.8%.

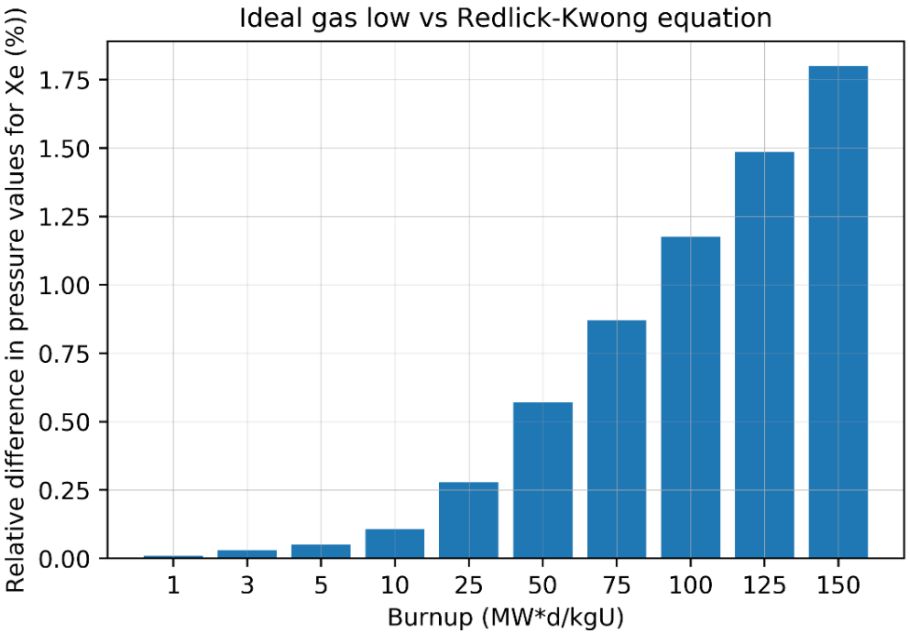

Figure 3.12: Relative difference in pressures values for Xe

3.4 Assessment of the Maximal Stress and Fuel Failure Rate

The main criterion of TRISO particle integrity is the failure rate of SiC layer. When SiC layer is failed, the TRISO particle is also considered failed. There are several reasons of SiC failure, such as pressure buildup in TRISO, chemical interaction with fission gases diffused from fuel kernel, kernel migration, mechanical debonding and irradiation induced effects. All these effects are correlated, and in specific conditions they can cause SiC failure.

In order to estimate the impact of pressure buildup on fuel failure rate, the thin-shell approximation was used to calculate the maximum tensile stress on SiC layer. Stresses were calculated both for using Homan and Proksch models. Figure 14 shows the corresponding results.

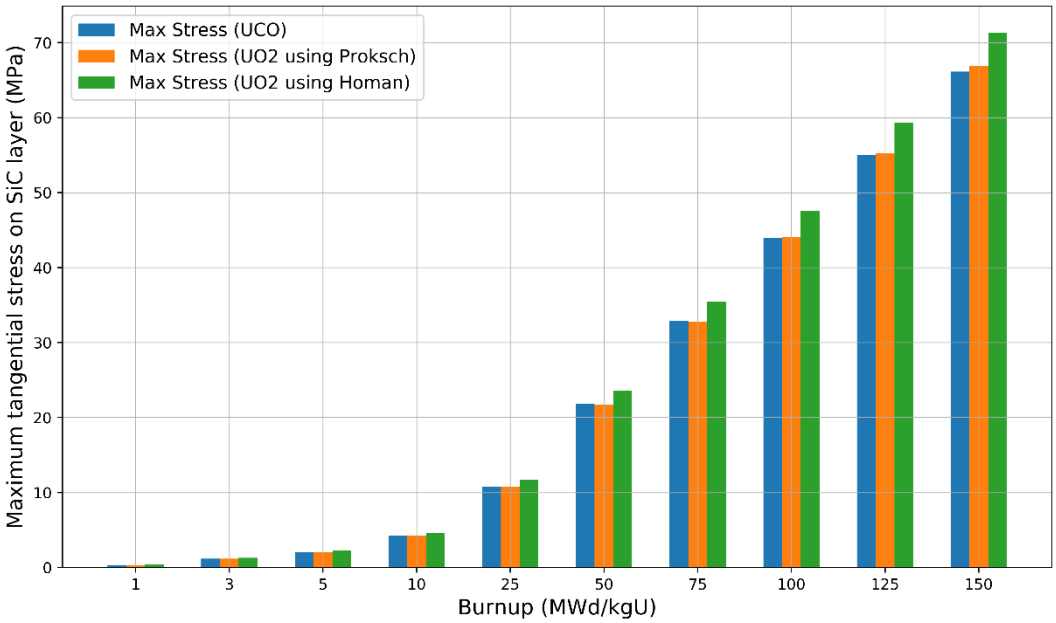

Figure 3.13: Max stress on SiC layer of TRISO particle both for UCO and UO_2 type kernels.

As we can see from Figure 3.13, max stress in case of UCO kernel is a little lower than in UO_2, because of the CO gases, however the difference is not so very big even at high burnup values (around 5 MPa in case of Homan model, and around 1 MPa in case of Proksch model).

Pressure vessel failure occurs when the tensile stress exceeds the ultimate tensile strength of the SiC layer. It was reported that for SiC layer the ultimate tensile strength is between 300-800 MPa [105].

In order to estimate the fuel failure fraction, the Weibull equation was used [117]:

$$FR = 1 - \exp\left(-\ln(2) \cdot \left(\frac{\sigma_t}{\sigma_a}\right)^m\right) \quad (3.6),$$

where FR is the failure fraction of SiC layer, σ_t is max tensile stress, $\sigma_u = 750MPa$ is the mean fracture strength, and m=6.84 is Weibull modulus [116]. The results of fuel failure rate for both UCO and UO_2 kernels are shown in Figure 3.14.

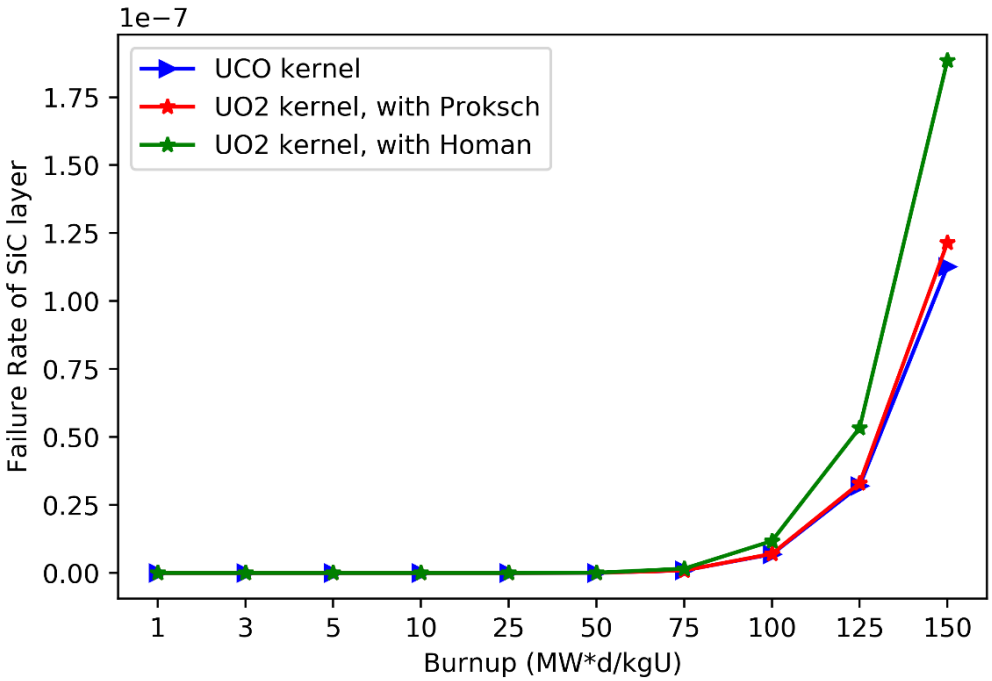

Figure 3.14: TRISO fuel failure rate both for UCO and UO_2 type kernels.

From Figure 3.14 we can see that the TRISO particle failure rate is below 2×10^{-7} value even in high burnup values. The current TRISO fuel failure acceptance criteria is around 10^{-5}. Also, we can see that in the case of Proksch model the failure rate of SiC layer with UO_2 type kernel is almost equal to the case with UCO kernel type, however the usage of Homan model provides more conservative results.

3.5 Summary

Single fuel block element of GT-MTR reactor (based on NGNP recommended design) was modelled to estimate the pressure buildup inside TRISO fuel particles using Serpent code. Analysis is done both for UCO and UO_2 type fuel kernels with the same modelling parameters. Besides Xe and Kr, He and CO gases (in case of UO_2 kernel) were also considered and their contribution in total pressure was studied. Different models were used to calculate the pressure in buffer layer and the free oxygen released in the fuel, and the differences were analysed. The maximum stress in SiC layer was calculated using thin shell approximation, and then Weibull equation was implemented to estimate fuel failure rate. The results obtained in this work can be summarized as follows:

- The main contribution in pressure buildup analysis is made by Xe gas (more than 80%) both for UCO and UO_2 type fuel kernels. Kr gas is making around 18% contribution in

total pressure in case of UCO fuel, and 10% in case of UO_2 type kernel (in case of using Homan model for calculating free oxygen release).

- Contribution of helium gas in total pressure for UO_2 type kernel is higher than for UCO type fuel, however the values are very small even at high burnup values (less than 0.1% for both kernel types).
- The ideal gas law and Redlich-Kwong equation of state are providing very similar results in low burnup values, however the second one is more conservative (1.8% difference in case of Xe gas, at high burnup values). In case of high burnup values the implementation of the appropriate model could be important, therefore in case of safety analysis it is recommended to use Redlich-Kwong equation.
- Fuel failure rate (with consideration of only pressure buildup inside TRISO fuel) in case of UO_2 kernel is higher than for UCO type kernel, however even at the highest burnup values the probability of fuel failure is almost 2 orders less than acceptance criteria.
- Future analyses are needed for understanding the correlation between pressure buildup and other phenomena in TRISO fuel particle performance analysis.

4. Uncertainty quantification of TRISO fuel performance analysis

As mentioned in Chapter 2, there are several phenomena influencing the mechanical failure and of TRISO particles, such as pressure buildup, kernel migration, chemical attack on SiC layer, IPyC layer deboning [123], etc. Therefore, an accurate evaluation of stresses in SiC layer of TRISO particles is particularly important to specify the safety limits and one should evaluate uncertainties. In general, the overall uncertainty quantification should include uncertainties of used tools, models, geometrical and material specifications, etc.

There are several publications which are addressing the impact of uncertainties of geometrical and material data on failure fraction of TRISO particles [127-128]. In current research, the geometrical and material related uncertainties from the optimization perspectives are evaluated. Which means, that we quantify the uncertainties not only against the reference case, but we consider all the potential combinations of different input sets for the better design. Of course, for the general optimization analysis other factors also should be considered, such as fission gas release, chemical effects, neutronics, etc. However, considering the vast number of combinations, current results can serve as a reference for the overall TRISO fuel optimization analysis and new reactor designs [129-133]. As a reference case for the analysis, AGR-2 experimental data was used [134] with the UCO type kernel, as it has been proven that unlike UO_2, carbon containing fuels do not produce excess free oxygen [135] and therefore, those kernels are more likely to be used in the future designs.

4.1 Model description

In the current model, the AGR-2 (Advanced Gas Reactor 2) experimental data was used. AGR-2 is a research experiment that studied the behaviour of fuel rods made from a new type of nuclear fuel called "advanced fuel." The fuel is made from a mixture of cerium and uranium, which has the potential to increase the efficiency of nuclear power plants and reduce the amount of nuclear waste produced. The experiment was being conducted at the Idaho National Laboratory and involves running the fuel rods through a series of tests to determine their performance under different conditions.

The AGR-2 test train was a multi-capsule, instrumented lead experiment containing six separate capsules stacked vertically, each independently controlled for temperature and monitored for fission gas release.

Table 4.1: Irradiation conditions of AGR-2 compacts [134]

Compact	Fuel Type	Fluence (10^{25} n/m^2) [E>0.18 MeV]	Burnup (%FIMA)	Avg. Temp. (°C)	Compact	Fuel Type	Fluence (10^{25} n/m^2) [E>0.18 MeV]	Burnup (%FIMA)	Avg. Temp. (°C)
Capsule 2	UCO				Capsule 5				
2-1-1	UCO	3.21	12.55	1218	5.1.1	UCO	3.41	12.82	1108
2-1-2	UCO	3.25	12.64	1219	5.1.2	UCO	3.43	12.90	1109
2-1-3	UCO	2.88	10.96	1194	5.1.3	UCO	3.03	11.10	1078
2-2-1	UCO	3.35	12.49	1287	5.2.1	UCO	3.38	12.30	1141
2-2-2	UCO	3.39	12.57	1287	5.2.2	UCO	3.39	12.36	1141
2-2-3	UCO	2.99	10.82	1261	5.2.3	UCO	3.00	10.44	1108
2-3-1	UCO	3.42	12.65	1296	5.3.1	UCO	3.28	12.05	1126
2-3-2	UCO	3.46	12.07	1296	5.3.2	UCO	3.29	12.10	1126
2-3-3	UCO	3.06	11.02	1270	5.3.3	UCO	2.91	10.08	1093
2-4-1	UCO	3.44	13.14	1240	5.4.1	UCO	3.13	12.07	1071
2-4-2	UCO	3.47	13.17	1240	5.4.2	UCO	3.14	12.05	1071
2-4-3	UCO	3.08	11.53	1216	5.4.3	UCO	2.78	10.09	1040
Capsule 3					Capsule 6				
3-1-1	UO_2	3.41	10.62	1011	6-1-1	UCO	2.73	10.79	1100
3-1-2	UO_2	3.45	10.69	1012	6-1-2	UCO	2.73	10.83	1100
3-1-3	UO_2	3.05	9.27	996	6-1-3	UCO	2.42	9.10	1069
3-2-1	UO_2	3.47	10.45	1061	6-2-1	UCO	2.60	10.18	1129
3-2-2	UO_2	3.51	10.54	1062	6-2-2	UCO	2.61	10.20	1129
3-2-3	UO_2	3.09	9.03	1045	6-2-3	UCO	2.30	8.23	1095
3-3-1	UO_2	3.49	10.49	1062	6-3-1	UCO	2.42	9.60	1094
3-3-2	UO_2	3.53	10.56	1062	6-3-2	UCO	2.43	9.61	1094
3-3-3	UO_2	3.11	9.09	1046	6-3-3	UCO	2.14	7.47	1060

Compact	Fuel Type	Fluence (10^{25} n/m^2) [E>0.18 MeV]	Burnup (%FIMA)	Avg. Temp. (°C)	Compact	Fuel Type	Fluence (10^{25} n/m^2) [E>0.18 MeV]	Burnup (%FIMA)	Avg. Temp. (°C)
3-4-1	UO_2	3.47	10.65	1013	6-4-1	UCO	2.20	9.25	1018
3-4-2	UO_2	3.50	10.71	1013	6-4-2	UCO	2.21	9.27	1018
3-4-3	UO_2	3.10	9.33	998	6-4-3	UCO	1.94	7.27	987

Each capsule contained 12 fuel compacts and only one fuel type. UCO fuel was irradiated in Capsules 2, 5, and 6 (see Table 4.1). Capsule 5-1-2 was selected as a reference case in this research. The characteristics of the AGR-2 TRISO particles are shown in Table 4.2.

Table 4.2: Characteristics of AGR-2 TRISO fuel particles [134]

Property	Mean Value ± Standard Deviation	
	UCO	UO_2
Kernel diameter (µm)	426.7 ± 8.8	507.7 ± 11.9
Kernel density (Mg/m^3)	10.966 ± 0.033	10.858 ± 0.082
U-235 enrichment (wt %)	14.029 ± 0.026	9.600 ± 0.010
Carbon/uranium (atomic ratio)	0.392 ± 0.002	not applicable
Oxygen/uranium (atomic ratio)	1.428 ± 0.005	2.003 ± 0.005
Buffer thickness (µm)	98.9 ± 8.4	97.7 ± 9.9
Buffer density (Mg/m^3)	not measured	0.99
IPyC thickness (µm)	40.4 ± 2.5	41.9 ± 3.2
IPyC density (Mg/m^3)	1.890 ± 0.011	not measured
SiC thickness (µm)	35.2 ± 1.2	37.5 ± 1.2
SiC density (Mg/m^3)	3.197 ± 0.004	3.200 ± 0.002
OPyC thickness (µm)	43.4 ± 2.9	45.6 ± 2.4
OPyC density (Mg/m^3)	1.907 ± 0.007	1.884 ± 0.004
Compact diameter (mm)	12.286 ± 0.005	12.269 ± 0.007

Property	Mean Value ± Standard Deviation	
	UCO	UO_2
Compact length (mm)	25.141 ± 0.017	25.134 ± 0.018
Compact matrix density (Mg/m^3)	1.589 ± 0.005	1.667 ± 0.006

For the uncertainty analysis, only the geometry and density of the layers were considered in current research. Taking into consideration the high computation numbers, only 4 cases for each parameter were chosen in their uncertainty range. The details are shown in Table 4.3. In total, 9.765.625 cases (5^{10}) were considered in this research.

Table 4.3: Chosen parameters for the uncertainty analysis

	X	REF	REF-X	REF+X	REF-2X	REF+2X
Parameter	uncertainty range (±)	case0	case1	case2	case3	case4
Kernel radius (mm)	4.4	**213.35**	208.95	217.75	204.55	222.15
Buffer Thickness (mm)	8.4	**98.9**	90.5	107.3	82.1	115.7
IPyC thickness (mm)	2.5	**40.4**	37.9	42.9	35.4	45.4
SiC thickness (mm)	1.2	**35.2**	34	36.4	32.8	37.6
OPyC thickness (mm)	2.9	**43.4**	40.5	46.3	37.6	49.2
Kernel density (g/cm^3)	0.033	**10.966**	10.933	10.999	10.9	11.032
Buffer density (g/cm^3)	0.01	**1.05**	1.04	1.06	1.03	1.07
IPyC density (g/cm^3)	0.011	**1.89**	1.879	1.901	1.868	1.912
SiC density (g/cm^3)	0.004	**3.197**	3.193	3.201	3.189	3.205
OPyC density (g/cm^3)	0.007	**1.907**	1.9	1.914	1.893	1.921

The fuel performance analysis of the selected cases was performed using the Bison code [12]. Bison is a multi-physics, multi-dimensional, and multi-scale computer code that is used to model the behaviour of nuclear fuel rods. It uses finite element methods to model the behaviour of the fuel under different operating conditions, including thermal, mechanical, and chemical behaviour. In current research, 1D version of the model is selected.

The calculations were divided into five equal batches (i.e., groups) over the neutron irradiation time. The following objective parameters were selected for analysis:

- Gas pressure – gas pressure in the buffer

- Pd penetration – penetration depth of palladium into the SiC layer
- SiC radial stress– maximum radial stress on the SiC layer
- SiC tangential stress – tangential stress on the SiC layer
- IPyC Weibull failure fraction – failure fraction of the IPyC layer
- SiC Weibull failure fraction – failure fraction of the SiC layer.

The results of the reference case (see Table 4.3) are shown in the Table 4.4. The reference case represents the combination of the man value parameters shown in Table 4.2.

Table 4.4: Results of the reference case

Selected parameter	Min value	Max value
Gas pressure	833.35	4.15E+6
Pd penetration	1.12E-08	5.09E-06
Radial SiC stress	-2.5E+07	-3741415
Tangential SiC stress	-3.4E+08	-4.8E+07
IPyC Weibull failure fraction	9.24E-10	0.270195
SiC Weibull failure fraction	6.52E-14	1.44E-08

The numbers in the table above represent the minimum and maximum values of the objective parameters over the irradiation time. Our goal was to determine how the boundary values of the parameters of interest changed depending on the material and geometric properties of the TRISO fuel particles (from a safety and optimization perspective). Section 3 shows the uncertainty analysis results.

4.2 Results of Uncertainty Analysis

In this section, the results of uncertainty analysis and the corresponding summaries are shown from batch 1 to batch 5. The discussion of the results is presented in section 4.4.

4.2.1 Results of Uncertainty Analysis-batch 1

Below, the results of each objective parameter are presented for batch 1. The average, minimum, and maximum values for each parameter is presented, along with the corresponding input values. Results of gas pressure in the buffer layer are represented in Figure 4.1 and Table 4.5.

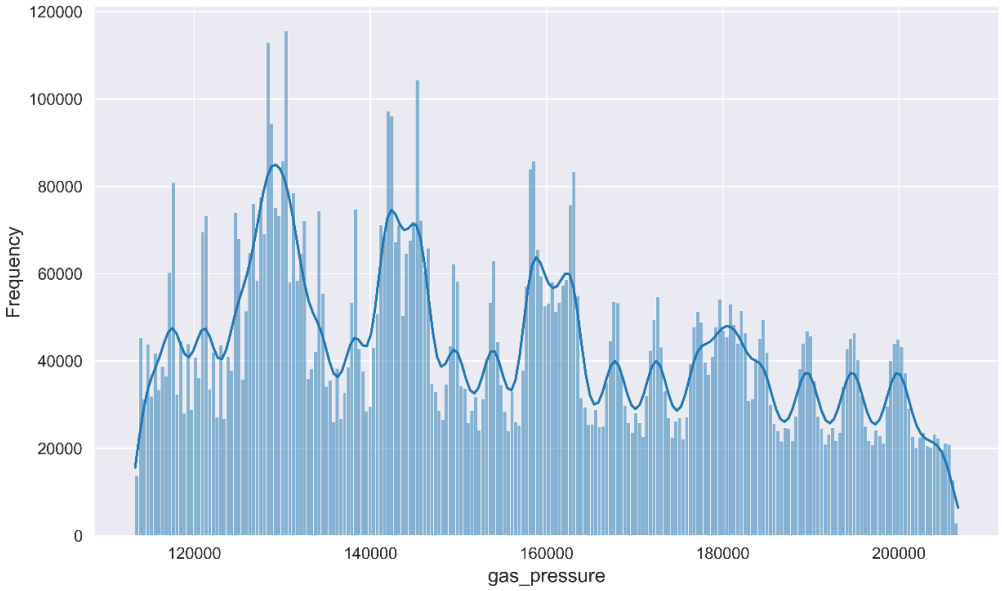

Figure 4.1: Distribution of gas pressure in buffer layer

Table 4.5: Pressure case description: batch 1

Parameter	Max case	Min case
Gas pressure (Pa)	2.07E+05	1.13E+05
Pd penetration (m)	6.70E-07	6.70E-07
SiC radial stress (Pa)	-2.4E+07	-1.7E+07
Maximum SiC radial stress (Pa)	-2.82E+06	-1.89E+06
Minimum SiC radial stress (Pa)	-2.9E+07	-2.1E+07
SiC tangential stress (Pa)	-2.9E+08	-2.8E+08
Maximum SiC tangential stress (Pa)	-3E+07	-2.8E+07
Minimum SiC tangential stress (Pa)	-3.5E+08	-3.3E+08
IPyC Weibull failure fraction	0.1553	0.4237
SiC Weibull failure fraction	4.92E-09	3.64E-08

Parameter	Max case	Min case
Kernel radius (cm)	0.0222	0.0205
Buffer thickness (cm)	8.21E-03	0.0116
IPyC thickness (cm)	3.54E-03	4.54E-03
SiC thickness (cm)	3.28E-03	3.76E-03
OPyC thickness (cm)	4.92E-03	3.76E-03
Kernel density (g/cm^3)	10.900	11.032
Buffer density (g/cm^3)	1.070	1.030
IPyC density (g/cm^3)	1.912	1.868
SiC density (g/cm^3)	3.189	3.205
OPyC density (g/cm^3)	1.893	1.921

The average pressure of this case was 1.55E+5 Pa.

The results of palladium penetration into SiC layer are represented in Figure 4.2 and Table 4.6.

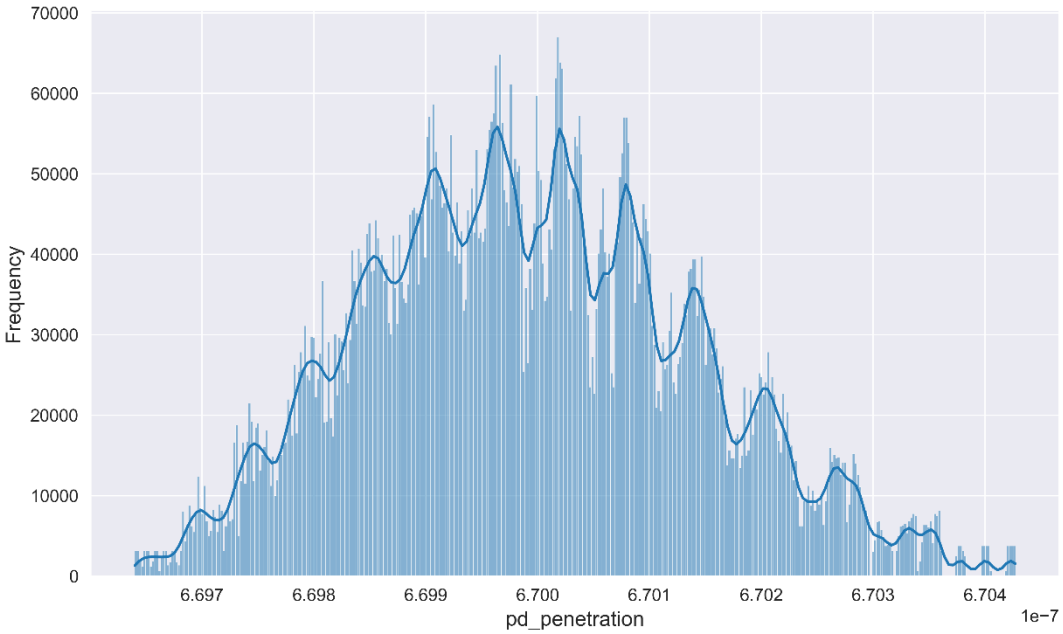

Figure 4.2: Distribution of Pd penetration into SiC layer

Table 4.6: Pd penetration description (batch 1)

Parameter	Max case	Min case
Gas pressure (Pa)	2.00E+05	1.17E+05
Pd penetration (m)	6.704E-07	6.69E-07
SiC radial stress (Pa)	-2.32E+07	-1.78E+07
Maximum SiC radial stress (Pa)	-2.58E+06	-2.08E+06
Minimum SiC radial stress (Pa)	-2.83E+07	-2.16E+07
SiC tangential stress (Pa)	-2.62E+08	-3.12E+08
Maximum SiC tangential stress (Pa)	-2.71E+07	-2.94E+07
Minimum SiC tangential stress (Pa)	-3.15E+08	-3.74E+08
IPyC Weibull failure fraction	0.2178	0.3099
SiC Weibull failure fraction	7.05E-09	2.52E-08
Kernel radius (cm)	0.022215	0.020455
Buffer thickness (cm)	8.21E-03	0.01157
IPyC thickness (cm)	3.54E-03	4.54E-03
SiC thickness (cm)	3.76E-03	3.28E-03
OPyC thickness (cm)	4.92E-03	3.76E-03
Kernel density (g/cm^3)	11.032	10.900
Buffer density (g/cm^3)	1.030	1.070
IPyC density (g/cm^3)	1.868	1.912
SiC density (g/cm^3)	3.189	3.205
OPyC density (g/cm^3)	1.921	1.893

The average value of palladium penetration was 6.70E-07 m.

The results of radial stress on SiC layer are represented in Figure 4.3 and Table 4.7.

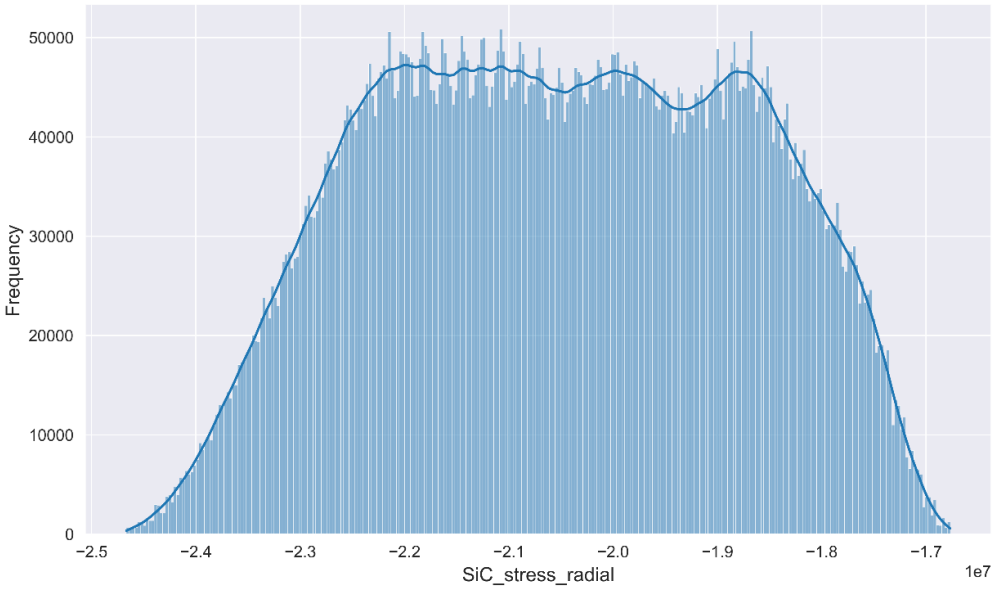

Figure 4.3: Distribution of radial stress on SiC layer

Table 4.7: Radial stress on SiC layer: case description (batch 1)

Parameter	Max case	Min case
Gas pressure (Pa)	1.28E+05	1.85E+05
Pd penetration (m)	6.70E-07	6.70E-07
SiC radial stress (Pa)	-1.7E+07	-2.5E+07
Maximum SiC radial stress (Pa)	-1.85E+06	-2.91E+06
Minimum SiC radial stress (Pa)	-2E+07	-3E+07
SiC tangential stress (Pa)	-2.7E+08	-3E+08
Maximum SiC tangential stress (Pa)	-2.5E+07	-3.2E+07
Minimum SiC tangential stress (Pa)	-3.3E+08	-3.6E+08
IPyC Weibull failure fraction	0.321279	0.210463
SiC Weibull failure fraction	2.33E-08	7.97E-09
Kernel radius (cm)	0.0222	0.0205
Buffer thickness (cm)	0.0116	8.21E-03

Parameter	Max case	Min case
IPyC thickness (cm)	4.54E-03	3.54E-03
SiC thickness (cm)	3.76E-03	3.28E-03
OPyC thickness (cm)	3.76E-03	4.92E-03
Kernel density (g/cm^3)	11.032	10.900
Buffer density (g/cm^3)	1.030	1.070
IPyC density (g/cm^3)	1.912	1.868
SiC density (g/cm^3)	3.189	3.201
OPyC density (g/cm^3)	1.921	1.893

The average value of radial SiC stress was -2.05E+07Pa.

The results of tangential stress on SiC layer are represented in Figure 4.4 and Table 4.8.

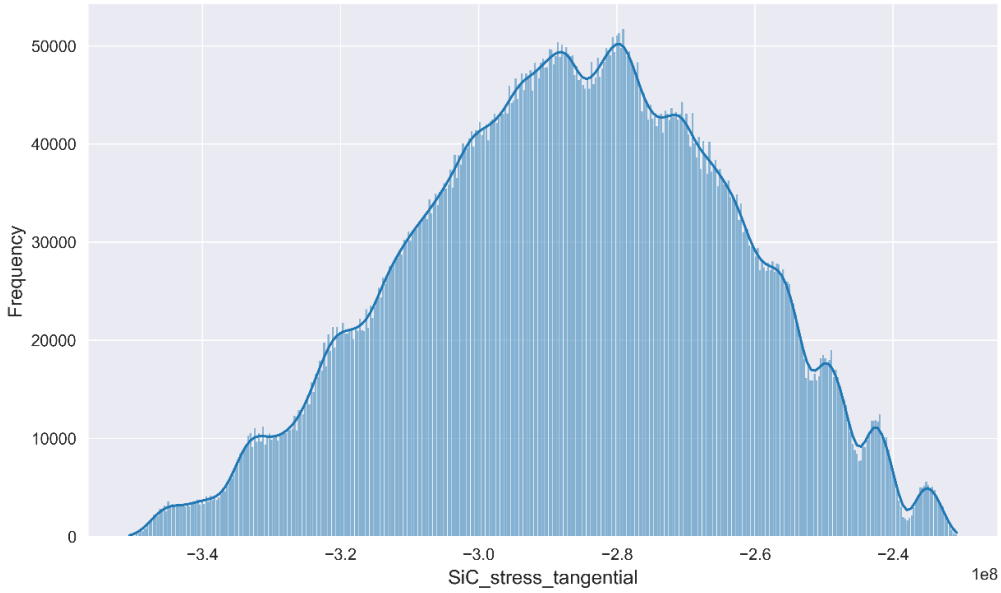

Figure 4.4: Distribution of tangential stress on SiC layer

Table 4.8: Tangential stress on SiC layer: case description (batch 1)

Parameter	Max case	Min case
Gas pressure (Pa)	1.33E+05	1.78E+05

Parameter	Max case	Min case
Pd penetration (m)	6.70E-07	6.70E-07
SiC radial stress (Pa)	-1.7E+07	-2.4E+07
Maximum SiC radial stress (Pa)	-1.93E+06	-2.77E+06
Minimum SiC radial stress (Pa)	-2.1E+07	-2.9E+07
SiC tangential stress (Pa)	-2.3E+08	-3.5E+08
Maximum SiC tangential stress (Pa)	-2.3E+07	-3.5E+07
Minimum SiC tangential stress (Pa)	-2.8E+08	-4.2E+08
IPyC Weibull failure fraction	0.1717	0.4124
SiC Weibull failure fraction	4.19E-09	4.61E-08
Kernel radius (cm)	0.0222	0.0205
Buffer thickness (cm)	0.0116	8.21E-03
IPyC thickness (cm)	3.54E-03	4.54E-03
SiC thickness (cm)	3.76E-03	3.28E-03
OPyC thickness (cm)	3.76E-03	4.92E-03
Kernel density (g/cm^3)	10.900	11.032
Buffer density (g/cm^3)	1.070	1.030
IPyC density (g/cm^3)	1.912	1.868
SiC density (g/cm^3)	3.197	3.197
OPyC density (g/cm^3)	1.921	1.893

The average value of SiC tangential stress was -2.9E+07 Pa.

The results of IPyC layer failure fraction are represented in Figure 4.5 and Table 4.9.

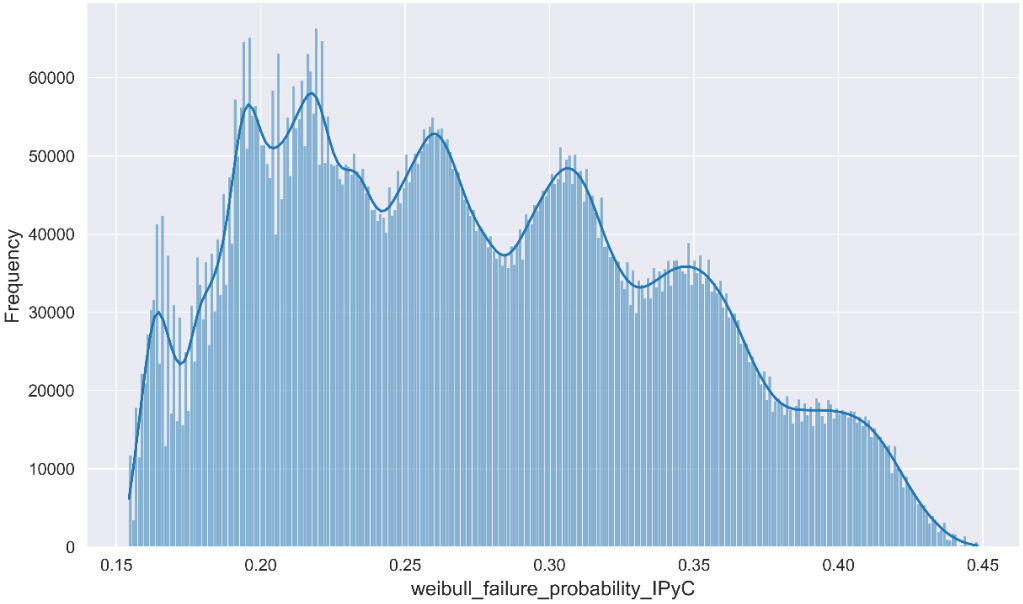

Figure 4.5: Distribution of failure fraction of IPyC layer

Table 4.9: IPyC layer failure fraction case description (batch 1)

Parameter	Max case	Min case
Gas pressure (Pa)	1.78E+05	1.64E+05
Pd penetration (m)	6.70E-07	6.70E-07
SiC radial stress (Pa)	-1.9E+07	-2.3E+07
Maximum SiC radial stress (Pa)	-2.24E+06	-2.48E+06
Minimum SiC radial stress (Pa)	-2.3E+07	-2.7E+07
SiC tangential stress (Pa)	-2.8E+08	-2.9E+08
Maximum SiC tangential stress (Pa)	-2.9E+07	-2.8E+07
Minimum SiC tangential stress (Pa)	-3.4E+08	-3.5E+08
IPyC Weibull failure fraction	0.4482	0.1544
SiC Weibull failure fraction	6.05E-08	3.90E-09
Kernel radius (cm)	0.0205	0.0222
Buffer thickness (cm)	8.21E-03	9.89E-03
IPyC thickness (cm)	4.54E-03	3.54E-03

Parameter	Max case	Min case
SiC thickness (cm)	3.76E-03	3.28E-03
OPyC thickness (cm)	3.76E-03	4.92E-03
Kernel density (g/cm^3)	11.032	10.900
Buffer density (g/cm^3)	1.030	1.070
IPyC density (g/cm^3)	1.868	1.912
SiC density (g/cm^3)	3.189	3.205
OPyC density (g/cm^3)	1.893	1.921

The average value of the IPyC Weibull failure fraction was 0.2741.

Results of SiC layer failure fraction are represented in Figure 4.6 and Table 4.10.

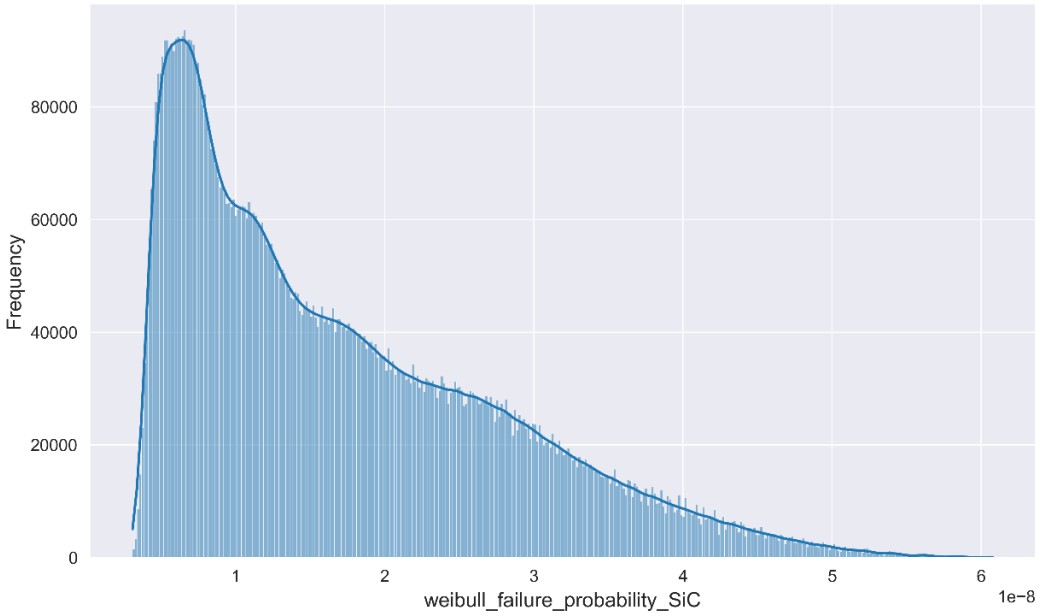

Figure 4.6: Distribution of failure fraction of SiC layer

Table 4.10: SiC layer failure fraction case description (batch 1)

Parameter	Max case	Min case
Gas pressure (Pa)	1.78E+05	1.33E+05

Parameter	Max case	Min case
Pd penetration (m)	6.70E-07	6.70E-07
SiC radial stress (Pa)	-1.9E+07	-2.2E+07
Maximum SiC radial stress (Pa)	-2.05E+06	-2.61E+06
Minimum SiC radial stress (Pa)	-2.3E+07	-2.7E+07
SiC tangential stress (Pa)	-2.8E+08	-2.9E+08
Maximum SiC tangential stress (Pa)	-2.8E+07	-3E+07
Minimum SiC tangential stress (Pa)	-3.4E+08	-3.5E+08
IPyC Weibull failure fraction	0.447499	0.155028
SiC Weibull failure fraction	6.08E-08	3.09E-09
Kernel radius (cm)	0.0205	0.0222
Buffer thickness (cm)	8.21E-03	0.000116
IPyC thickness (cm)	4.54E-03	3.54E-03
SiC thickness (cm)	3.76E-03	3.28E-03
OPyC thickness (cm)	3.76E-03	4.92E-03
Kernel density (g/cm^3)	11.032	10.900
Buffer density (g/cm^3)	1.030	1.070
IPyC density (g/cm^3)	1.868	1.912
SiC density (g/cm^3)	3.189	3.189
OPyC density (g/cm^3)	1.921	1.893

The average value of SiC Weibull failure fraction was 1.71E-08.

4.2.2 Results of Uncertainty Analysis-batch 2

Below are the objective parameter results for batch 2. The average, minimum, and maximum values for each parameter are presented, along with the corresponding input values.

The results for the gas pressure in the buffer layer are presented in Figure 4.7 and Table 4.11.

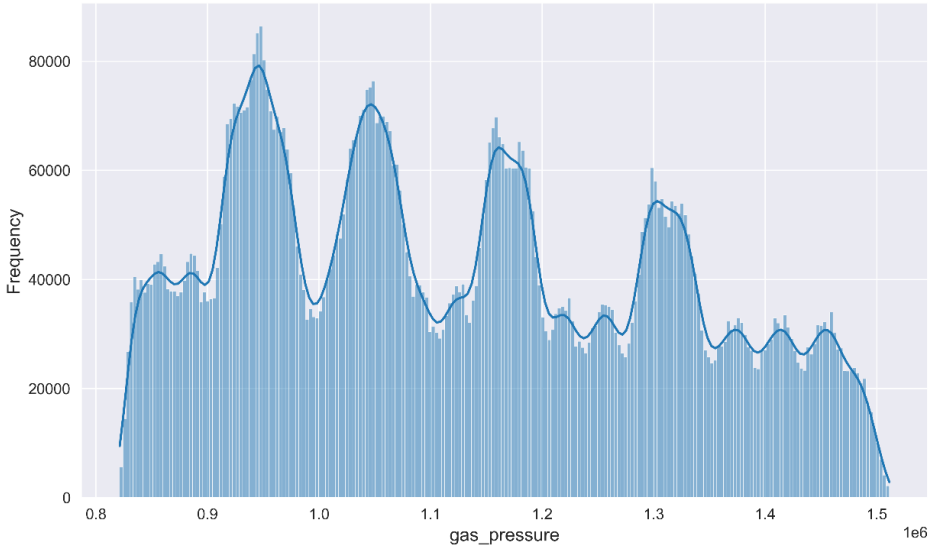

Figure 4.7: Distribution of gas pressure in buffer layer (batch 2)

Table 4.11: Pressure case description: batch 2

Parameter	Max case	Min case
Gas pressure (Pa)	1.51E+06	8.21E+05
Pd penetration (m)	1.62E-06	1.61E-06
SiC radial stress (Pa)	-2.1E+07	-1.5E+07
Maximum SiC radial stress (Pa)	-2.58E+06	-2.07E+06
Minimum SiC radial stress (Pa)	-2.8E+07	-2.2E+07
SiC tangential stress (Pa)	-2.5E+08	-2.3E+08
Maximum SiC tangential stress (Pa)	-2.8E+07	-2.9E+07
Minimum SiC tangential stress (Pa)	-3.5E+08	-3.4E+08
IPyC Weibull failure fraction	0.1548	0.4244
SiC Weibull failure fraction	4.96E-09	3.62E-08
Kernel radius (cm)	0.0222	0.0205
Buffer thickness (cm)	8.21E-03	0.0116

Parameter	Max case	Min case
IPyC thickness (cm)	3.54E-03	4.54E-03
SiC thickness (cm)	3.28E-03	3.76E-03
OPyC thickness (cm)	4.92E-03	3.76E-03
Kernel density (g/cm^3)	10.900	11.032
Buffer density (g/cm^3)	1.070	1.030
IPyC density (g/cm^3)	1.912	1.868
SiC density (g/cm^3)	3.197	3.205
OPyC density (g/cm^3)	1.921	1.893

The average pressure value was 1.13E+06 Pa.

The results of palladium penetration into SiC layer are represented in Figure 4.8 and Table 4.12.

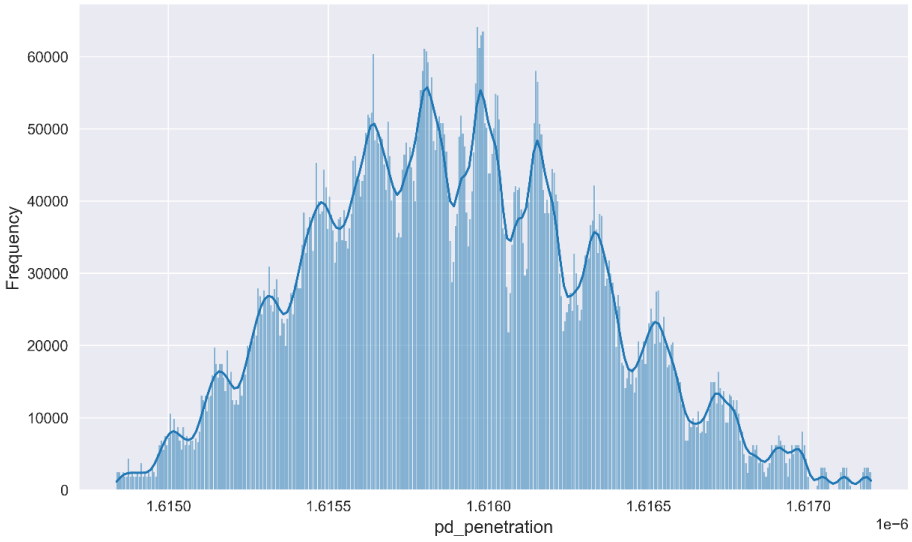

Figure 4.8: Distribution of Pd penetration into SiC layer

Table 4.12: Pd penetration description (batch 2)

Parameter	Max case	Min case
Gas pressure (Pa)	1.46E+06	8.53E+05
Pd penetration (m)	1.62E-06	1.61E-06

Parameter	Max case	Min case
SiC radial stress (Pa)	-2E+07	-1.5E+07
Maximum SiC radial stress (Pa)	-2.58E+06	-2.08E+06
Minimum SiC radial stress (Pa)	-2.8E+07	-2.2E+07
SiC tangential stress (Pa)	-2.2E+08	-2.7E+08
Maximum SiC tangential stress (Pa)	-2.7E+07	-2.9E+07
Minimum SiC tangential stress (Pa)	-3.1E+08	-3.7E+08
IPyC Weibull failure fraction	0.2178	0.3099
SiC Weibull failure fraction	7.05E-09	2.52E-08
Kernel radius (cm)	0.0222	0.0205
Buffer thickness (cm)	8.21E-03	0.0116
IPyC thickness (cm)	3.54E-03	4.54E-03
SiC thickness (cm)	3.76E-03	3.28E-03
OPyC thickness (cm)	4.92E-03	3.76E-03
Kernel density (g/cm^3)	11.032	10.900
Buffer density (g/cm^3)	1.030	1.070
IPyC density (g/cm^3)	1.868	1.912
SiC density (g/cm^3)	3.189	3.201
OPyC density (g/cm^3)	1.921	1.893

The average Pd penetration value was 1.616E-06 m.

Results of radial stress on SiC layer are represented in Figure 4.9 and Table 4.13.

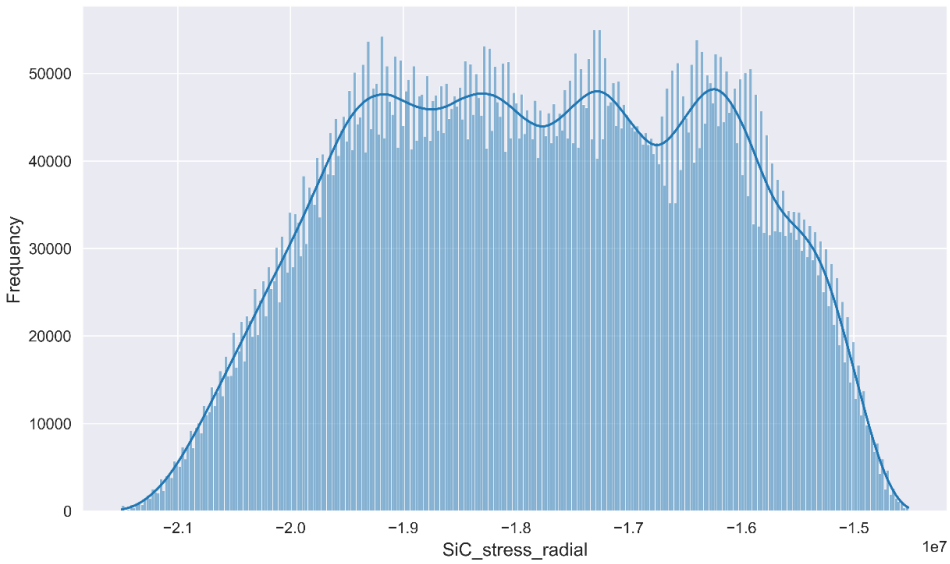

Figure 4.9: Distribution of radial stress on SiC layer

Table 4.13: Radial stress on SiC layer case description (batch 2)

Parameter	Max case	Min case
Gas pressure (Pa)	9.42E+05	1.34E+06
Pd penetration	1.62E-06	1.62E-06
SiC radial stress (Pa)	-1.45E+07	-2.15E+07
Maximum SiC radial stress (Pa)	-2.02E+06	-2.66E+06
Minimum SiC radial stress (Pa)	-2.08E+07	-2.95E+07
SiC tangential stress (Pa)	-2.32E+08	-2.50E+08
Maximum SiC tangential stress (Pa)	-2.64E+07	-3.02E+07
Minimum SiC tangential stress (Pa)	-3.28E+08	-3.57E+08
IPyC Weibull failure fraction	0.3218	0.2099
SiC Weibull failure fraction	2.31E-08	8.02E-09
Kernel radius (cm)	0.022215	0.020455
Buffer thickness (cm)	0.01157	8.21E-03
IPyC thickness (cm)	4.54E-03	3.54E-03

Parameter	Max case	Min case
SiC thickness (cm)	3.76E-03	3.28E-03
OPyC thickness (cm)	3.76E-03	4.92E-03
Kernel density (g/cm^3)	11.032	10.900
Buffer density (g/cm^3)	1.030	1.070
IPyC density (g/cm^3)	1.912	1.868
SiC density (g/cm^3)	3.205	3.201
OPyC density (g/cm^3)	1.893	1.921

The average value of radial SiC stress was -1.8E+7 Pa.

Results of tangential stress on SiC layer are represented in Figure 4.10 and Table 4.14.

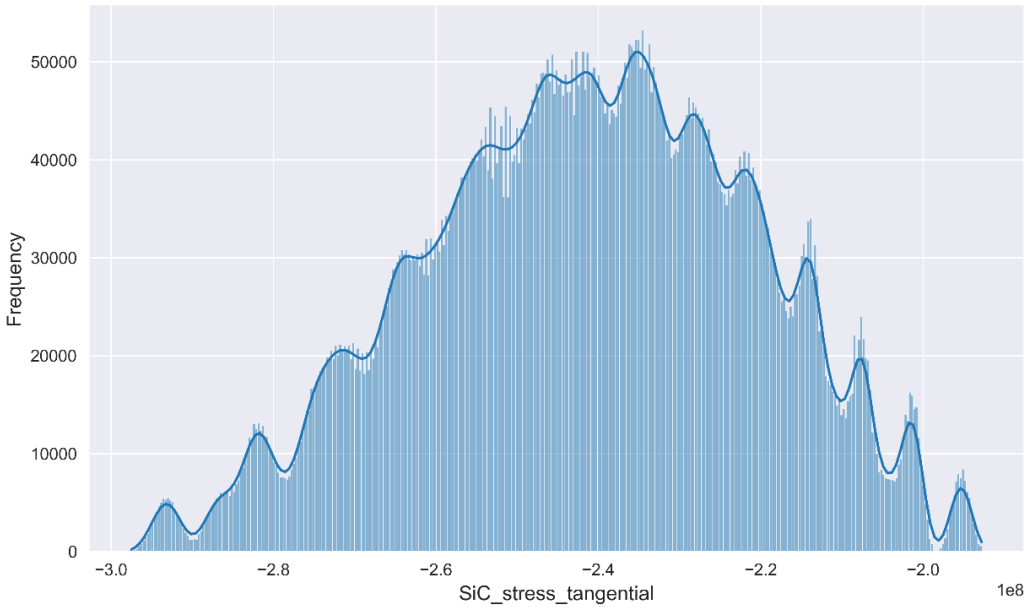

Figure 4.10: Distribution of tangential stress on SiC layer

Table 4.14: Tangential stress on SiC layer case description (batch 2)

Parameter	Max case	Min case
Gas pressure (Pa)	1.50E+06	1.29E+06
Pd penetration (m)	1.62E-06	1.62E-06

Parameter	Max case	Min case
SiC radial stress (Pa)	-1.6E+07	-2.1E+07
Maximum SiC radial stress (Pa)	-2.25E+06	-2.57E+06
Minimum SiC radial stress (Pa)	-2.3E+07	-2.8E+07
SiC tangential stress (Pa)	-1.9E+08	-3E+08
Maximum SiC tangential stress (Pa)	-2.5E+07	-3.1E+07
Minimum SiC tangential stress (Pa)	-2.9E+08	-4.1E+08
IPyC Weibull failure fraction	0.2267	0.3120
SiC Weibull failure fraction	7.95E-09	3.75E-08
Kernel radius (cm)	0.0222	0.0205
Buffer thickness (cm)	8.21E-03	8.21E-03
IPyC thickness (cm)	3.54E-03	4.54E-03
SiC thickness (cm)	3.76E-03	3.28E-03
OPyC thickness (cm)	3.76E-03	4.92E-03
Kernel density (g/cm^3)	10.900	11.032
Buffer density (g/cm^3)	1.070	1.030
IPyC density (g/cm^3)	1.868	1.912
SiC density (g/cm^3)	3.205	3.189
OPyC density (g/cm^3)	1.893	1.921

The average value of SiC tangential stress was -2.8E+7 Pa.

The results of IPyC layer failure fraction are represented in Figure 4.11 and Table 4.15.

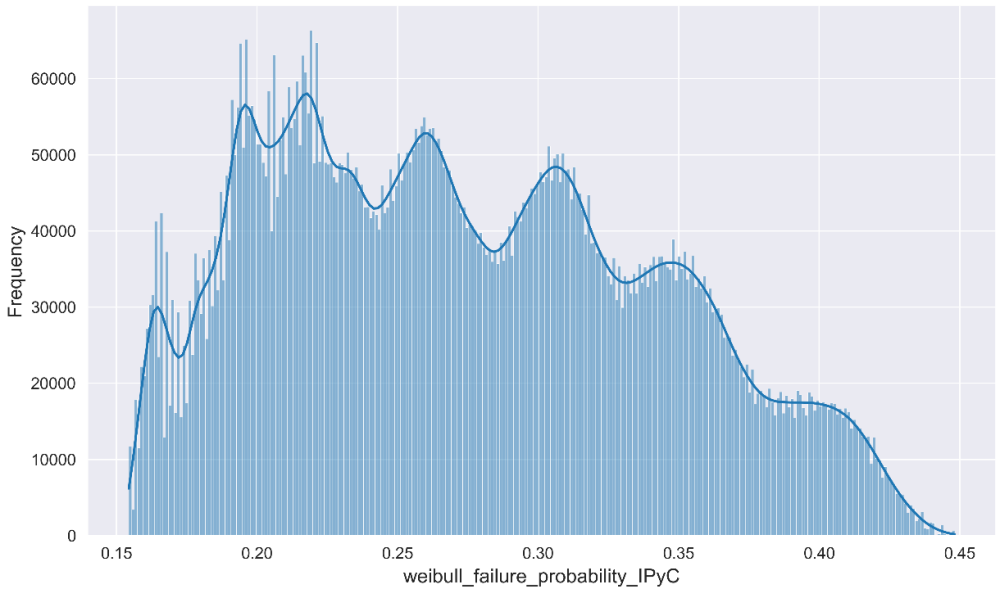

Figure 4.11: Distribution of failure fraction of IPyC layer

Table 4.15: IPyC layer failure fraction case description (batch 2)

Parameter	Max case	Min case
Gas pressure (Pa)	1.28E+06	1.20E+06
Pd penetration (m)	1.62E-06	1.62E-06
SiC radial stress (Pa)	-1.6E+07	-2E+07
Maximum SiC radial stress (Pa)	-2.24E+06	-2.48E+06
Minimum SiC radial stress (Pa)	-2.3E+07	-2.7E+07
SiC tangential stress (Pa)	-2.3E+08	-2.5E+08
Maximum SiC tangential stress (Pa)	-2.9E+07	-2.8E+07
Minimum SiC tangential stress (Pa)	-3.4E+08	-3.5E+08
IPyC Weibull failure fraction	0.4482	0.1544
SiC Weibull failure fraction	6.05E-08	3.90E-09
Kernel radius (cm)	0.0205	0.0222
Buffer thickness (cm)	8.21E-03	9.89E-03
IPyC thickness (cm)	4.54E-03	3.54E-03

Parameter	Max case	Min case
SiC thickness (cm)	3.76E-03	3.28E-03
OPyC thickness (cm)	3.76E-03	4.92E-03
Kernel density (g/cm^3)	11.032	10.900
Buffer density (g/cm^3)	1.030	1.070
IPyC density (g/cm^3)	1.868	1.912
SiC density (g/cm^3)	3.189	3.205
OPyC density (g/cm^3)	1.893	1.921

The average value of IPyC Weibull failure fraction was 0.2741.

The results of SiC layer failure fraction are represented in Figure 4.12 and Table 4.16.

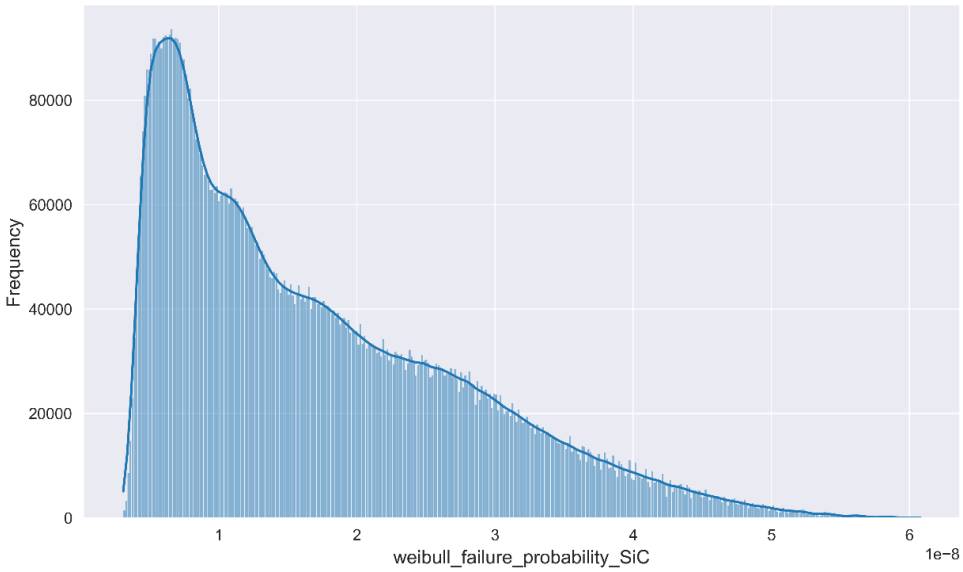

Figure 4.12: Distribution of failure fraction of SiC layer

Table 4.16: SiC layer failure fraction case description (batch 2)

Parameter	Max case	Min case
Gas pressure (Pa)	1.28E+06	9.81E+05
Pd penetration (m)	1.62E-06	1.62E-06
SiC radial stress (Pa)	-1.6E+07	-1.9E+07

Parameter	Max case	Min case
Maximum SiC radial stress (Pa)	-2.05E+06	-2.61E+06
Minimum SiC radial stress (Pa)	-2.3E+07	-2.7E+07
SiC tangential stress (Pa)	-2.4E+08	-2.5E+08
Maximum SiC tangential stress (Pa)	-2.8E+07	-3E+07
Minimum SiC tangential stress (Pa)	-3.4E+08	-3.5E+08
IPyC Weibull failure fraction	0.4475	0.1550
SiC Weibull failure fraction	6.08E-08	3.09E-09
Kernel radius (cm)	0.0205	0.0222
Buffer thickness (cm)	8.21E-03	0.00116
IPyC thickness (cm)	4.54E-03	3.54E-03
SiC thickness (cm)	3.76E-03	3.28E-03
OPyC thickness (cm)	3.76E-03	4.92E-03
Kernel density (g/cm^3)	11.032	10.900
Buffer density (g/cm^3)	1.030	1.070
IPyC density (g/cm^3)	1.868	1.912
SiC density (g/cm^3)	3.189	3.189
OPyC density (g/cm^3)	1.921	1.893

The average value of SiC Weibull failure fraction was 1.71E-08.

4.2.3 Results of Uncertainty Analysis-batch 3

The results for the gas pressure in the buffer layer are presented in Figure 4.13 and Table 4.17.

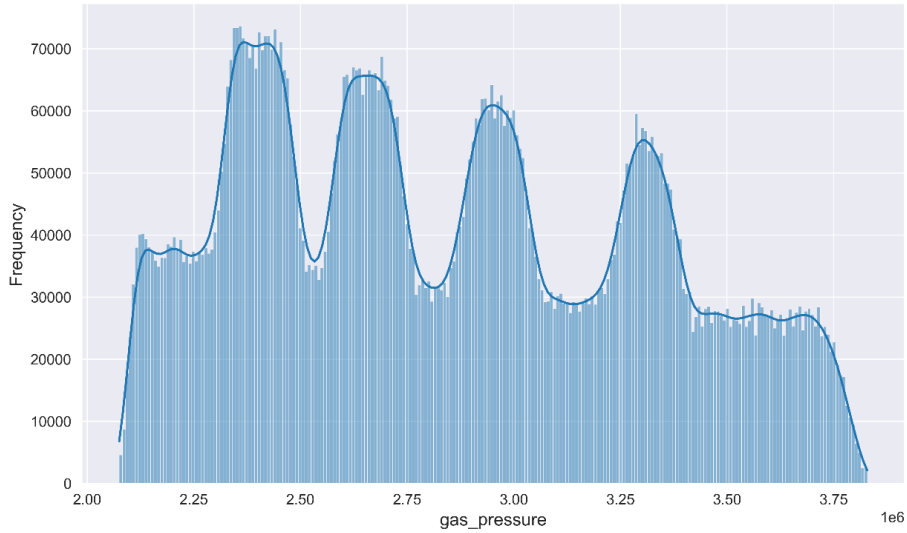

Figure 4.13: Distribution of gas pressure in buffer layer (batch 3)

Table 4.17: Pressure case description: batch 3

Parameter	Max case	Min case
Gas pressure (Pa)	3.83E+06	2.07E+06
Pd penetration (m)	2.77E-06	2.77E-06
SiC radial stress (Pa)	-1.6E+07	-1.1E+07
Maximum SiC radial stress (Pa)	-2.58E+06	-2.07E+06
Minimum SiC radial stress (Pa)	-2.8E+07	-2.2E+07
SiC tangential stress (Pa)	-1.7E+08	-1.6E+08
Maximum SiC tangential stress (Pa)	-2.8E+07	-2.9E+07
Minimum SiC tangential stress (Pa)	-3.5E+08	-3.4E+08
IPyC Weibull failure fraction	0.1548	0.4244
SiC Weibull failure fraction	4.96E-09	3.62E-08
Kernel radius (cm)	0.0222	0.0205
Buffer thickness (cm)	8.21E-03	0.0116
IPyC thickness (cm)	3.54E-03	4.54E-03

Parameter	Max case	Min case
SiC thickness (cm)	3.28E-03	3.76E-03
OPyC thickness (cm)	4.92E-03	3.76E-03
Kernel density (g/cm^3)	10.900	11.032
Buffer density (g/cm^3)	1.070	1.030
IPyC density (g/cm^3)	1.912	1.868
SiC density (g/cm^3)	3.197	3.193
OPyC density (g/cm^3)	1.921	1.893

The average value of pressure was 2.85E+06 Pa.

The results for Pd penetration into the SiC layer are presented in Figure 4.14 and Table 4.18.

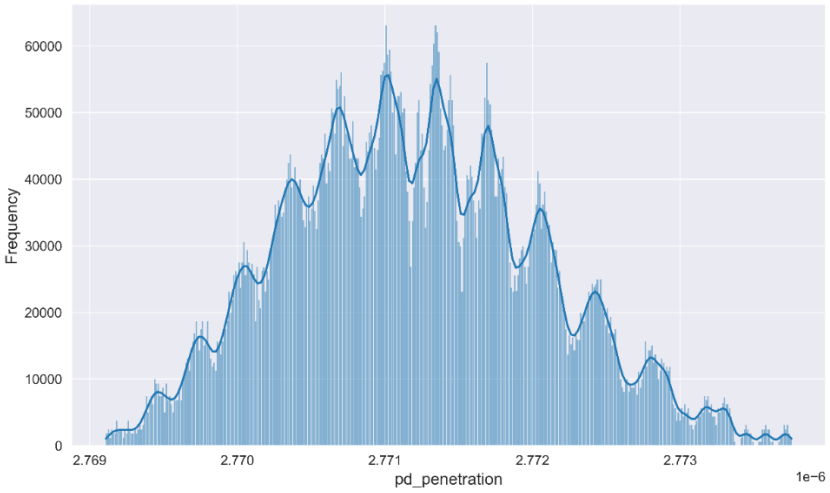

Figure 4.14: Distribution of Distribution of Pd penetration into SiC layer

Table 4.18: Pd penetration description (batch 3)

Parameter	Max case	Min case
Gas pressure (Pa)	3.73E+06	2.14E+06
Pd penetration (m)	2.77E-06	2.77E-06
SiC radial stress (Pa)	-1.5E+07	-1.1E+07
Maximum SiC radial stress (Pa)	-2.61E+06	-2.04E+06

Parameter	Max case	Min case
Minimum SiC radial stress (Pa)	-2.8E+07	-2.2E+07
SiC tangential stress (Pa)	-1.5E+08	-1.8E+08
Maximum SiC tangential stress (Pa)	-2.6E+07	-3.2E+07
Minimum SiC tangential stress (Pa)	-3.1E+08	-3.8E+08
IPyC Weibull failure fraction	0.1643	0.4050
SiC Weibull failure fraction	5.83E-09	3.09E-08
Kernel radius (cm)	0.0222	0.0205
Buffer thickness (cm)	8.21E-03	0.0116
IPyC thickness (cm)	3.54E-03	4.54E-03
SiC thickness (cm)	3.76E-03	3.28E-03
OPyC thickness (cm)	4.92E-03	3.76E-03
Kernel density (g/cm^3)	11.032	10.900
Buffer density (g/cm^3)	1.030	1.070
IPyC density (g/cm^3)	1.912	1.868
SiC density (g/cm^3)	3.189	3.201
OPyC density (g/cm^3)	1.921	1.893

The average value of Pd penetration was 2.77E-06 m. The results for the radial stress on the SiC layer are presented in Figure 4.15 and Table 4.19.

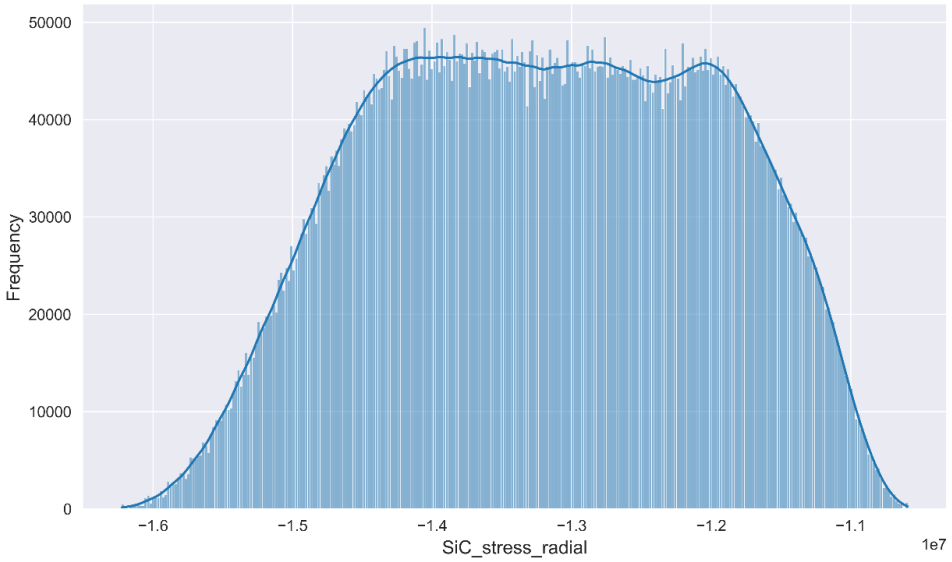

Figure 4.15: Distribution of radial stress on SiC layer

Table 4.19: Radial stress on SiC layer: case description (batch 3)

Parameter	Max case	Min case
Gas pressure (Pa)	2.40E+06	3.36E+06
Pd penetration (m)	2.77E-06	2.77E-06
SiC radial stress (Pa)	-1.06E+07	-1.62E+07
Maximum SiC radial stress (Pa)	-2.02E+06	-2.66E+06
Minimum SiC radial stress (Pa)	-2.08E+07	-2.95E+07
SiC tangential stress (Pa)	-1.58E+08	-1.69E+08
Maximum SiC tangential stress (Pa)	-2.64E+07	-3.02E+07
Minimum SiC tangential stress (Pa)	-3.28E+08	-3.57E+08
IPyC Weibull failure fraction	0.3218	0.2099
SiC Weibull failure fraction	2.31E-08	8.02E-09
Kernel radius (cm)	0.022215	0.020455
Buffer thickness (cm)	0.0001157	8.21E-03
IPyC thickness (cm)	4.54E-03	3.54E-03

Parameter	Max case	Min case
SiC thickness (cm)	3.76E-03	3.28E-03
OPyC thickness (cm)	3.76E-03	4.92E-03
Kernel density (g/cm^3)	11.032	10.900
Buffer density (g/cm^3)	1.030	1.070
IPyC density (g/cm^3)	1.912	1.868
SiC density (g/cm^3)	3.193	3.193
OPyC density (g/cm^3)	1.893	1.921

The average value of SiC radial stress was -1.3E+07 Pa.

Results of tangential stress on SiC layer are represented in Figure 4.16 and Table 4.20.

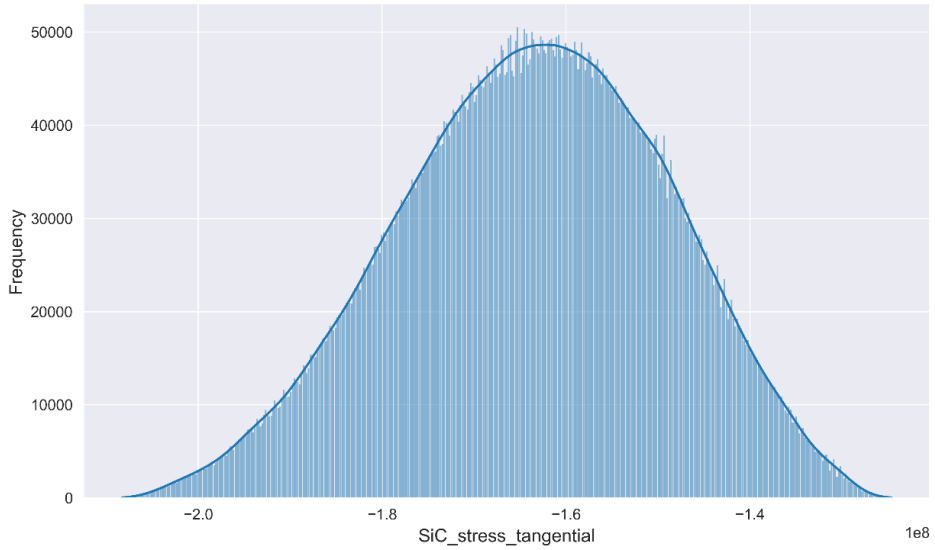

Figure 4.16: Distribution of tangential stress on SiC layer

Table 4.20: Tangential stress on SiC layer case description (batch 3)

Parameter	Max case	Min case
Gas pressure (Pa)	2.45E+06	3.23E+06
Pd penetration (m)	2.77E-06	2.77E-06
SiC radial stress (Pa)	-1.1E+07	-1.5E+07

Parameter	Max case	Min case
Maximum SiC radial stress (Pa)	-1.93E+06	-2.77E+06
Minimum SiC radial stress (Pa)	-2.1E+07	-2.9E+07
SiC tangential stress (Pa)	-1.3E+08	-2E+08
Maximum SiC tangential stress (Pa)	-2.3E+07	-3.5E+07
Minimum SiC tangential stress (Pa)	-2.8E+08	-4.2E+08
IPyC Weibull failure fraction	0.1717	0.4124
SiC Weibull failure fraction	4.19E-09	4.61E-08
Kernel radius (cm)	0.0222	0.0205
Buffer thickness (cm)	0.0116	8.21E-03
IPyC thickness (cm)	3.54E-03	4.54E-03
SiC thickness (cm)	3.76E-03	3.28E-03
OPyC thickness (cm)	3.76E-03	4.92E-03
Kernel density (g/cm^3)	10.933	10.933
Buffer density (g/cm^3)	1.040	1.040
IPyC density (g/cm^3)	1.912	1.868
SiC density (g/cm^3)	3.197	3.193
OPyC density (g/cm^3)	1.921	1.893

The average value of SiC tangential stress was -2.84E+08 Pa.

Results of IPyC layer failure fraction are represented in Figure 4.17 and Table 4.21.

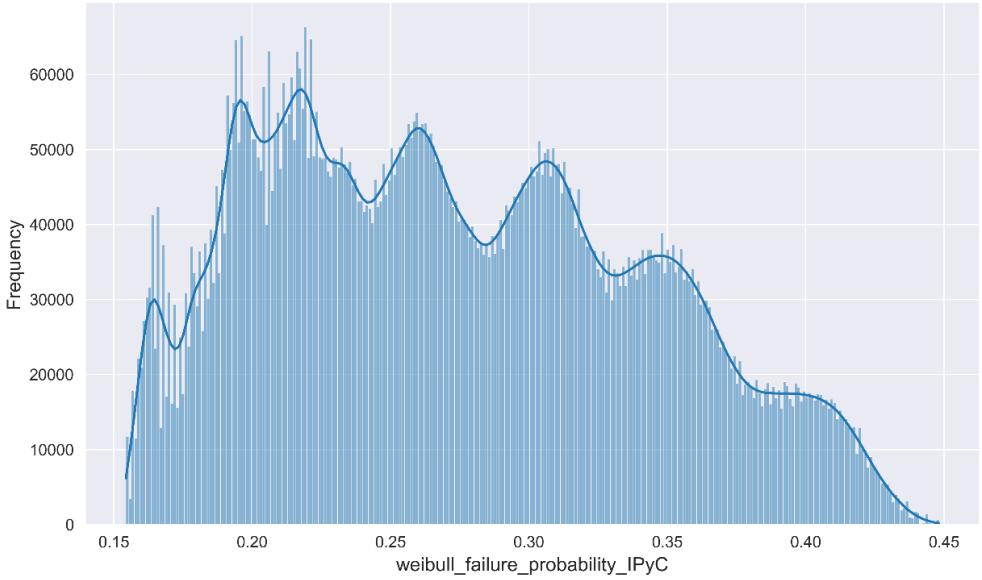

Figure 4.17: Distribution of failure fraction of IPyC layer

Table 4.21: IPyC layer failure fraction case description (batch 3)

Parameter	Max case	Min case
Gas pressure (Pa)	3.20E+06	3.07E+06
Pd penetration (m)	2.77E-06	2.77E-06
SiC radial stress (Pa)	-1.2E+07	-1.5E+07
Maximum SiC radial stress (Pa)	-2.24E+06	-2.48E+06
Minimum SiC radial stress (Pa)	-2.3E+07	-2.7E+07
SiC tangential stress (Pa)	-1.6E+08	-1.7E+08
Maximum SiC tangential stress (Pa)	-2.9E+07	-2.8E+07
Minimum SiC tangential stress (Pa)	-3.4E+08	-3.5E+08
IPyC Weibull failure fraction	0.4482	0.1544
SiC Weibull failure fraction	6.05E-08	3.90E-09
Kernel radius (cm)	0.0205	0.0222
Buffer thickness (cm)	8.21E-03	9.89E-03
IPyC thickness (cm)	4.54E-03	3.54E-03

Parameter	Max case	Min case
SiC thickness (cm)	3.76E-03	3.28E-03
OPyC thickness (cm)	3.76E-03	4.92E-03
Kernel density (g/cm^3)	11.032	10.900
Buffer density (g/cm^3)	1.030	1.070
IPyC density (g/cm^3)	1.868	1.912
SiC density (g/cm^3)	3.189	3.205
OPyC density (g/cm^3)	1.893	1.921

The average value of IPyC Weibull failure fraction was 0.2741.

Results of SiC layer failure fraction are represented in Figure 4.18 and Table 4.22.

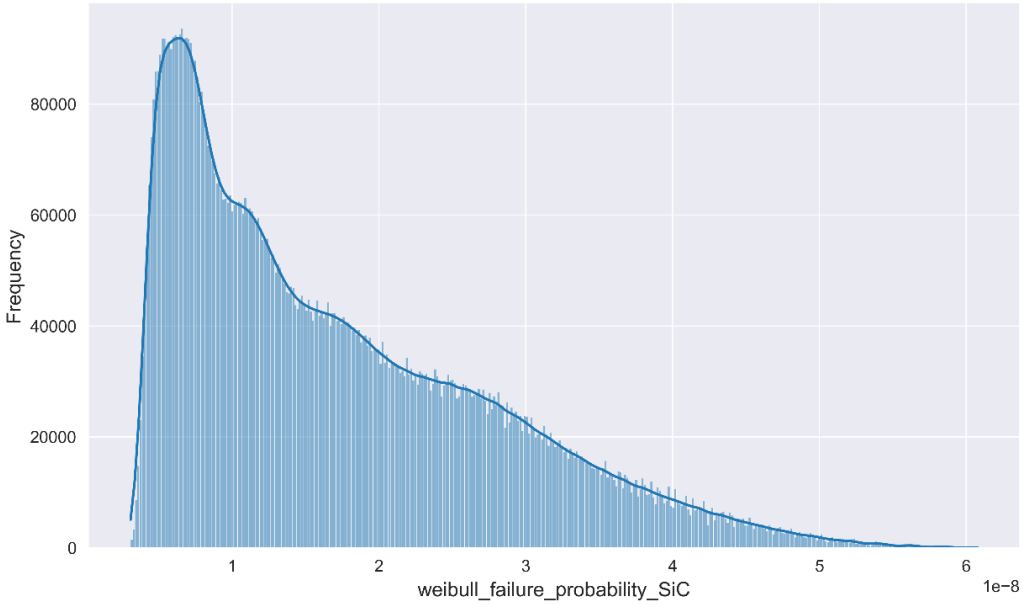

Figure 4.18: Distribution of failure fraction of SiC layer

Table 4.22: SiC layer failure fraction case description (batch 3)

Parameter	Max case	Min case
Gas pressure (Pa)	3.20E+06	2.51E+06
Pd penetration (m)	2.77E-06	2.77E-06

Parameter	Max case	Min case
SiC radial stress (Pa)	-1.2E+07	-1.4E+07
Maximum SiC radial stress (Pa)	-2.05E+06	-2.61E+06
Minimum SiC radial stress (Pa)	-2.3E+07	-2.7E+07
SiC tangential stress (Pa)	-1.6E+08	-1.7E+08
Maximum SiC tangential stress (Pa)	-2.8E+07	-3E+07
Minimum SiC tangential stress (Pa)	-3.4E+08	-3.5E+08
IPyC Weibull failure fraction	0.4475	0.1550
SiC Weibull failure fraction	6.08E-08	3.09E-09
Kernel radius (cm)	0.0205	0.0222
Buffer thickness (cm)	8.21E-03	0.0116
IPyC thickness (cm)	4.54E-03	3.54E-03
SiC thickness (cm)	3.76E-03	3.28E-03
OPyC thickness (cm)	3.76E-03	4.92E-03
Kernel density (g/cm^3)	11.032	10.900
Buffer density (g/cm^3)	1.030	1.070
IPyC density (g/cm^3)	1.868	1.912
SiC density (g/cm^3)	3.189	3.189
OPyC density (g/cm^3)	1.921	1.893

The average value of IPyC Weibull failure fraction was 1.71E-08.

4.2.4 Results of Uncertainty Analysis-batch 4

Results of gas pressure in the buffer layer are represented in Figure 4.19 and Table 4.23.

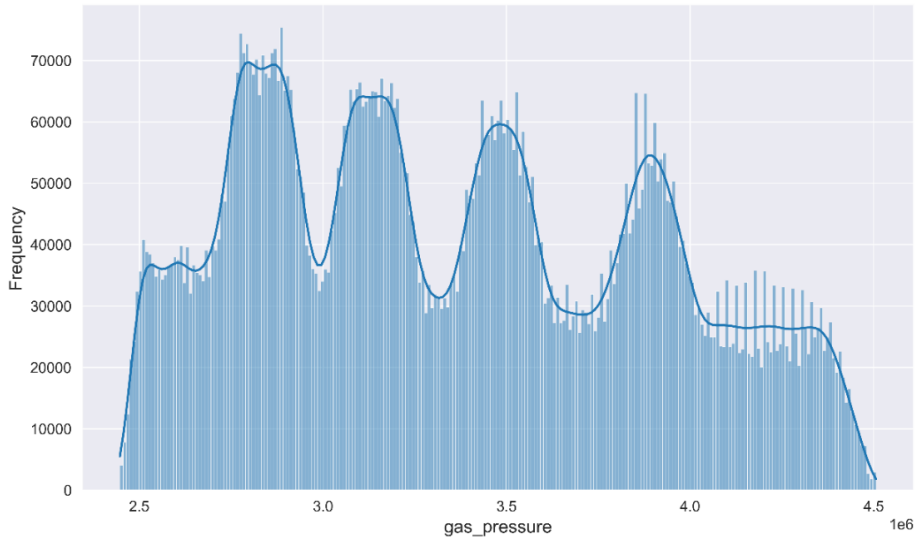

Figure 4.19: Distribution of gas pressure in buffer layer (batch 4)

Table 4.23: Pressure case description: batch 4

Parameter	Max case	Min case
Gas pressure (Pa)	4.51E+06	2.45E+06
Pd penetration (m)	3.77E-06	3.76E-06
SiC radial stress (Pa)	-1.4E+07	-9467388
Maximum SiC radial stress (Pa)	-2.58E+06	-2.07E+06
Minimum SiC radial stress (Pa)	-2.8E+07	-2.2E+07
SiC tangential stress (Pa)	-1.4E+08	-1.3E+08
Maximum SiC tangential stress (Pa)	-2.8E+07	-2.9E+07
Minimum SiC tangential stress (Pa)	-3.5E+08	-3.4E+08
IPyC Weibull failure fraction	0.1548	0.4244
SiC Weibull failure fraction	4.96E-09	3.62E-08
Kernel radius (cm)	0.0222	0.0205
Buffer thickness (cm)	8.21E-03	0.0116
IPyC thickness (cm)	3.54E-03	4.54E-03

Parameter	Max case	Min case
SiC thickness (cm)	3.28E-03	3.76E-03
OPyC thickness (cm)	4.92E-03	3.76E-03
Kernel density (g/cm^3)	10.900	11.032
Buffer density (g/cm^3)	1.070	1.030
IPyC density (g/cm^3)	1.912	1.868
SiC density (g/cm^3)	3.189	3.205

The average value of pressure was 3.36E+06 Pa.

Results of palladium penetration into SiC layer are represented in Figure 4.20 and Table 4.24.

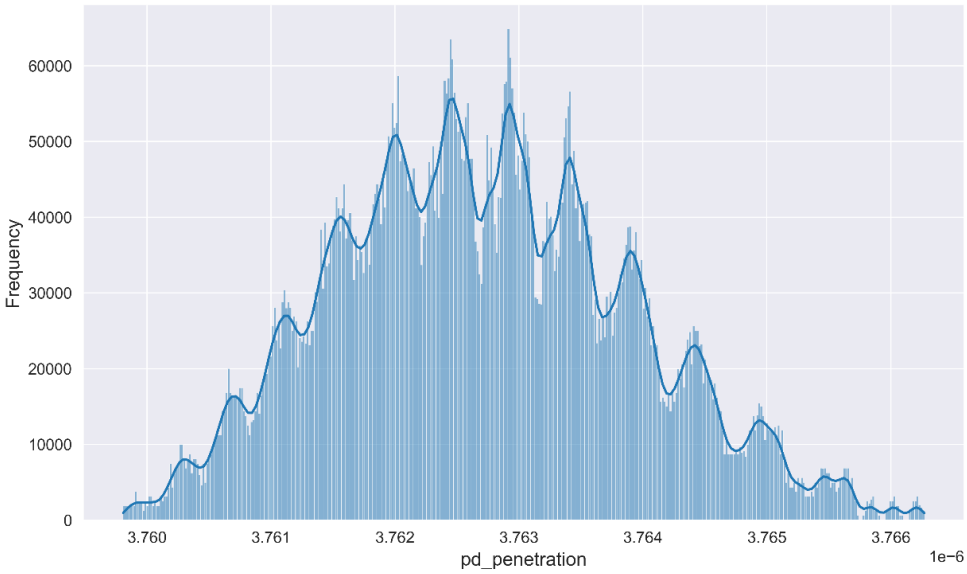

Figure 4.20: Distribution of Pd penetration into SiC layer

Table 4.24: Pd penetration description (batch 4)

Parameter	Max case	Min case
Gas pressure (Pa)	4.39E+06	2.52E+06
Pd penetration (m)	3.77E-06	3.76E-06
SiC radial stress (Pa)	-1.4E+07	-9585004
Maximum SiC radial stress (Pa)	-2.61E+06	-2.04E+06

Parameter	Max case	Min case
Minimum SiC radial stress (Pa)	-2.8E+07	-2.2E+07
SiC tangential stress (Pa)	-1.2E+08	-1.4E+08
Maximum SiC tangential stress (Pa)	-2.6E+07	-3.2E+07
Minimum SiC tangential stress (Pa)	-3.1E+08	-3.8E+08
IPyC Weibull failure fraction	0.1643	0.4050
SiC Weibull failure fraction	5.83E-09	3.09E-08
Kernel radius (cm)	0.0222	0.0205
Buffer thickness (cm)	8.21E-03	0.0116
IPyC thickness (cm)	3.54E-03	4.54E-03
SiC thickness (cm)	3.76E-03	3.28E-03
OPyC thickness (cm)	4.92E-03	3.76E-03
Kernel density (g/cm^3)	11.032	10.900
Buffer density (g/cm^3)	1.030	1.070
IPyC density (g/cm^3)	1.912	1.868
SiC density (g/cm^3)	3.197	3.205
OPyC density (g/cm^3)	1.921	1.893

The average value of Pd penetration was 3.763E-06 m.

Results of radial stress on SiC layer are represented in Figure 4.21 and Table 4.25.

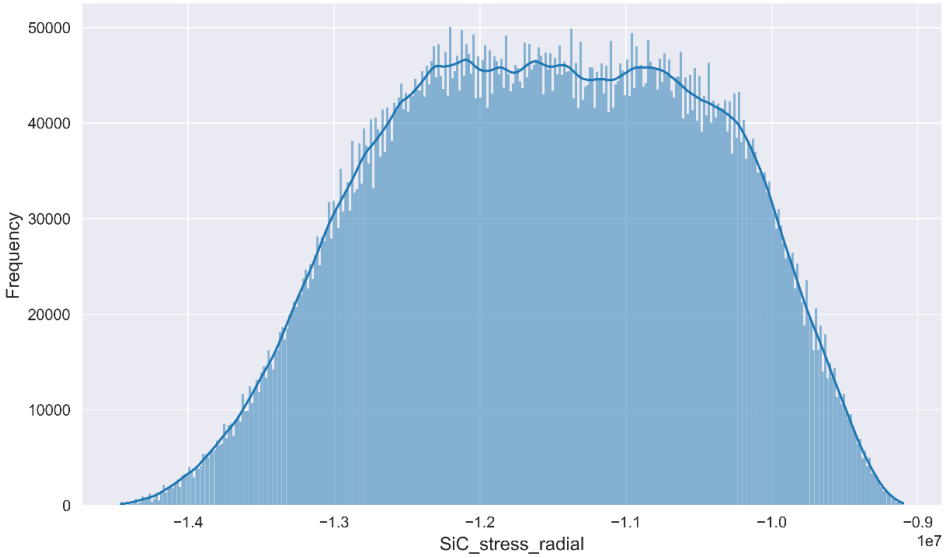

Figure 4.21: Distribution of radial stress on SiC layer

Table 4.25: Radial stress on SiC layer: case description (batch 4)

Parameter	Max case	Min case
Gas pressure (Pa)	2.84E+06	3.96E+06
Pd penetration (m)	3.76E-06	3.76E-06
SiC radial stress (Pa)	-9.10E+06	-1.40E+07
Maximum SiC radial stress (Pa)	-2.02E+06	-2.66E+06
Minimum SiC radial stress (Pa)	-2.1E+07	-3E+07
SiC tangential stress (Pa)	-1.3E+08	-1.4E+08
Maximum SiC tangential stress (Pa)	-2.6E+07	-3E+07
Minimum SiC tangential stress (Pa)	-3.3E+08	-3.6E+08
IPyC Weibull failure fraction	0.3218	0.2099
SiC Weibull failure fraction	2.31E-08	8.02E-09
Kernel radius (cm)	0.0222	0.0205
Buffer thickness (cm)	0.0116	8.21E-03
IPyC thickness (cm)	4.54E-03	3.54E-03

Parameter	Max case	Min case
SiC thickness (cm)	3.76E-03	3.28E-03
OPyC thickness (cm)	3.76E-03	4.92E-03
Kernel density (g/cm^3)	11.032	10.900
Buffer density (g/cm^3)	1.030	1.070
IPyC density (g/cm^3)	1.912	1.868
SiC density (g/cm^3)	3.205	3.189
OPyC density (g/cm^3)	1.893	1.921

The average value of SiC tangential stress was -1.2E+07 Pa.

Results of tangential stress on SiC layer are represented in Figure 4.22 and Table 4.26.

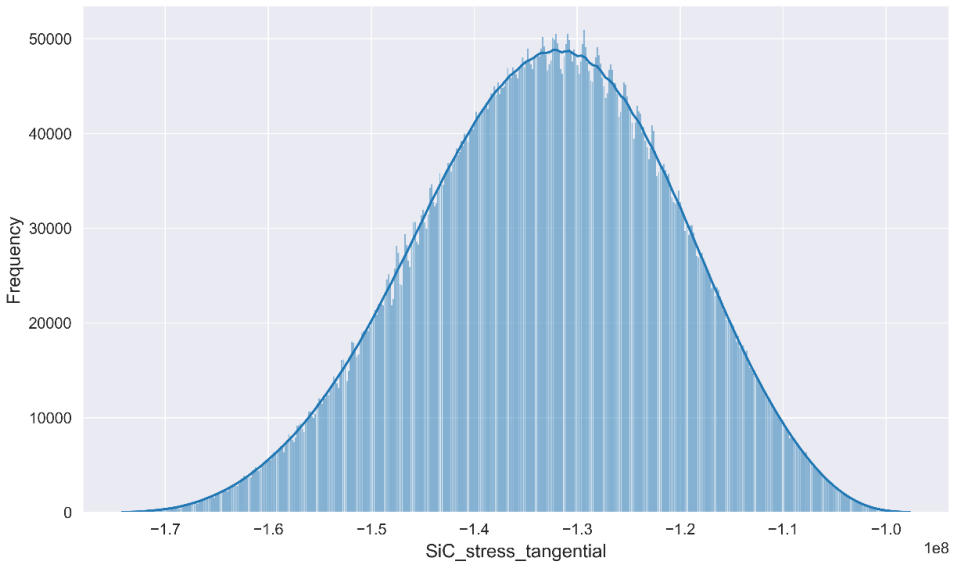

Figure 4.22: Distribution of tangential stress on SiC layer

Table 4.26: Tangential stress on SiC layer case description (batch 4)

Parameter	Max case	Min case
Gas pressure (Pa)	2.83E+06	3.96E+06
Pd penetration (m)	3.76E-06	3.76E-06

Parameter	Max case	Min case
SiC radial stress (Pa)	-9.75E+06	-1.30E+07
Maximum SiC radial stress (Pa)	-1.84E+06	-2.91E+06
Minimum SiC radial stress (Pa)	-2E+07	-3E+07
SiC tangential stress (Pa)	-1.3E+08	-1.3E+08
Maximum SiC tangential stress (Pa)	-2.6E+07	-3.2E+07
Minimum SiC tangential stress (Pa)	-3.3E+08	-3.6E+08
IPyC Weibull failure fraction	0.3480	0.2105
SiC Weibull failure fraction	2.47E-08	7.97E-09
Kernel radius (cm)	0.0222	0.0205
Buffer thickness (cm)	0.0116	8.21E-03
IPyC thickness (cm)	4.54E-03	3.54E-03
SiC thickness (cm)	3.76E-03	3.28E-03
OPyC thickness (cm)	3.76E-03	4.92E-03
Kernel density (g/cm^3)	11.032	10.900
Buffer density (g/cm^3)	1.030	1.070
IPyC density (g/cm^3)	1.901	1.868
SiC density (g/cm^3)	3.189	3.189
OPyC density (g/cm^3)	1.921	1.893

The average value of SiC radial stress was -2.49E+07 Pa.

Results of IPyC layer failure fraction are represented in Figure 4.23 and Table 4.27.

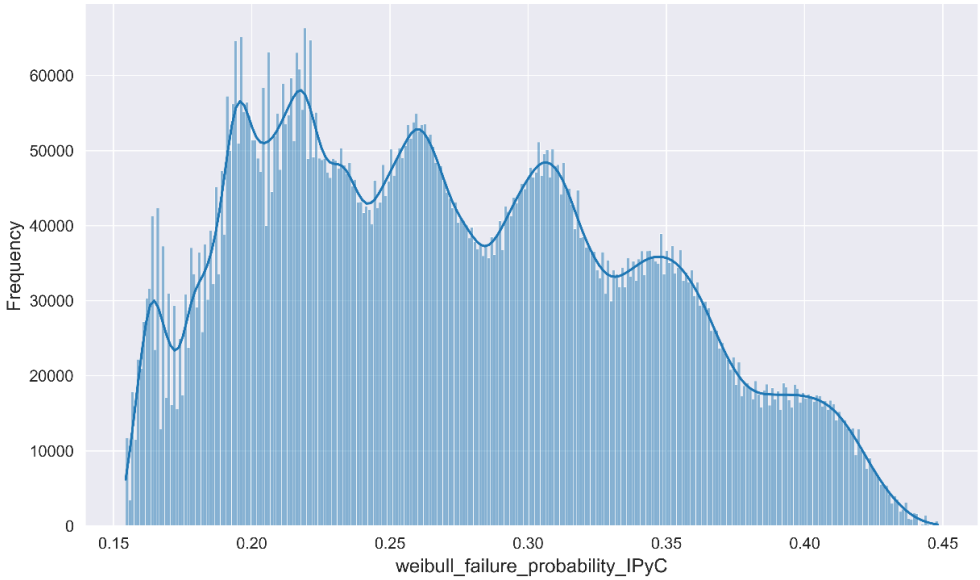

Figure 4.23: IPyC layer failure fraction

Table 4.27: IPyC layer failure fraction case description (batch 4)

Parameter	Max case	Min case
Gas pressure (Pa)	3.76E+06	3.62E+06
Pd penetration (m)	3.76E-06	3.77E-06
SiC radial stress (Pa)	-1E+07	-1.3E+07
Maximum SiC radial stress (Pa)	-2.24E+06	-2.48E+06
Minimum SiC radial stress (Pa)	-2.3E+07	-2.7E+07
SiC tangential stress (Pa)	-1.2E+08	-1.4E+08
Maximum SiC tangential stress (Pa)	-2.9E+07	-2.8E+07
Minimum SiC tangential stress (Pa)	-3.4E+08	-3.5E+08
IPyC Weibull failure fraction	0.4482	0.1544
SiC Weibull failure fraction	6.05E-08	3.90E-09
Kernel radius (cm)	0.0205	0.0222
Buffer thickness (cm)	8.21E-03	9.89E-03
IPyC thickness (cm)	4.54E-03	3.54E-03
SiC thickness (cm)	3.76E-03	3.28E-03

Parameter	Max case	Min case
OPyC thickness (cm)	3.76E-03	4.92E-03
Kernel density (g/cm^3)	11.032	10.900
Buffer density (g/cm^3)	1.030	1.070
IPyC density (g/cm^3)	1.868	1.912
SiC density (g/cm^3)	3.189	3.205
OPyC density (g/cm^3)	1.893	1.921

The average value of IPyC Weibull failure fraction was 0.2741.

Results of SiC layer failure fraction are represented in Figure 4.24 and Table 4.28.

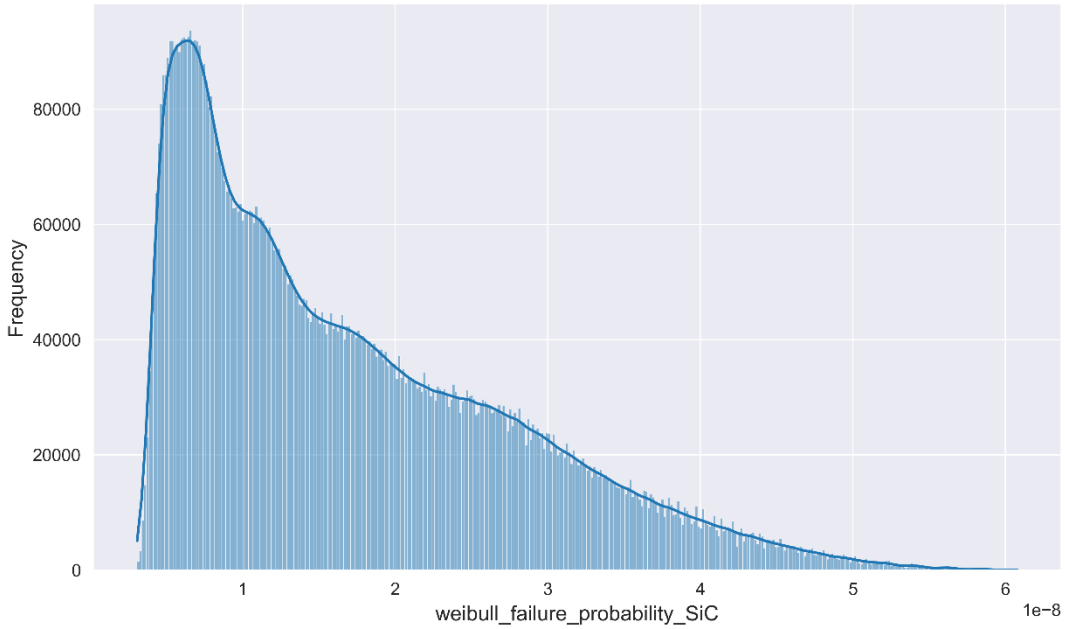

Figure 4.24: Distribution of failure fraction of SiC layer

Table 4.28: SiC layer failure fraction case description (batch 4)

Parameter	Max case	Min case
Gas pressure (Pa)	3.76E+06	2.97E+06
Pd penetration (m)	3.76E-06	3.76E-06
SiC radial stress (Pa)	-1.1E+07	-1.2E+07

Parameter	Max case	Min case
Maximum SiC radial stress (Pa)	-2.05E+06	-2.61E+06
Minimum SiC radial stress (Pa)	-2.3E+07	-2.7E+07
SiC tangential stress (Pa)	-1.3E+08	-1.4E+08
Maximum SiC tangential stress (Pa)	-2.8E+07	-3E+07
Minimum SiC tangential stress (Pa)	-3.4E+08	-3.5E+08
IPyC Weibull failure fraction	0.4475	0.1550
SiC Weibull failure fraction	6.08E-08	3.09E-09
Kernel radius (cm)	0.0205	0.0222
Buffer thickness (cm)	8.21E-03	0.0116
IPyC thickness (cm)	4.54E-03	3.54E-03
SiC thickness (cm)	3.76E-03	3.28E-03
OPyC thickness (cm)	3.76E-03	4.92E-03
Kernel density (g/cm^3)	11.032	10.900
Buffer density (g/cm^3)	1.030	1.070
IPyC density (g/cm^3)	1.868	1.912
SiC density (g/cm^3)	3.189	3.189
OPyC density (g/cm^3)	1.921	1.893

The average value of SiC Weibull failure fraction was 1.71E-08.

4.2.5 Results of Uncertainty Analysis-batch 5

The results for the gas pressure in the buffer layer are presented in Figure 4.25 and Table 4.29.

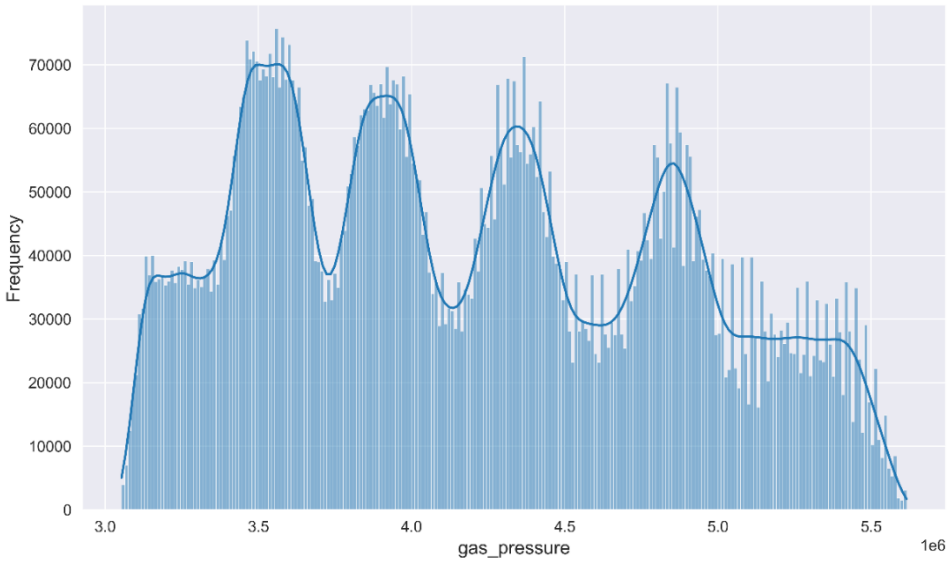

Figure 4.25: Distribution of gas pressure in buffer layer (batch 5)

Table 4.29: Pressure case description: batch 5

Parameter	Max case	Min case
Gas pressure (Pa)	5.62E+06	3.05E+06
Pd penetration (m)	5.09E-06	5.09E-06
SiC radial stress (Pa)	-1.1E+07	-7097138
Maximum SiC radial stress (Pa)	-2.58E+06	-2.07E+06
Minimum SiC radial stress (Pa)	-2.8E+07	-2.2E+07
SiC tangential stress (Pa)	-9.5E+07	-8.3E+07
Maximum SiC tangential stress (Pa)	-2.8E+07	-2.9E+07
Minimum SiC tangential stress (Pa)	-3.5E+08	-3.4E+08
IPyC Weibull failure fraction	0.1548	0.4244
SiC Weibull failure fraction	4.96E-09	3.62E-08
Kernel radius (cm)	0.0222	0.0205
Buffer thickness (cm)	8.21E-03	0.0116
IPyC thickness (cm)	3.54E-03	4.54E-03

Parameter	Max case	Min case
SiC thickness (cm)	3.28E-03	3.76E-03
OPyC thickness (cm)	4.92E-03	3.76E-03
Kernel density (g/cm^3)	10.900	11.032
Buffer density (g/cm^3)	1.070	1.030
IPyC density (g/cm^3)	1.912	1.868
SiC density (g/cm^3)	3.189	3.205
OPyC density (g/cm^3)	1.921	1.893

The average pressure value was 4.19E+06 Pa.

Results of palladium penetration into SiC layer are represented in Figure 4.26 and Table 4.30.

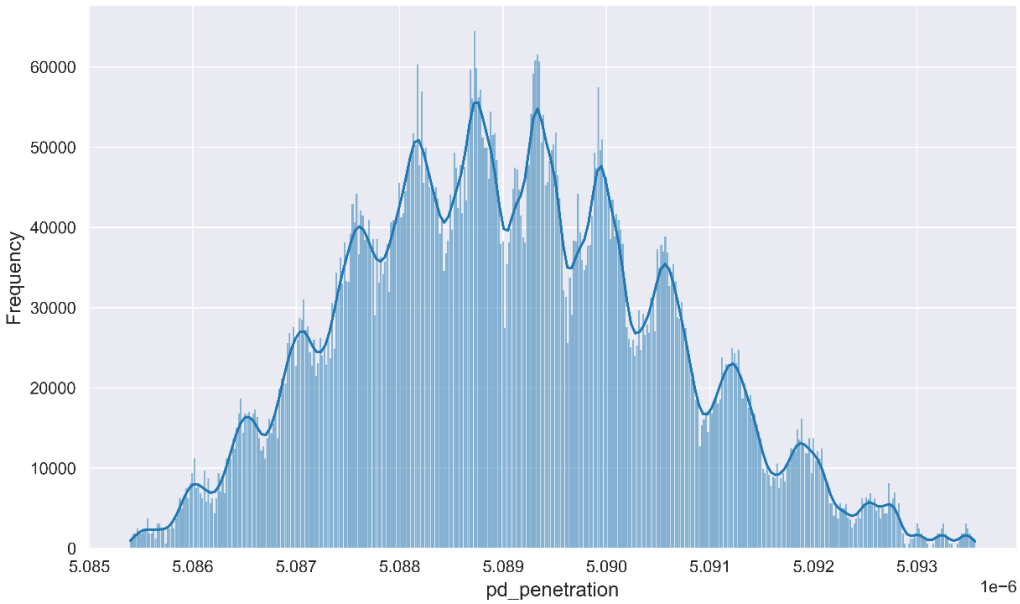

Figure 4.26: Distribution of Pd penetration into SiC layer

Table 4.30: Pd penetration description (batch 5)

Parameter	Max case	Min case
Gas pressure (Pa)	5.47E+06	3.14E+06
Pd penetration (m)	5.09E-06	5.09E-06

Parameter	Max case	Min case
SiC radial stress (Pa)	-1.1E+07	-7182571
Maximum SiC radial stress (Pa)	-2.61E+06	-2.04E+06
Minimum SiC radial stress (Pa)	-2.8E+07	-2.2E+07
SiC tangential stress (Pa)	-8.4E+07	-9.4E+07
Maximum SiC tangential stress (Pa)	-2.6E+07	-3.2E+07
Minimum SiC tangential stress (Pa)	-3.1E+08	-3.8E+08
IPyC Weibull failure fraction	0.1643	0.4050
SiC Weibull failure fraction	5.83E-09	3.09E-08
Kernel radius (cm)	0.0222	0.0205
Buffer thickness (cm)	8.21E-03	0.0116
IPyC thickness (cm)	3.54E-03	4.54E-03
SiC thickness (cm)	3.76E-03	3.28E-03
OPyC thickness (cm)	4.92E-03	3.76E-03
Kernel density (g/cm^3)	11.032	10.900
Buffer density (g/cm^3)	1.030	1.070
IPyC density (g/cm^3)	1.912	1.868
SiC density (g/cm^3)	3.197	3.205
OPyC density (g/cm^3)	1.921	1.893

The average value of Pd penetration was 5.09E-06 m.

Results of max radial stress on SiC layer are represented in Figure 4.27 and Table 4.31.

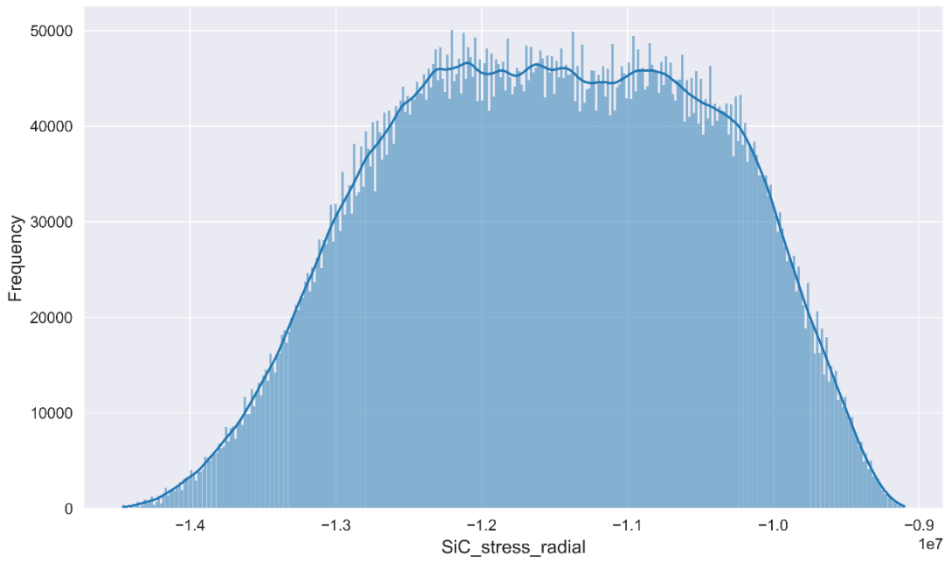

Figure 4.27: Distribution of radial stress on SiC layer

Table 4.31: Radial stress on SiC layer case description (batch 5)

Parameter	Max case	Min case
Gas pressure (Pa)	3.54E+06	4.94E+06
Pd penetration (m)	5.09E-06	5.09E-06
SiC radial stress (Pa)	-6.81E+06	-1.10E+07
Maximum SiC radial stress (Pa)	-2.02E+06	-2.66E+06
Minimum SiC radial stress (Pa)	-2.1E+07	-3E+07
SiC tangential stress (Pa)	-8.7E+07	-9.2E+07
Maximum SiC tangential stress (Pa)	-2.6E+07	-3E+07
Minimum SiC tangential stress (Pa)	-3.3E+08	-3.6E+08
IPyC Weibull failure fraction	0.3218	0.2099
SiC Weibull failure fraction	2.31E-08	8.02E-09
Kernel radius (cm)	0.0222	0.0205
Buffer thickness (cm)	0.0116	8.21E-03
IPyC thickness (cm)	4.54E-03	3.54E-03

Parameter	Max case	Min case
SiC thickness (cm)	3.76E-03	3.28E-03
OPyC thickness (cm)	3.76E-03	4.92E-03
Kernel density (g/cm^3)	11.032	10.900
Buffer density (g/cm^3)	1.030	1.070
IPyC density (g/cm^3)	1.912	1.868
SiC density (g/cm^3)	3.197	3.205
OPyC density (g/cm^3)	1.893	1.921

The average value of SIC radial stress was -8.86E+7 Pa.

Results of tangential stress on SiC layer are represented in Figure 4.28 and Table 4.32.

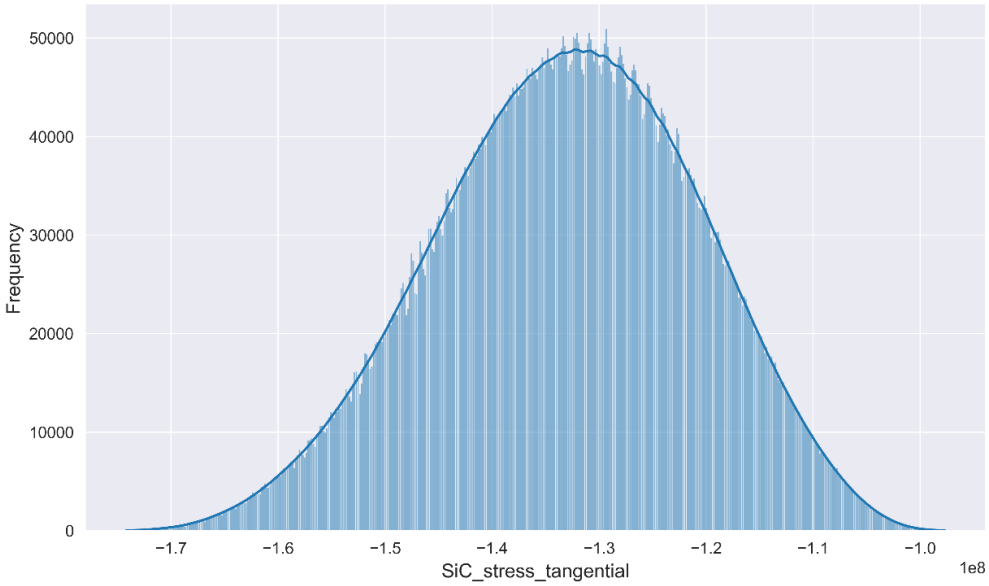

Figure 4.28: Distribution of tangential stress on SiC layer

Table 4.32: Tangential stress on SiC layer case description (batch 5)

Parameter	Max case	Min case
Gas pressure (Pa)	5.55E+06	3.09E+06
Pd penetration (m)	5.09E-06	5.09E-06

Parameter	Max case	Min case
SiC radial stress (Pa)	-7.59E+06	-1.00E+07
Maximum SiC radial stress (Pa)	-2.25E+06	-2.38E+06
Minimum SiC radial stress (Pa)	-2.3E+07	-2.7E+07
SiC tangential stress (Pa)	-5.9E+07	-1.2E+08
Maximum SiC tangential stress (Pa)	-2.5E+07	-3.1E+07
Minimum SiC tangential stress (Pa)	-2.9E+08	-4E+08
IPyC Weibull failure fraction	0.2267	0.2951
SiC Weibull failure fraction	7.95E-09	2.24E-08
Kernel radius (cm)	0.0222	0.0205
Buffer thickness (cm)	8.21E-03	0.0116
IPyC thickness (cm)	3.54E-03	4.54E-03
SiC thickness (cm)	3.76E-03	3.28E-03
OPyC thickness (cm)	3.76E-03	4.92E-03
Kernel density (g/cm^3)	10.900	11.032
Buffer density (g/cm^3)	1.070	1.030
IPyC density (g/cm^3)	1.868	1.912
SiC density (g/cm^3)	3.205	3.193
OPyC density (g/cm^3)	1.893	1.921

The average value of SiC radial stress was -2.49E+7 Pa.

Results of IPyC layer failure fraction are represented in Figure 4.29 and Table 4.33.

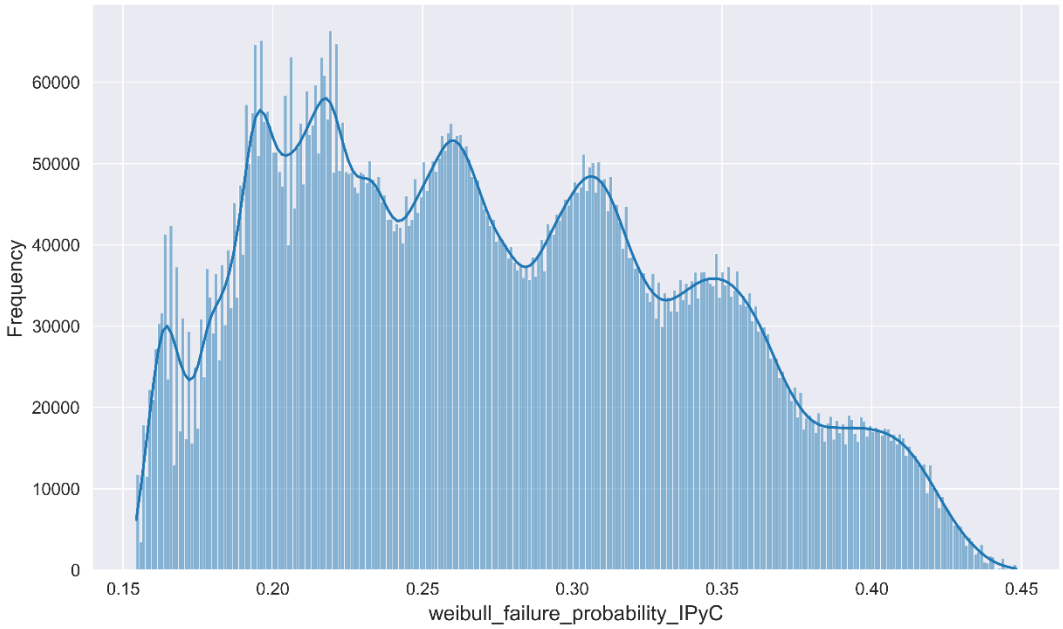

Figure 4.29: Distribution of failure fraction of IPyC layer

Table 4.33: IPyC layer failure fraction case description (batch 5)

Parameter	Max case	Min case
Gas pressure (Pa)	4.68E+06	4.52E+06
Pd penetration (m)	5.09E-06	5.09E-06
SiC radial stress (Pa)	-7.70E+06	-1.00E+07
Maximum SiC radial stress (Pa)	-2.24E+06	-2.48E+06
Minimum SiC radial stress (Pa)	-2.3E+07	-2.7E+07
SiC tangential stress (Pa)	-7.8E+07	-9.9E+07
Maximum SiC tangential stress (Pa)	-2.9E+07	-2.8E+07
Minimum SiC tangential stress (Pa)	-3.4E+08	-3.5E+08
IPyC Weibull failure fraction	0.4482	0.1544
SiC Weibull failure fraction	6.05E-08	3.90E-09
Kernel radius (cm)	0.0205	0.0222
Buffer thickness (cm)	8.21E-03	9.89E-03
IPyC thickness (cm)	4.54E-03	3.54E-03

Parameter	Max case	Min case
SiC thickness (cm)	3.76E-03	3.28E-03
OPyC thickness (cm)	3.76E-03	4.92E-03
Kernel density (g/cm^3)	11.032	10.900
Buffer density (g/cm^3)	1.030	1.070
IPyC density (g/cm^3)	1.868	1.912
SiC density (g/cm^3)	3.189	3.205
OPyC density (g/cm^3)	1.893	1.921

The average value of IPyC Weibull failure fraction was 0.2741.

Results of SiC layer failure fraction are represented in Figure 4.30 and Table 4.34.

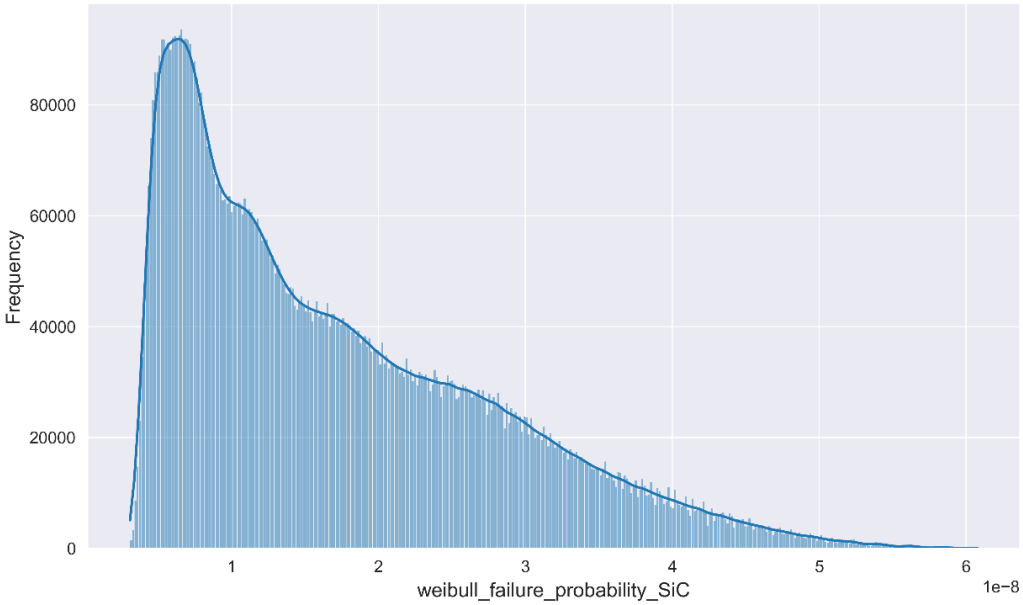

Figure 4.30: Distribution of failure fraction of SiC layer

Table 4.34: SiC layer failure fraction case description (batch 5)

Parameter	Max case	Min case
Gas pressure (Pa)	4.68E+06	3.71E+06
Pd penetration (m)	5.09E-06	5.09E-06

Parameter	Max case	Min case
SiC radial stress (Pa)	-8.58E+06	-9.03E+06
Maximum SiC radial stress (Pa)	-2.05E+06	-2.61E+06
Minimum SiC radial stress (Pa)	-2.3E+07	-2.7E+07
SiC tangential stress (Pa)	-8.3E+07	-9.5E+07
Maximum SiC tangential stress (Pa)	-2.8E+07	-3E+07
Minimum SiC tangential stress (Pa)	-3.4E+08	-3.5E+08
IPyC Weibull failure fraction	0.4475	0.1550
SiC Weibull failure fraction	6.08E-08	3.09E-09
Kernel radius (cm)	0.0205	0.0222
Buffer thickness (cm)	8.21E-03	0.0116
IPyC thickness (cm)	4.54E-03	3.54E-03
SiC thickness (cm)	3.76E-03	3.28E-03
OPyC thickness (cm)	3.76E-03	4.92E-03
Kernel density (g/cm^3)	11.032	10.900
Buffer density (g/cm^3)	1.030	1.070
IPyC density (g/cm^3)	1.868	1.912
SiC density (g/cm^3)	3.189	3.189
OPyC density (g/cm^3)	1.921	1.893

The average value of SiC Weibull failure fraction was 1.71E-08.

4.3 Summary and discussions

This section summarizes the results from both an uncertainty quantification and an optimization perspective. The results of the min and max cases from the pressure analysis are presented in Figure 4.31 and Table 4.35. As Figure 4.31 shows, the ratio of the max case

pressure is 30% more than the reference case starting from the second batch. Also, the reference case pressure is very close to the average pressure from the cases. This means that geometrical and material uncertainties can bring up to 30% higher pressure values in the kernel layer. On the other hand, as the distribution is not normal, the minimum pressure was around 20% less than the average. The geometrical and material properties of the min and max pressure cases are presented below for each batch.

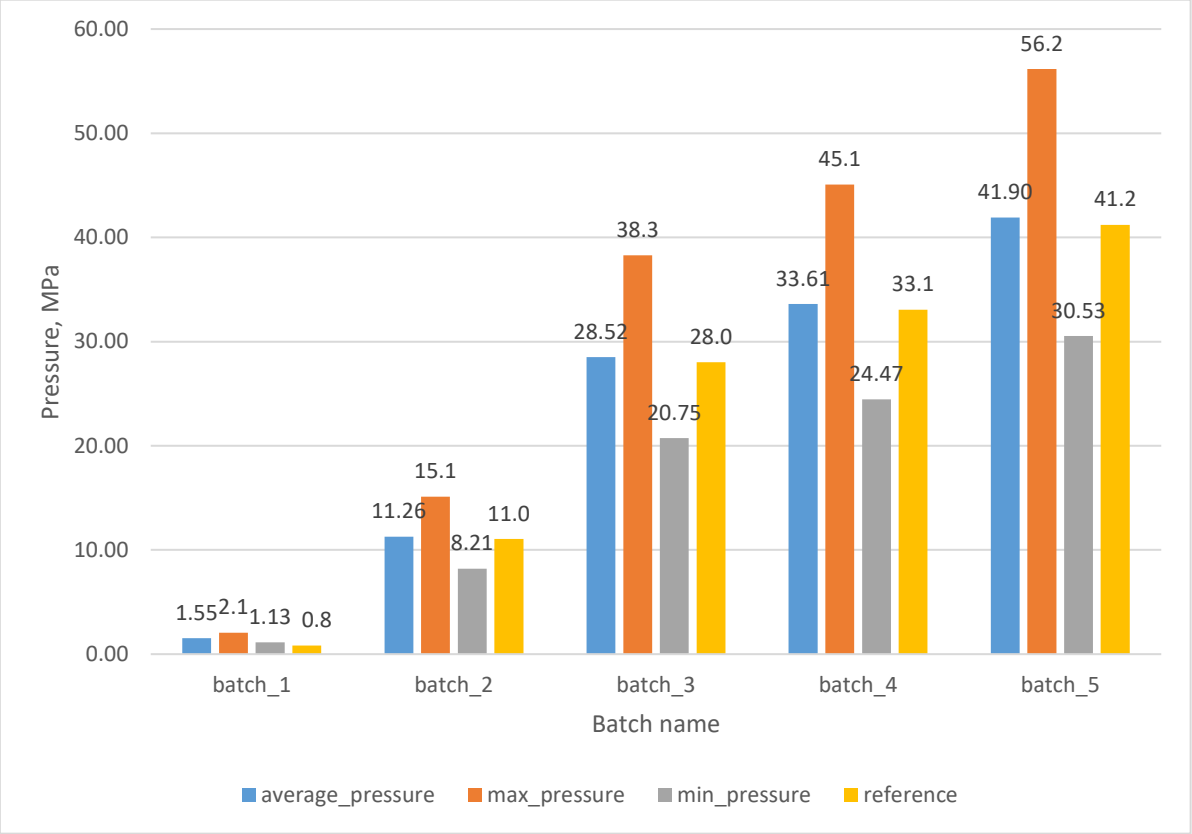

Figure 4.31: Min, max and average values of pressure from each batch

Table 4.35. Minimum and maximum cases for the pressure for each batch

Pressure results	b1 min	b1 max	b2 min	b2 max	b3 min	b3 max	b4 min	b4 max	b5 min	b5 max
Kernel radius	0.22215	0.20455	0.22215	0.20455	0.22215	0.20455	0.22215	0.20455	0.22215	0.20455
Buffer thickness	0.0821	0.1157	0.0821	0.1157	0.0821	0.1157	0.0821	0.1157	0.0821	0.1157
IPyC thickness	0.0354	0.0454	0.0354	0.0454	0.0354	0.0454	0.0354	0.0454	0.0354	0.0454
SiC thickness	0.0328	0.0376	0.0328	0.0376	0.0328	0.0376	0.0328	0.0376	0.0328	0.0376
OPyC thickness	0.0492	0.0376	0.0492	0.0376	0.0492	0.0376	0.0492	0.0376	0.0492	0.0376

Pressure results	b1 min	b1 max	b2 min	b2 max	b3 min	b3 max	b4 min	b4 max	b5 min	b5 max
Kernel density	10.9	11.032	10.9	11.032	10.9	11.032	10.9	11.032	10.9	11.032
Buffer density	1.07	1.03	1.07	1.03	1.07	1.03	1.07	1.03	1.07	1.03
IPyC density	1.912	1.868	1.912	1.868	1.912	1.868	1.912	1.868	1.912	1.868
SiC density	3.189	3.205	**3.197**	3.205	**3.197**	**3.193**	3.189	3.205	3.189	3.205
OPyC density	**1.893**	**1.921**	1.921	1.893	1.921	1.893	1.921	1.893	1.921	1.893

As we can see from Table 4.35, mostly the SiC density and OPyC density are changing over batch to batch, however the geometrical parameters are remaining consistent for min and max cases. The kernel radius is the min for the min pressure, and the max for the max pressure, which is logical (because of more fuel mass, and therefore more fission gases). Therefore, dependent on the irradiation time, it might be beneficial to increase/ decrease SiC and OPyC densities.

The results of the min and max cases from the palladium penetration are presented in Figure 4.32 and Table 4.36.

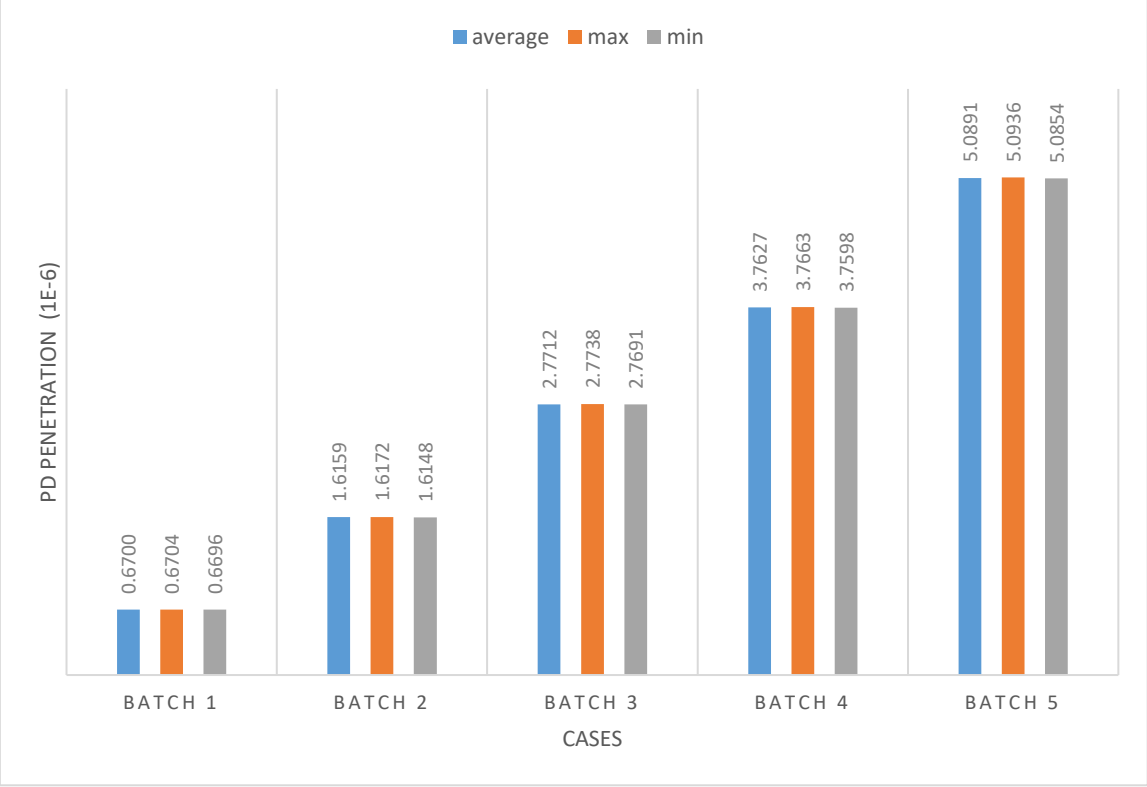

Figure 4.32 Min, max and average values of palladium penetration from each batch

Figure 4.32 shows, that Pd penetration is not very much dependent on the geometrical and material data. The best cases of the geometrical and material data are presented.

Table 4.36. Minimum and maximum cases for the Pd penetration for each batch

Pressure results	b1 max	b1 min	b2 max	b2 min	b3 max	b3 min	b4 max	b4 min	b5 max	b5 min
Kernel radius	0.22215	0.20455	0.22215	0.20455	0.22215	0.20455	0.22215	0.20455	0.22215	0.20455
Buffer thickness	0.0821	0.1157	0.0821	0.1157	0.0821	0.1157	0.0821	0.1157	0.0821	0.1157
IPyC thickness	0.0354	0.0454	0.0354	0.0454	0.0354	0.0454	0.0354	0.0454	0.0354	0.0454
SiC thickness	0.0376	0.0328	0.0376	0.0328	0.0376	0.0328	0.0376	0.0328	0.0376	0.0328
OPyC thickness	0.0492	0.0376	0.0492	0.0376	0.0492	0.0376	0.0492	0.0376	0.0492	0.0376
Kernel density	11.032	10.9	11.032	10.9	11.032	10.9	11.032	10.9	11.032	10.9
Buffer density	1.03	1.07	1.03	1.07	1.03	1.07	1.03	1.07	1.03	1.07
IPyC density	1.868	**1.912**	1.868	**1.912**	**1.912**	1.868	**1.912**	1.868	**1.912**	1.868
SiC density	3.189	3.205	3.189	**3.201**	3.189	**3.201**	**3.197**	3.205	**3.197**	3.205
OPyC density	1.921	1.893	1.921	1.893	1.921	1.893	1.921	1.893	1.921	1.893

The results of analysis of the radial stress on SiC layer are presented in Figure 4.3.

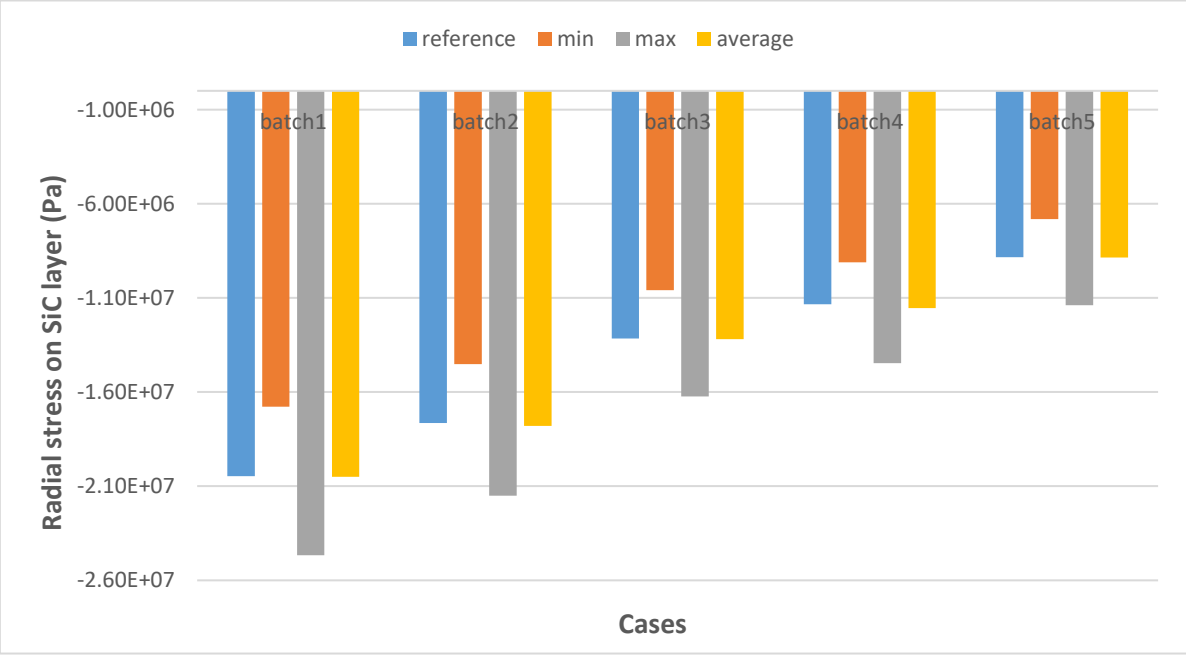

Figure 4.33 Min, max, average, and reference values of radial stress from each batch

As we can see from Figure 4.33 the radial stress over the irradiation is decreasing, which is corresponding to the general case. However, from the uncertainty point of view we can see, that relative difference of the reference radial stress and max radial stress is changing by 20%–28%, and in case of min value it is changing by 18%–22%. Also, the difference between reference case and average value is less than 1% over the irradiation time.

The results of analysis of the tangential stress on SiC layer are presented in Figure 4.34. Figure 4.34 shows that the tangential stress over the irradiation is decreasing, which is corresponding to the general case. It also shows that the relative difference between the reference and the maximum tangential stress values changes by 25% – 32%, and in the case of the minimum value it changes by 19%–32%. Also, the difference between the reference and the average values is less than 1% over the irradiation time.

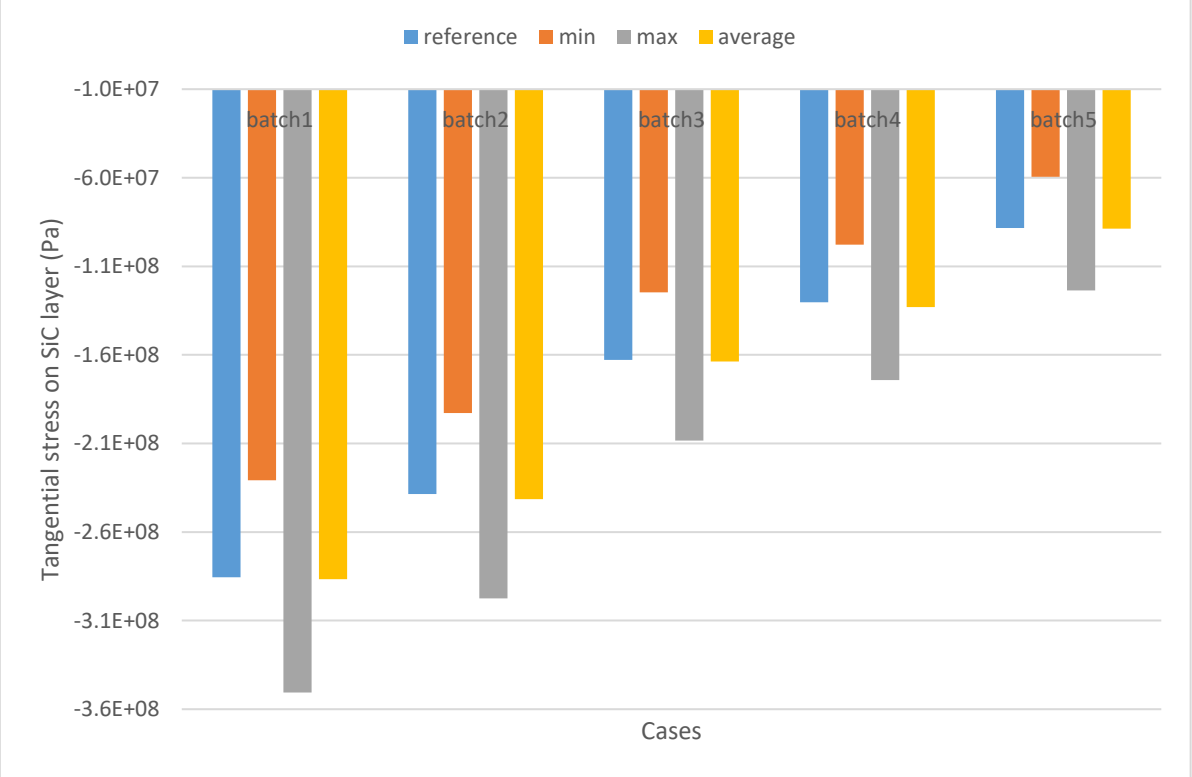

Figure 4.34: Min, max, average, and reference values of tangential stress from each batch

In Figure 4.35 the results of the IPyC layer failure fraction are presented. As the main contributor in the failure fraction is the maximum stress, the failure fraction numbers after the batch 1 is not changing. However, it is important to see how much difference can be expected for the high burnup cases, when the absolute max stress can be more than at the beginning of the irradiation. As Figure 4.35 shows, there can be up to 65% relative difference in the failure

fraction with the max value and the reference value, which can be significant to consider at high burnup level cases.

In Figure 4.36 the results of the SiC layer failure fraction are presented. As the main contributor in the failure fraction is the max stress (like in IPyC case), the max failure fraction is coming from the batch 1.

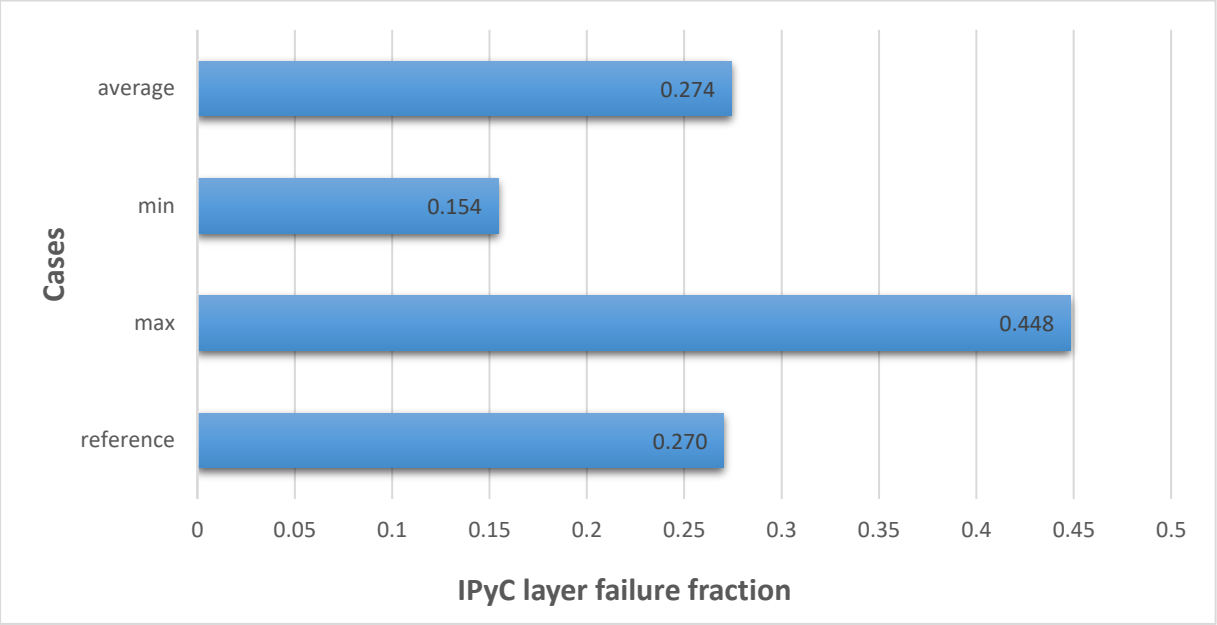

Figure 4.35: Min, max, average, and reference values of IPyC layer failure fraction

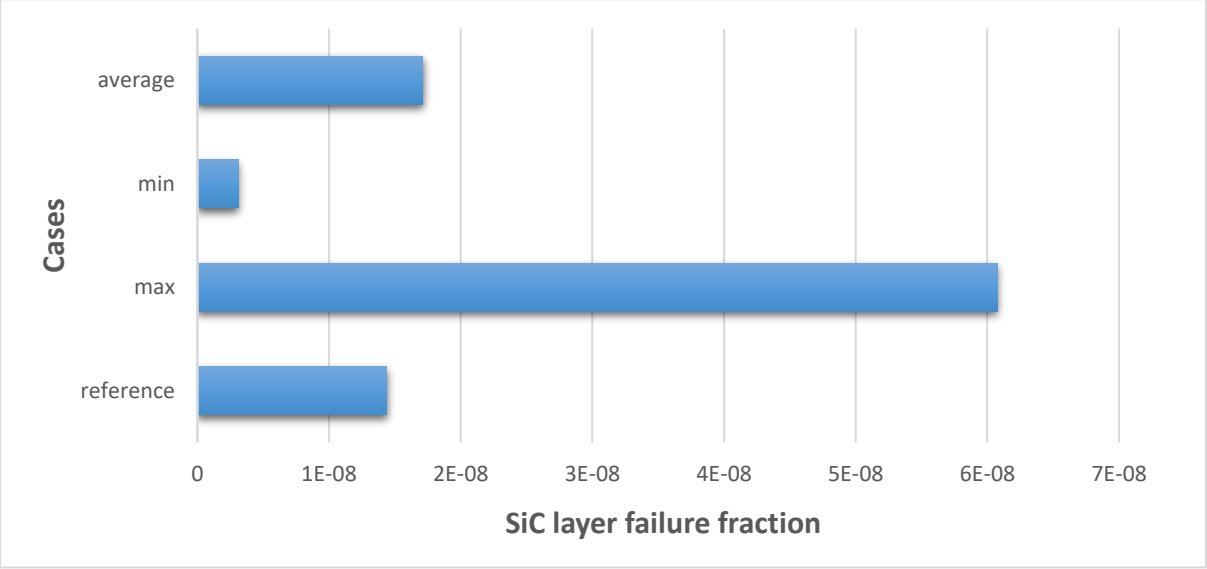

Figure 4.36: Min, max, average, and reference values of SiC layer failure fraction

Figure 4.36 shows that the max failure fraction can be around 80% more than the reference case, and it can be significant for high burnup level cases. The relative difference between reference and average failure fractions is around 3%.

5. Conclusions

This thesis offers a thorough investigation of TRISO fuel particle performance analysis. It starts with a brief overview of past and current reactor designs that utilize TRISO fuel particles as nuclear fuel, including experimental, prototype, and commercial designs. The second Chapter delves into essential phenomena in TRISO fuel performance analysis, examining current modelling capabilities and highlighting open questions for future studies. The findings are published in a peer-reviewed journal as a comprehensive review paper [123].

Based on the review results, Chapter 3 represents the analysis of pressure buildup in TRISO fuel particles with UCO and UO_2 type kernels at varying burnup levels. Different methods are utilized to quantify the concentrations of fission gases and helium inside the fuel kernel, and comparisons are made to determine the impact on SiC failure rate. The results are published in a peer-reviewed journal and reveal that Xe gas makes up the main contribution to pressure buildup analysis (more than 80%) for both UCO and UO_2 type fuel kernels [136]. Kr gas accounts for approximately 18% of total pressure in the case of UCO fuel and 10% in the case of UO_2 type kernel (using Homan model for calculating free oxygen release). Additionally, the ideal gas law and Redlich-Kwong equation of state provide similar results at low burnup values, with the latter being more conservative (1.8% difference in case of Xe gas at high burnup values). For high burnup values, the appropriate model implementation is crucial, and the Redlich-Kwong equation is recommended for safety analysis. The fuel failure rate for UO_2 kernel is higher than for UCO type kernel, although the probability of fuel failure is almost 2 orders less than the acceptance criteria, even at the highest burnup values.

Finally, the uncertainties and variations in geometrical configurations and material properties of TRISO fuel particles are quantified, and the optimization potential of TRISO particles is discussed. AGR-2 experiment capsule 5-1-2 is selected as a reference case, and approximately 10 million calculations are performed using Bison code to evaluate how selected output parameters change due to different combinations of input parameters. The results show that the distributions of output parameters are mostly not normal, and the difference between reference and bounding values can vary significantly. Furthermore, for most cases, this difference increases over irradiation time, and TRISO fuel material and geometry configurations should be considered for high burnup level design concepts. It is essential to note that the current research only considered optimization potential from the mechanical perspective, and overall quantification requires considering also other factors, such as neutronics and thermo-hydraulics [137]. Nevertheless, these results serve as the primary

estimation for potential redesign changes of TRISO fuel particles for new design concepts and are published in a peer-reviewed journal as a standalone article.

6. References

1. Special issue, “High-temperature reactors and the Dragon project”, the Journal of the British Nuclear Energy Society, Vol. 5, 1-4, 1966
2. Chapman, B., “Operation and maintenance experience with the Dragon reactor experimental”, Proc. ANS Meeting on Gas-Cooled Reactors, HTGR and GCFBR, Gatlinburg, May 1974
3. Graham, L.W. et al., “HTR fuel development and testing in the Dragon project”, CONF-740501, National Technical Information Service, 1974
4. Rennie, C.A., “Achievements of the Dragon project”, Annals of Nuclear Energy 5, 1978
5. Ashworth, F.P. et al., “A summary and evaluation of the achievements of the Dragon project and its contributions to the development of HTR”, Dragon Project Report 1000, U.K, Atomic Energy Establishment, 1978
6. Simon R., “The Primary Circuit of the Dragon High Temperature Reactor Experiment”, In the Proceedings from 18th International Conference on Structural Mechanics in Reactor Technology, Berlin, Germany, 2005
7. Beck J.M., C.B. Garcia and L.F. Pincock, “High Temperature Gas-Cooled Reactors Lessons Learned Applicable to the Next Generation Nuclear Plant”, INL/EXT-10-19329, Idaho National Laboratory, Idaho Falls, Idaho, 2010
8. Simnad M.T., “The early history of high-temperature helium gas-cooled nuclear power reactors”, Energy 16, 25-32, 1991
9. P. Fortescue et al., “HTGR underlying principles and design”, Nucleonics 18, N1 86, 1960
10. Fisher C.R. and D.D. Orvis, “Licensing HTGRs in the United States. Proceedings from International Working Group on Gas-Cooled Reactors”, International Atomic Energy Agency, Austria, 1981
11. Goodjohn A.J., “Summary of Gas-Cooled reactor programs”, Energy 16, 79-106, 1991
12. Marnet C., G. Ivens, and E. Ziermann, “The AVR power plant in its last year of operation”, Energy 16, 71-77, 1991
13. Yasukawa S., et al., “The study on the role of very high-temperature reactor and nuclear process heat utilization in future energy system”, JAERI-M-86-165, 1986
14. Kitamura N., et al., “Present status of initial core fuel fabrication for the HTTR”, IAEA-TECDOC, 988, Johannesburg, Dec. 1997
15. Jojiri N., et al., “Characteristics of HTTR”, IAEA-TECDOC, 988, Johannesburg, Dec. 1997

16. Special issue, JAERI, “Present Status of the HTGR Research and Development”, 1989
17. S. Shiozawa, et al., “The HTGR program in Japan and the HTTR project”, IAEA TCM, Petten, 1994
18. Tanaka T., “Construction of the HTTR and its testing program”, 3rd JAERI Symposium on HTGR Technologies, Oarai, 1996
19. Shiozawa S., “Research and development of HTTR hydrogen production systems in JAERI”, Proc. 12th Pacific Basin Nuclear Conference, Seoul, Korea, 2000
20. Wu Z., D. Lin, and D. Zhong, “The design features of the HTR-10”, Nuclear Engineering and Design, 218, 25-32, 2002
21. Wang Dazhong, Lu Yingyun, “Roles and prospect of nuclear power in China’s energy supply strategy”, Nuclear Engineering and Design, 218, 2002
22. INET/Interatom/KFA Jülich, “China-German R&D cooperation, HTR test module China”, Final Report for the Concept Phase, Sept. 1988
23. Yuanhui X., Zhenya Q., Zongxin W., “Design of the 10 MW high-temperature reactor”, IAEA TCM, Petten, 1994
24. Institute of Nuclear Energy Technology, Tsinghua University, “Design criteria for the 10 MW high-temperature gas-cooled test reactor”, IAEA TECDOC 899, Vienna, Aug. 1996
25. Special issue, “The Chinese high-temperature reactor HTR-10 -the first inherently safe generation IV nuclear power system”, Nuclear Engineering and Design, Vol. 218, N1-3, 2002
26. Special issue, “The 300 MW Thorium high-temperature nuclear power plant THTR”, Atomwirtschaft, 5, May 1971
27. Baust E., Rautenberg J., Wohler J., “Results and experience from the commissioning of the THTR 300”, Atomkernenergie-Kerntechnik, Vol. 47, 1985
28. Special issue, “Fort St. Vrain nuclear power station”, Nuclear Engineering International, Dec. 1971
29. Olson H. G., Swart P.E., “Fort St, Vrain high-temperature gas-cooled reactor”, Nuclear Engineering and Design, 72, 1982
30. Schulten R., et al., Industrial nuclear power plant with high-temperature reactor PR-500, OTTO principle for the product HHT on of process steam, JŰL-941RG, 1973
31. IAEA, “Design and evaluation of heat utilization systems for the high-temperature engineering test reactor”, IAEA-TECDOC-1236, Vienna, 2001
32. Jansing W., “Testing of high-temperature components in the KVK, Specialists Meeting on Heat Exchanging Components of Gas-Cooled Reactors”, Düsseldorf, April 16 -19, 1984

33. Ohashi H., et al., “Current status of research and development on system integration technology for connection between HTGR and hydrogen production system at JAERI”, OECD/NEA: 3rd Information Exchange Meeting on the Nuclear Production of Hydrogen, Oarai; Japan, 2005
34. D. Olander, “Nuclear Fuels-Present and Future”, Journal of Nuclear Materials, 389, 2009
35. Paul A. Demkowicz, Bing Liu, John D. Hunn, “Coated Particle Fuel: Historical Perspectives And Current Progress”, Journal of Nuclear Materials, 515, 434, 2019
36. Jing Wang, “An Integrated Performance Model For High Temperature Gas Cooled Reactor Coated Particle Fuel”, PhD Thesis, MIT 2004
37. Jian Li, Ding She, Lei Shi, “Status Of Development Of An Integrated Source Term Analysis Code Package For HTGR", Proceedings of HTR 2018, Warsaw, Poland, 2018
38. Petti D.A. et al., “Development of Improved Models and Design of Coated Particle Gas Reactor Fuels: Annual Program Report Under the International Nuclear Energy Research Initiative (I-NERI)”, INEEL/EXT-02-0493, Nov 2002
39. Proksch E., Strigl A., Nabielek H., “Production of carbon monoxide during burn-up of UO_2 kerneled HTR fuel particles”, Journal of Nuclear Materials, 107, 280, 1982
40. G. W. Horsley et al., “Influence of Irradiation Temperature, Burnup, and Fuel Composition on Gas Pressure (Xe, Kr, CO, CO_2) in Coated Particle Fuels”, Journal of the American Ceramic Society, 59, 1976
41. E. López-Honorato et al., “Characterization Of The Anisotropy Of Pyrolytic Carbon Coatings And The Graphite Matrix In Fuel Compacts By Two Modulator Generalized Ellipsometry And Selected Area Electron Diffraction”, Journal of Carbon, 50, 2, 2012
42. P. R. Goggin et al., “Dimensional changes in the irradiated graphite lattice”, Journal of Carbon, 189, 1964
43. G. E. Bacon, “A Method For Determining The Degree Of Orientation Of Graphite”, Journal of Applied Chemistry, 6, 477, 1956
44. J.C. Bokros, “Deposition, Structure And Properties Of Pyrolytic Carbon”, Chemistry and Physics of Carbon, 5, 8, 1969
45. T. Arai, S. Sato, T. Oku, H. Schiffers And W. Delle, “Assessment of Heterogeneity and Anisotropy of IG-110 Graphite for Nuclear Components”, Journal of Nuclear Science and Technology, 28, 8, 713, 1991
46. Nam Zin Cho, Hui Yu, Jong Woon Kim, “Two-Temperature Homogenized Model For Steady-State And Transient Thermal Analyses Of A Pebble With Distributed Fuel Particles”, Annals of Nuclear Energy, 36, 448, 2009

47. J. Shentu, Yun S., N.Z. Cho, “A Monte Carlo Method For Solving Heat Conduction Problems With Complicated Geometry”, Nuclear Engineering and Technology, 39, 207, 2007
48. J.H. Song and N.Z. Cho, “An Improved Monte Carlo Method Applied To The Heat Conduction Analysis Of A Pebble With Dispersed Fuel Particles”, Nuclear Eng. Technology, 2008
49. E. Saragi, “Modeling of Temperature Distribution in TRISO Fuel-Based on Finite Element Method”, The 3rd International Conference on Advances in Nuclear Science and Engineering, 2011
50. Haitao Wang, Xin Wang, “Study On Temperature Distribution On Pebble Bed HTR Fuel Element By Using Boundary Element Method”, Proceedings of the ASME, Pressure Vessels and Piping Conference PVP2013, France 2013
51. “Fuel Performance And Fission Product Behaviour In Gas Cooled Reactors”, International Atomic Energy Agency Technical Document, IAEA-TECDOC-978, 1997
52. J.T. Maki et al., “The Challenges Associated With High Burnup, High Temperature And Accelerated Irradiation For TRISO-Coated Particle Fuel”, Journal of Nuclear Materials, 371, 270, 2007
53. K. Fukuda et al., “Research and Development of HTGR fuel”, JAERI-Report, Japan Atomic Energy Research Institute, JAERIM 89-107, 1989
54. K. Sawa, S. Ueta, “Research and development on HTGR fuel in the HTTR project”, Nuclear Engineering and Design, 233, 167, 2004
55. Oya Zdere Glol et al., “Performance Analysis Of TRISO Coated Fuel Particles With Kernel Migration”, Journal of Nuclear Materials, 374, 168, 2008
56. A.H. Booth, “A Method of Calculating Fission Gas Release from UO_2 Fuel and its Application to the X-2-f Loop Test”, Atomic Energy of Canada Limited, 496, 1957
57. A. Muller, J. Stadif, “Ein Programm zur Berechnung der stationaren Kuhlgasaktivitat in Kugelhaufen-HTR”, Report Jul-1464, Research Center Julich, 1977
58. W. Schenk, D. Pitzer, H. Nabielek, Fission Product Release Profiles from Spherical HTR Fuel Elements at Accident Temperatures, Kernforschungsanlage Jülich GmbH Institut für Reaktorwerkstoffe, Jül-2234, 1988
59. H. Nabielek, B. Myers, Fission Product Retention in HTR Fuel, Gas-Cooled Reactors Today, British Nuclear Energy Society, 145, 1982
60. B.F. Myers, “The Fuel Design Data Manual”, Report GA-901866/F, GA Technologies, 1987

61. J.A. Turnbull et al., “The Diffusion Coefficients of Gaseous and Volatile Species during the Irradiation of Uranium Dioxide”, Journal of Nucl. Mat., 107, 168, 1982
62. R. Williamson, “Facsimile message on enhanced vacancy diffusion to B. F. Myers”, AEA Technology, UK, ORNL, June 6, 1996
63. B.F. Myers, “Fission Gas Release in High Temperature Gas-Cooled Reactors”, Archival Viewgraphs, Oak Ridge National Laboratory, 1991
64. B.J. Myers, R.E. Morrissey, “Licensing Topical Report: The Measurement and Modelling of Time-Dependent Fission Product Release from Failed HTGR Fuel Particles under Accident Conditions”, Report GA-A15439, General Atomic Company, 1978
65. D. Olander, “Fundamental Aspects of Nuclear Reactor Fuel Elements”, Report TDD-26711-P1, Technical Information Center, Office of Public Affairs, Energy Research and Development Administration, 1976
66. T. Ogawa et al., “Release of Short-Lived Noble Gases from HTGR Fuel with Failed Coated Fuel Particles and Contaminated Matrix”, Nuclear. Eng. Design, 132, 31, 1991
67. D.G. Hurst, “Diffusion of Fission Gas, Calculated Diffusion from a Sphere Taking into Account Trapping and Return from Traps”, Report AECL-1550, Atomic Energy of Canada Limited, 1962
68. G.W. Momot, A.A. Hruljev, “Limits of Safe Operation in Terms of Fission Product Release from the Fuel Element and its Justification”, Fuel and Graphite for HTR (Proc. 1st Soviet/German Seminar, Moscow, 1990), Internal Report KFA-HTA-IB-6/90, Research Center Julich, 319-335, 1990
69. P.E. Brown And R.L. Faircloth, “Metal Fission Product Behaviour In High Temperature Reactors - UO_2 Coated Particle Fuel”, Journal of Nuclear Materials 59, 29, 1976
70. H. Krohn, R. Finken, “FRESCO: Ein Rechenprogramm zur Berechnung der Spaltproduktfreisetzung aus kugelfonnigen HTR-Brennelementen in Bestrahlungsund Ausheizexperimenten”, Report Jul-Spez-212, Research Center Julich, 1983
71. R. Berger-Rossa, “Ruckhaltung und Umverteilung von Spaltprodukten im Core und im Primarkreislauf von Hochtemperatur reaktoren bei hypothetischen Storfaller- eignissen”, Report Jul-2188, Research Center Julich, 1988
72. U.J. Mattke, “Berechnung der Spaltproduktverteilung in Core und Primarkreislauf eines Hochtemperaturreaktors im Noimalbetrieb”, Report Jul-2515, Research Center Julich, 1991
73. K. Sawa et al., “Validation of Fission Product Release from Fuel Element of HTTR”, J. Nucl. Sci. Tech., 29, 842, 1992

74. W.W. Hudrttsch, “COPAR2: A Program to Compute the Release of Fission Products from Coated Particles”, GA Document No. 908696, GA Technologies Inc., 1986
75. P.X. Smith, TRAFIC, “A Computer Program for Calculating the Release of Metallic Fission Products from an HTGR Core”, Report GA-A14721, General Atomic Company, 1978
76. J.W. Prados and J.L. Scott, “Models for Fission Gas Release from Coated Fuel Particles”, Oak Ridge National Laboratory, Report ORNL-3421, 1963
77. B.P. Collin, “Diffusivities of Ag, Cs, Sr, and Kr in TRISO Fuel Particles and Graphite”, INL/EXT-16-39548, Revision 0, 2016
78. H. Kleykamp, “The Chemical State Of The Fission Products In Oxide Fuels”, Journal of Nuclear Materials, 131, 221, 1985
79. Haiming Wen, Isabella J. Van Rooyen, “Distribution Of Fission Products Palladium, Silver, Cerium And Caesium In The Un-Corroded Areas Of The Locally Corroded SiC Layer Of A Neutron Irradiated TRISO Fuel Particle”, Journal of the European Ceramic Society, 37, 3271, 2017
80. E.J. Olivier, J.H. Neethling, “Palladium transport in SiC”, Nuclear Engineering and Design, 244, 25, 2012
81. K.M. Minato et al., “Fission Product Palladium-Silicon Carbide Interaction In HTGR Fuel Particles”, Journal of Nuclear Materials, 172, 184, 1990
82. K. Minato et al., “Fission Product Behavior in TRISO-Coated UO_2 Fuel Particles”, Journal of Nuclear Materials, 208, 266, 1994
83. K.M. Minato et al., “Release Behaviour Of Metallic Fission Products From HTGR Fuel Particles at 1600 to 1900C”, Journal of Nuclear Materials, 202, 47, 1993
84. T.N. Tiegs, “Fission product Pd-SiC interaction in irradiated coated-particle fuels”, Nuclear Technology, 57, 389, 1981
85. R.L. Pearson et al., “The Interaction of Palladium, The Rare Earths, and Silver with Silicon Carbide in HTGR Fuel Particles”, Oak Ridge National Laboratory, 1982
86. T. Ogawa, K. Ikawa, “Reactions of Pd with SiC and ZrC”, High Temperature Science, 22, 179, 1986
87. R.J. Lauf, “The Interaction of Silver and Palladium with Silicon Carbide in HTGR Fuel Particles”, Preliminary Report, Oak-Ridge National Laboratory, 1980
88. F. Montgomery, “Fission Product-SiC Reaction in HTGR Fuel”, General Atomic Company, Report DOE T/35300-T3, 1981

89. K. Ikawa, F. Kobayashi, K. Iwamoto, “Failure of Coated Fuel Particles During Thermal Excursion Above 2000 °C”, J. Nucl. Sci. Technol., 15, 10, 774, 1978
90. H. Suzuki et al., “Reactions Between SiC And Pd or CeO_2 At High Temperatures”, Journal of Nuclear Science and Technology, 14, 6, 438, 1977
91. P.A. Demkowicz et al., “High Temperature Interface Reactions Of TiC, TiN, And SiC With Palladium And Rhodium”, Solid State Ionics, 179, 2313, 2008
92. J.H. Neethling et al., “Palladium Assisted Silver Transport In Polycrystalline SiC”, Nuclear Engineering and Design, 2011
93. I.J. van Rooyen et al., “Effects Of Phosphorous-Doping and High Temperature Annealing on CVD GROWN 3C-SiC”, Nucl. Eng. Des., 251, 191, 2012
94. I.J. Van Rooyen, J.H. Neethling, A. Henry, E. Janzén, “Influence of phosphorous and high temperature annealing on the nanostructures of 3C-SiC”, HTR 2010, 2010
95. H. Zhang, E. López-Honorato, P. Xiao, “Effect of Thermal Treatment on Microstructure and Fracture Strength of SiC Coatings”, J. Am. Ceram. Soc., 96, 5, 1610, 2013
96. J.J. Hancke, G.T. Rooyen, J.P.R. De Villiers, “The Effect of Coating Parameters and Annealing on the Crushing Strength of TRISO Coated Particle”s, Nucl. Technol., 182, 1, 49, 2013
97. I.J. Van Rooyen, E.J. Olivier, J.H. Neethlin, “Investigation Of The Distribution Of Fission Products Silver, Palladium And Cadmium In Neutron Irradiated SiC Using a Cs Corrected HRTEM”, HTR2014-3-1255, Proceedings of the HTR 2014 Conference, China, 2014
98. I.J. Van Rooyen, M.L. Dunzik-Gougar, P.M. Van Rooyen, “Silver (Ag) transport mechanisms in TRISO coated particles: a critical review”, Nucl. Eng. Des., 271, 180, 2014
99. D.A. Petti et al., “Key Differences In The Fabrication, Irradiation And High Temperature Accident Testing Of US And German TRISO-Coated Particle Fuel, And Their Implications On Fuel Performance”, Nucl. Eng. Design, 222, 281, 2003
100. K. Bongartz, E. Gyarmati, H. Schuster, K. Tauber, “The Brittle Ring Test: A Method for Measuring Strength and Young’s Modulus on Coatings of HTR Fuel Particles”, J. Nucl. Mater. 62, 123, 1976
101. K. Bongartz et al., “Measurement of Young's Modulus and Fracture Stress on HTR Particle Coatings by the Brittle Ring Test”, J. Nucl. Mater., 45, 261, 1972
102. T.S. Byun et al., “Evaluation of Fracture Stress for the SiC Layer of TRISO-Coated Fuel Particles Using a Modified Crush Test Method”, Int. J. Appl. Ceram. Technol., 7, 327, 2010

103. J.D. Hunn et al., “Fabrication and Characterization of Sixteen SiC Variants Deposited on the Same IPyC Substrate for Fracture Strength Testing”, Oak Ridge National Laboratory Research Report. ORNL/TM-2009/324, December 2009
104. T.S. Byun et al., “Fracture Stress Data for SiC Layers in TRISO-Coated Fuel Particles”, Oak Ridge National Laboratory Research, Report ORNL/TM-2008/167, 2008
105. X. Zhao et al., “Mechanical Properties of Sic Coatings on Spherical Particles Measured Using The Micro-Beam Method”, Scripta Materials, 59, 39, 2008
106. E. Lopez-Honorato et al., “TRISO Coated Fuel Particles With Enhanced SiC Properties”, Journal of Nuclear Materials, 392, 2, 219, 2009
107. J. Tan et al., “Young’s Modulus Measurements of Sic Coatings on Spherical Particles by Using Nanoindentation”, Journal of Nuclear Materials, 393, 1, 22, 2009
108. G.K. Miller et al., “Statistical Approach and Benchmarking for Modelling of Multi-dimensional Behavior of TRISO-coated Fuel Particles”, J. Nucl. Materials, 317, 69, 2003
109. K. Minato, K. Fukuda, “SiC Coating of Small Particles in a Fluidized Bed Reactor”, Advanced Materials and Manufacturing Processes, 3, 4, 617, 1988
110. D. Helary et al., “EBSD Investigation of SiC for HTR Fuel Particles”, Journal of Nuclear Materials, 350, 3, 332, 2006
111. L. Tan et al., “EBSD for Microstructure and Property Characterization of the SiC-coating in TRISO Fuel Particles”, J. Nucl. Mater., 372, 2, 400, 2008
112. J.D. Hunn et al., “Increase In Pyrolytic Carbon Optical Anisotropy And Density During Processing Of Coated Particle Fuel Due To Heat Treatment”, J. Nucl. Mater., 374, 3, 445, 2008
113. J.L. Kaae, “The Effect Of Annealing On The Microstructures And The Mechanical Properties Of Poorly Crystalline Isotropic Pyrolytic Carbons”, Carbon, 10, 3, 1972
114. D.P. Harmon, C.B. Scott, “Properties Influencing High-Temperature Gas-Cooled Reactor Coated Fuel Particle Performance”, Nucl. Technology, 35, 2, 343, 1977
115. “NP-MHTGR Material Models of Pyrocarbon and Pyrolytic Silicon Carbide”, CEGA-002820, CEGA Corporation, 1993
116. D. Petti et al., “Development of Improved Models and Designs for Coated-Particle Gas Reactor Fuels”, INEEL/EXT-05-02615, December 2004
117. J.L. Kaae, “A Mathematical Model for Calculating Stresses in a Four Layer Carbon Silicon Carbide Coated Fuel Particle”, Journal of Nuclear Materials, 32, 2, 1969
118. K. Bongartz, “Improvement of a Method for Predicting Failure Rates of Coated Particles During Irradiation”, Nucl. Techn., 35, 379, 1977

119. K. Bongartz, “Status of the Fuel Stress and Failure Rate Calculations at KFA”, Julich, GmbH, 1980

120. G.K. Miller, R.G. Bennett, “Analytical Solution for Stresses in TRISO-coated Particles”, Journal of Nuclear Materials, 206, 1, 35, 1993

121. Hibbitt et al., “ABAQUS User’s Manual”, Version 5.8, Inc., 1998

122. J. Powers, Brian D. Wirth, “A review of TRISO fuel performance models”, Journal of Nuclear Materials, Volume 405, Issue 1, Pages 74-82,2010,

123. Nairi Baghdasaryan & Tomasz Kozlowski, “Review of Progress in Coated Fuel Particle Performance Analysis, Nuclear Science and Engineering”, 194:3, 169-180, 2020

124. “NEA Benchmark of the Modular High-Temperature Gas-Cooled Reactor-350 MW Core Design Volumes I and II”, NEA/NSC/R, 16 February 2018

125. J. Leppanen, “PSG2/Serpent - a Continuous-energy Monte Carlo Reactor Physics Burnup Calculation Code”, User’s Manual 2012

126. FJ. Homan et al., “Stoichiometric Effects on Performance of High-Temperature Gas-Cooled Reactor Fuels from the UCO System”, Nucl. Techn. 35, pages 428-441, (1977)

127. W Jiang et al., “Efficient High-Fidelity TRISO Statistical Failure Analysis using BISON: Applications to AGR-2 Irradiation Testing”, Journal of Nuclear Materials, 153585, 2022

128. Jian Li et al., “Influence of input data uncertainties on failure fraction of TRISO-coated particle”, Annals of Nuclear Energy, 163, 2021

129. Rong Li, Bing Liu, Karl Verfondern, “The study of irradiation-induced failure behavior for the TRISO-coated fuel particle in HTGR”, Journal of Nuclear Materials, 516, 2019

130. K.A. Terrani, L.L. Snead, J.C. Gehin, “Microencapsulated fuel technology for commercial light water and advanced reactor application”, J. Nuclear Materials, 427, pp. 209-224, 2012

131. N.R. Brown et al., “Neutronic evaluation of a PWR with fully ceramic microencapsulated fuel, part I: lattice benchmarking, cycle length, and reactivity coefficients”, Ann. Nucl. Energy, 62, pp. 538-547, 2013

132. X. Dai et al., “Conceptual core design of an innovative small PWR utilizing fully ceramic microencapsulated fuel”, Prog. Nucl. Energy, pp. 63-71,2014

133. S. Sahin, H.M. Sahin, A. Acır “Utilization of TRISO fuel with reactor grade plutonium in CANDU reactors”, Nucl. Eng. Des, 240, pp. 2066-2074, 2010

134. J.D. Stempien, J.D. Hunn, R.N. Morris, T.J. Gerczak, P. Demkowicz, “AGR-2 TRISO Fuel Post-Irradiation Examination Final Report”, Technical Report INL/EXT-21-64279, Idaho National Laboratory, Idaho Falls, ID United States, 2021.
135. Heinz Nabielek at al., “The Performance of High-Temperature Reactor Fuel Particles at Extreme Temperatures”, Nuclear Technology, 84:1, 62-81, 1989
136. Nairi Baghdasaryan & Tomasz Kozlowski ”Pressure buildup analysis of TRISO-coated fuel particles”, Nuclear Engineering and Design, Volume 380, 2021
137. Nairi Baghdasaryan et al., “TRISO Fuel Performance Analysis: Uncertainty Quantification Toward Optimization”, Nuclear Engineering and Design, Volume 410, 2023